Aqueous Corrosion of Aluminum-Based Nuclear Fuel

by M. D. Kaminski

Argonne National Laboratory, with facilities in the states of Illinois and Idaho, is
owned by the United States Government and operated by The University
of Chicago under the provisions of a contract with the Department of Energy.

ANL-CMT-03/1

AQUEOUS CORROSION OF ALUMINUM-BASED NUCLEAR FUEL

Michael D. Kaminski
Chemical Engineering Division
Argonne National Laboratory
Argonne, IL 60439 USA

April 2003

CONTENTS

FIGURES

TABLES

Aqueous Corrosion of Aluminum-Based Nuclear Fuel

Michael D. Kaminski
Chemical Technology Division
Argonne National Laboratory
Argonne, IL 60439

ABSTRACT

As part of the U.S. National Spent Nuclear Fuel Program, aluminide fuels (UAl_x) are being tested under conditions that might exist in the proposed repository at Yucca Mountain, Nevada. Intermittent drip tests at 90°C were completed for up to 183 days on partially declad, unirradiated, low-enriched UAl_x samples. Through 183 days of exposure to modified water from the J-13 well at 90°C, the fuel coupon remained in good mechanical condition. Only a tarnishing of the surface was observed and no spalled products were found in the fuel holder. The mechanism for alteration is consistent with that observed from dry oxidation experiments on UAl_x (for the initial corrosion) and humid UO_2 oxidation (for the subsequent paragenesis). Specifically, solid-state conversion of UAl_x into UO_2 and oxidized Al is followed by further oxidation, dissolution of the uranium, and reprecipitation as uranyl oxyhydroxides. The release rate of uranium varied from 0.23 to 2.9 $mg/m^2/day$ (avg. = 0.97 mg $U/m^2/day$) depending on the specimen and test interval, but was similar in magnitude to that observed in earlier flow-through and drip tests with irradiated UAl_x and UO_2. Most (mean=87%) of the released uranium sorbed to the vessel walls. Colloids were detected in the leachate samples, and dynamic light scattering of aliquots from most sampling periods favored a polydisperse distribution typical of environmental samples. In addition, the light scattering intensities measured in these tests were much higher than any measured from UO_2 fuel tests in our laboratory. Electron microscopy of the colloids indicated that the colloids were individual and agglomerated silicates and aluminosilicates. No distinct uranium-rich colloids were found, although dissolved uranium would be expected to sorb to aluminosilicate colloids. In conclusion, the UAl_x corroded slowly, releasing uranium at a rate comparable to UO_2 fuels. Colloid production, however, was quite high with light scattering intensities that were much higher than any measured in previous tests with spent fuels in our laboratory.

I. INTRODUCTION

The large inventory of spent nuclear fuel (SNF) owned by the Department of Energy (DOE) is being evaluated for potential disposal within the proposed mined geological repository near Yucca Mountain, Nevada. These fuels include those from the weapons production reactors at the Hanford site, test reactors such as the Fast Flux Test Facility and Materials Test Reactor, and numerous domestic and foreign research reactors such as the TRIGA reactors. To enable licensing and acceptance of these fuels at the repository, federal law requires accurate data and models that will predict the behavior of these fuels over a geologic time frame. The National Spent Nuclear Fuel Program (NSNFP) was created to "safely and efficiently manage all DOE-owned spent nuclear fuel and prepare it for disposal" [USDOE-2002].

The Release Rate Program under the NSNFP was created to ensure that experimental data and release-rate models are compatible with methodologies developed for commercial SNF and high-level waste glass to support the performance assessment activities. In general, the tests conducted under the Release Rate Program will provide information that can be useful to the NSNFP and the Yucca Mountain Project (YMP) in characterizing the performance of spent uranium-aluminum fuel under potential repository conditions. This information will be used to identify important degradation modes for this spent fuel and contribute to predictive model development of radionuclide and fission product release. The information will also provide a technical basis for determinig the source term for radionuclide release. The concentrations of radionuclides as measured in these tests may be used in Total System Performance Assessment (TSPA) calculations instead of values obtained from expert elicitation panels, or from solubility studies of individual phases.

Of the more than 200 types of spent nuclear fuel in the inventory, eleven were chosen as most representative and four were chosen as high-priority for immediate testing. The four fuel types designated for immediate testing are mixed oxide, metallic uranium (from the Hanford N-Reactor), graphite, and intermetallic uranium-aluminum. This report summarizes program activities on the testing of intermetallic uranium-aluminum (U-Al) fuels. The tests simulate possible repository conditions; spent uranium-aluminum fuel is contacted by small amounts of water that drip through a mock spent fuel container. The type of information derived from these tests includes the degradation rate of spent uranium-aluminum fuel (this includes dissolution, selective leaching, and physical processes that may alter the spent uranium-aluminum fuel under

repository conditions (as distinguished from basic dissolution kinetics testing in support of model development), the release rate of radionuclides from the spent uranium-aluminum fuel, and the chemistry and mineralogy of altered spent uranium-aluminum fuel and secondary minerals that form on the surface of the spent fuel. These key outputs are recorded as a function of the total time of reaction. The first phase of this program is to carry out the described tests on unirradiated fuels to address test design modifications, anticipated sampling frequency, primary alteration phases, and release rates for uranium.

This report is meant as a database for geologically unsaturated testing of unirradiated U-Al fuel. It contains a complete record of data and analysis from this program to date, including extensive appendices (A-E). Samples prepared by the melt-dilute process for the treatment of Al-based fuels may be tested within a few years. The differences between the fuels tested under this program and the expected melt-dilute compositions and their effect on fuel corrosion and radionuclide release are discussed briefly in Appendix B.

II. ALUMINIDE DISPERSION FUEL AND ITS CORROSION

The majority of U-Al fuels are composed of dispersions of powdered intermetallic uranium aluminide or UAl_x (UAl_2, UAl_3, and UAl_4) in aluminum with aluminum cladding (see Appendix A for an expanded discussion of other U-Al fuel types). When irradiated, the highest aluminide, UAl_4, is most stable and abundant in the fuel. The aluminide fuels are considered top priority for testing for reasons that include their relative volume in the DOE inventory, their high enrichment, and their metallurgical similarity to the final alloy form from the melt-dilute process [Adams-1999]. (See Appendix B for a discussion of the melt-dilute process.)

A.   Aqueous Corrosion

Morphological changes during aqueous dissolution have not received much impetus for detailed study in the past, as previous corrosion studies on aluminum-based fuels have been largely qualitative. It has been shown that the aluminum on the cladding surface and in the fuel meat corrodes relatively rapidly in an oxidizing, humid environment. The reaction mechanism involves the redox conversion of aluminum metal into hydrated aluminum oxides via

$$2Al + 4H_2O \rightarrow Al_2O_3 \bullet H_2O + 3H_2 \tag{1}$$

where $Al_2O_3 \bullet H_2O$ is boehmite. Exposure of aluminum fuels to moist, elevated temperatures and oxidative conditions leads to the rapid growth of the boehmite layer. This growth is unlike that which characterizes the passivation of aluminum at lower temperatures, where a thin boehmite or bayerite (AlOOH) layer forms and protects the metal from further oxidation.

No specific mechanistic study has been completed, to the author's knowledge, of wet oxidation of UAl_x metal, but a mechanism can be proposed on the basis of dry oxidation experiments and wet oxidation of UO_2 fuels. The corrosion of UAl_x under dry conditions [Openshaw-1964] occurs by diffusion of O_2-derived oxygen anion into the UAl_x lattice and segregation of aluminum and can be written as

$$UAl_x + O_2 \rightarrow UO_2 + xAl \tag{2}$$

Under dry oxidation, $UO_{2.33}$ and U_3O_8 phases form,

$$3UO_2 + \frac{1}{2}O_2 \rightarrow 3UO_{2.33} \xrightarrow{\frac{1}{2}O_2} U_3O_8 \qquad (3)$$
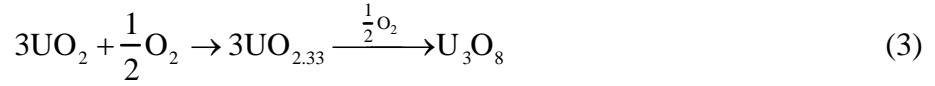
Crystallographically, oxidation of UO_2 would increase the oxygen stochiometry[1] to the point where the fluorite lattice of $UO_{2.33}$ can remain intact [Shoesmith-1992]. Further oxidation would require significant restructuring of the layered orthorhombic U_3O_8 via solid-state nucleation and growth [Taylor-1989]. In the presence of water, the conversion of UAl_x will be facilitated by diffusing species derived from water, in much the same manner as seen in the corrosion of metallic uranium [Colmenares-1984]. The reaction may be written as
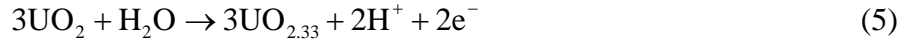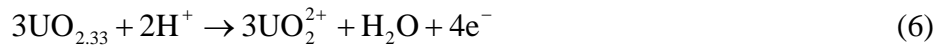
$$UAl_x + \left(\frac{3}{2}x + 2 + n\right)H_2O \rightarrow UO_2 + \left(\frac{3}{2}x + 2\right)H_2 + \left(\frac{x}{2}Al_2O_3\right) \cdot nH_2O \qquad (4)$$
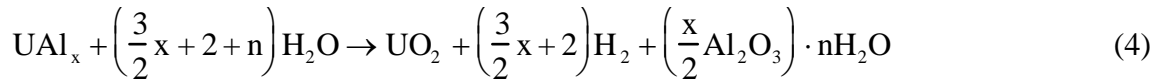
where the diffusion of water-derived species may dominate over O_2-derived species. The oxidation of the dioxide of uranium proceeds in the solid state as

$$3UO_2 + H_2O \rightarrow 3UO_{2.33} + 2H^+ + 2e^- \qquad (5)$$

where an appropriate reducing species would couple to the reaction. Higher oxidation would require rearrangement of the lattice through a dissolution and reprecipitation mechanism in a thin film of adsorbed water [Sunder-1981, Taylor-1989, -1995] to form the uranyl oxyhydroxides

$$3UO_{2.33} + 2H^+ \rightarrow 3UO_2^{2+} + H_2O + 4e^- \qquad (6)$$

and

$$UO_2^{2+} + \frac{1}{2}O_2 + xH_2O + 2e^- \rightarrow UO_3 \bullet xH_2O \qquad (7)$$
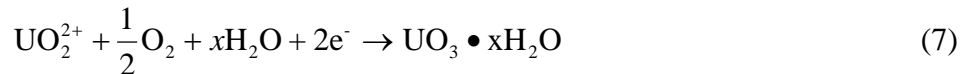
where the hydrated uranyl oxides such as dehydrated schoepite [Taylor-1989, -1995] would be more prevalent at high humidity and saturation conditions. Taylor et al. [1991] found that U_3O_8

---

[1] The reactions are written as UO_2 but are more appropriately identified by UO_{2+x} since stoichiometric UO_2 would not be maintained under environmental conditions [Colmenares-1984, Sunder-1981].

would be the stable form in a saturated environment if the oxygen were to become depleted in the reaction vessel. Under such conditions, dehydrated schoepite may redissolve, allowing the U(VI) to partially reduce and precipitate to form U_3O_8. Undoubtedly, the presence of high ionic strength solution with Si and Ca would favor the inclusion of such cations into the oxidized uranyl crystal. Taylor et al. [1991] recognized that, given the narrow field of stability for U_3O_8 in pure water oxidation, it is unlikely that U_3O_8 would precipitate from solution. Instead, paragenesis would favor uranates or silicates in complex solution such as groundwaters. Indeed, U_3O_8 is not found in natural mineral systems. Schoepite and its dehydrated derivatives have been identified with Si and Ca inclusions from natural analogs [Taylor-1995]. Additionally, one might expect the formation of becquerelite, $Ca(UO_2)_6O_4(OH)_6 \cdot 8H_2O$ which is known to associate with schoepite, or uranophane, $Ca(UO_2)_2(SiO_3,OH)_2 \cdot 4H_2O$, which can occur as acicular masses on uraninite [Gaiter-1989]. From the above discussion, one would expect that the UAl_x fuel oxidizes to $UO_{2.33}$ as U diffuses to the surface and grain boundary and Al oxidizes to Al_2O_3 or hydrated derivatives or exists as an impurity in the uranyl oxyhydroxide. However, $UO_{2.33}$ is less stable than dehydrated schoepite or uranyl silicates with the silicates likely forming later in the paragenetic sequence [Finch-1999, Finn-1995].

B.   <u>Previous Work</u>

Savannah River Site (SRS) has performed much of the work regarding the dissolution of Al-based fuels in repository-relevant conditions using simulated J-13 water. Researchers at SRS [Mickalonis-1998] used microscopy to study the corrosion of the surrogate fuels and found that the boehmite layer expands with time and spalls off the surface as oxidation progresses into the fuel meat. The aluminide particles appeared unreacted as the boehmite layer continued to grow suggesting a cathodic protection of the aluminide by the surrounding aluminum [Mickalonis-1998], a logical conclusion given the relative position of Al and UAl_x in the galvanic series. However, this cathodic protection did not occur in two failed aluminide fuel plates from the Advanced Test Reactor (ATR) [Vinjumari-1983]. The ATR plates experienced pinhole corrosion where 0.2 and 0.8 g of UAl_x fuel (~14 g/yr) dissolved. It is interesting to note that except for the pinhole, the corrosion was exclusive to the fuel meat region. This would suggest little galvanic protection afforded by the aluminum matrix towards the UAl_x fuel grains under ATR coolant conditions.

Dissolution observed by SRS [Mickalonis-1998] followed two distinct stages. The first stage was common to all alloy compositions tested (10, 13.2, and 25 wt% U) and all corrodent compositions (high-pH, low-pH, and nominal J-13 water); the aluminum matrix surrounding the uranium aluminide fuel grains dissolved preferentially, leaving the fuel grains loosely attached to the surface. The second stage was dependent on the corrodent composition. In nominal J-13 water, a thin protective oxide layer formed on the fuel surface and was susceptible to pitting corrosion. In low-pH J-13 water, corrosion of the aluminum continued until the solution became saturated in this element, at which time a thick aluminum oxide layer formed on the surface, significantly reducing uranium dissolution. In high-pH J-13 water, corrosion of the aluminum continued but aluminum saturation was not reached, and uranium continued to dissolve until uranium saturation was reached.

Savannah River researchers also conducted vapor corrosion testing on 10 and 18 wt% uranium alloy surrogates at 200°C for up to 62.5 days [Lam-1998]. Results were similar to those found in static testing. The alloy containing 18% uranium formed an outer layer of loosely adhered boehmite with isolated uranium-rich aggregates (likely uranyl oxyhydroxides). X-ray analysis of these aggregates showed uranium enrichment and very little aluminum.

Flow-through tests were completed [Wiersma-1998] on partially declad U-Al alloy, UAl_x, U_3O_8, and U_3Si_2 irradiated samples. The corrodent was variants of J-13 water at 25 and 90 °C. The dissolution rates for test periods up to 200 days were ~0.2 mg $U/m^2/d$ in J-13 for all fuel types at 25°C. Similar tests on unirradiated, cast UAl_x yielded dissolution rates of 24 mg $U/m^2/d$ at 90°C (release of plutonium was monitored periodically and coincided somewhat with uranium values). One might expect the irradiated fuels to display higher release rates based on the behavior of commercial UO_2 fuels and metallic uranium fuels. However, when one considers the metallurgy of the aluminide fuels during burnup, it is logical to assume that the release rates for uranium will be lower than in unirradiated fuels. Irradiation accelerates the diffusion of aluminum atoms into the UAl_x grains, creating almost exclusively UAl_4 in burned fuels, which is thermodynamically more stable than its lower stoichiometric mixtures. It is well documented that the porosity of these fuels is lower upon irradiation, and the solubility of fission products and gases is high in UAl_x (see Appendix A for further discussion and citations). Thus, an irradiated UAl_x fuel has much more favorable properties for retaining uranium than an unirradiated fuel.

Static (no-flow) tests [Wiersma-1998] were completed in 2.5-L glass vessels at 90°C in a closed atmosphere with U-Al samples (surrogates) submerged in variants of J-13 water for up to one month. The dissolution of uranium was most severe in J-13 water adjusted to pH 10, followed by J-13 water adjusted to pH 3, followed by nominal J-13 water (relative dissolution rate ratio 5:2:1). Galvanic couples with stainless steel produced the same trend (relative dissolution rate ratio 20:10:1) but with 2-10 times more uranium in solution than samples coupled to aluminum. In high-pH J-13 water, dissolved uranium concentration was constant after one week of exposure at 90°C. This finding was interpreted as a result of uranium saturation in solution.

Still to be determined are the elemental release rates under other hypothetical aqueous corrosion scenarios. Little information exists on likely paragenesis, and no information is available on the persistence and nature of colloids that may be generated in a repository environment. The tests conditions governing the program discussed in this report will allow us to address these issues and build upon previously completed studies.

III. TECHNICAL APPROACH

A.   Materials

1.   Fuel

The fuel chosen for testing was a low-enriched full-sized flat plate manufactured by CERCA (Argentina) using powder metallurgical techniques (Area# H-137A, Plate# 020V-1019, Batch# 140-20-8772-0000, from ORNL SPM 24#E-834, 19.75% ^{235}U). The fuel meat is composed of UAl_x (70.2 wt% U) in aluminum with surrounding AG3NE alloy (3% Mg, 97% Al). A picture-frame design was used to construct the fuel plate (see Fig. 1). The test specimens were prepared from an unirradiated plate at the Alpha-Gamma Hot Cell Facility (AGHCF) at Argonne (IPS Document# IPS-329-00-00). Square coupons of approximately 5-mm length and 2.5-mm thickness were cut from the middle of the fuel plate (samples A/G571A, A/G571B, A/G571C, and A/G571D according to Alpha-Gamma Hot Cell Facility nomenclature), and one side of the fuel cladding face was polished to 600 grit in an epoxy mount to reveal the fuel meat. The epoxy was cracked and the coupon removed. Residual epoxy was dissolved with acetone and the coupon rinsed with deionized water. Relevant dimensions for the coupons along with chemical composition data from inductively coupled plasma-mass spectroscopy (ICP-MS) of the fuel meat and cladding are shown in Table 1. The fuel meat was analyzed after the cladding was completely removed from fuel specimen 571D by polishing. Cladding samples for composition analysis were obtained from cutting scraps during the initial sample cutting at AGHCF. Both the fuel meat and cladding samples were dissolved and analyzed.
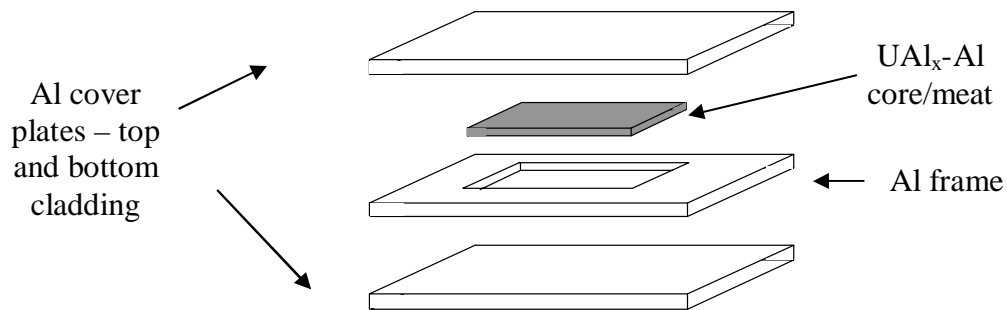

Fig. 1. Schematic of Picture-Frame Design Used to Manufacture Aluminide Fuels. The four plates are hot rolled to ensure a metallurgical bond between the pressed fuel meat powder and protective cladding. Test samples were cut from the center of the fuel plate and one side of the cladding was removed.

Table 1. UAl$_x$ Fuel Coupon Dimensions and Chemical Composition

Fuel Dimensions (mm or mm^2)	UNAUT1(571A)	UNAUT2(571C)	UNAUT3(571C)
Length	5.32	4.68	4.78
Width	4.76	4.36	4.03
Total Thickness	1.91	1.76	1.55
Meat Thickness	1.47	1.36	
Total Fuel Area	54.96	44.99	
Total Sample Area	89.15	72.63	65.84

Element	Fuel Meat (g/g)	Cladding (g/g)
Na	2.92×10^{-5}	$<4 \times 10^{-4}$
Mg	2.63×10^{-5}	3.13×10^{-2}
Al	0.497	9.62×10^{-1}
Si	0.00025	3.06×10^{-4}
K	9.74×10^{-5}	1.61×10^{-4}
Ca	0.00039	8.41×10^{-4}
Fe	0.00145	3.44×10^{-3}
Zr	1.45×10^{-5}	8.66×10^{-6}
Au	9.68×10^{-8}	1.93×10^{-7}
^{235}U	0.10	NA
^{238}U	0.39	4.07×10^{-5}
Total	0.99	1.0

2.   *Leachant and Reagents*

The water used in these tests was taken from the J-13 well and reacted at 90°C for 21 days with crushed core samples of Topopah Spring tuff. The well water prepared in this manner is called EJ-13 and is characterized by higher silicon and sodium content than J-13 water (see Table 2). Ultrapure nitric acid prepared to 1% was used to acidify fuel samples prior to analysis and to strip sorbed elements from the surface of the test vessels.

Table 2. Major Elemental Composition
of EJ-13 Water

Element	Concentration* (ng/g)
Na	5.54×10^4
Mg	290
Al	560
Si	4.1×10^4
Ca	1.1×10^4
Fe	250
Zr	1
Au	<0.2
U	0.8
K	12,000
CO_3^{2-}	26×10^3
Cl^-	15×10^3
F^-	3.8×10^3
NO_3^-	14×10^3

*Two sample averages from EJ-13 batches used
in the drip tests. Anions are from historical
averages for EJ-13 used at Argonne.

3.   Test Vessel

The fuel and leachant were added to a sealed stainless steel vessel. A schematic is provided in Figure 2. The threaded cap contained a single steel penetration that was connected to the injection tubing. By opening a valve on the injection tubing, gas pressure could be released, water could be injected onto the fuel, and the vessel could be pumped with air to replenish the oxygen supply. A copper gasket was placed between the cap and base and the cap was tightened to ~140 ft-lb torque.
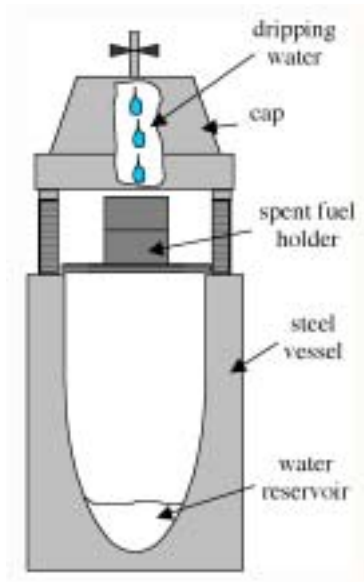
Fig. 2. Schematic Diagram of Stainless Steel "Drip Test" Vessel (cap. ~60 mL).

4.   Fuel Holder

The fuel was placed in a three-chamber fuel holder (see Fig. 3). The first design used a zircaloy bottom filter instead of the 0.011-mm bottom screen shown in Figure 3. The zircaloy filter contained numerous laser-drilled holes approximately 0.010 mm in diameter. This design was scrapped in favor of the 0.011-mm-opening gold screen. To make the bottom gold screen, the 0.025 mm screen was placed below the 0.011 mm screen to provide support and the two screens were mechanically sandwiched between two Zircaloy washers and inserted into the existing Zircaloy cylinder after cooling to liquid nitrogen temperature. This design allowed water to flow through the fuel holder more efficiently and was used for Test UNAUT1 after 115 days, and for the entire testing period for Tests UNAUT2 and UNAUT3.

Fig. 3. Zircaloy-4 Spent Fuel Holder Used for Drip Tests. The fuel is placed on the 0.6-mm screened chamber that was stacked on the middle chamber and placed on the 0.011-mm screened base. This entire assembly was suspended in a stainless steel vessel and sealed (ruler is in inches).

5.   *Unsaturated Drip-Test Methods*

The fuel was placed in the top chamber of a three-chamber fuel holder, which was subsequently placed in a stainless steel test vessel. Five milliliters of EJ-13 was injected into the base of the vessel and the vessel was sealed prior to test initiation. No special precautions were taken to prevent galvanic coupling of the fuel and steel vessel because it is recognized that the fuels will be in direct contact with steel materials while in the repository.

Unsaturated drip tests were performed by a method similar to that described previously [Finn-1994]. The vessels were placed in a 90°C oven and 0.75 mL of EJ-13 water was dripped twice a week on the fuel through an external injection port. Specifically, 0.75 mL was measured in a syringe and dispensed through 1/16-in. swage tubing into the vessel. Independent tests showed that at least 0.70 mL of EJ-13 immediately drips into the vessel. The remainder either drains more slowly or is retained in the tubing. Each vessel was connected to a gas gauge to monitor vessel pressure.

Two fuel samples and a blank were placed in separate test vessels. Leachate from the test vessels was sampled periodically. Test 1 (UNAUT1 designation using 571A fuel coupon, 0.1906 mg) was sampled after 31, 67, 115, 151, and 183 days and underwent nondestructive analysis. Test 2 (UNAUT2 designation using 571C fuel coupon, 0.1314 mg) was sampled after

16 days. Test 3 (UNAUT3 designation using 571C fuel coupon from UNAUT2 after polishing, 0.1167 mg) was sampled after 55 days and underwent more destructive analysis. The blank (UNAUB1, no fuel) was sampled after 83 and 151 days.

To sample, the test vessels were cooled to room temperature in less than 15 min using dry ice or less than 30 min using cool tap water and weighed. They were opened, the fuel was removed, and the entire leachate was transferred to a polypropylene bottle (acid-rinsed with 1% HNO_3 followed by deionized water). The only exception was UNAUT1 at the 151-day sampling. Here, the fuel was removed for x-ray diffraction (XRD) analysis only. No other measurements were taken and no liquid was removed from the vessel. Because the vessel was nearly dry at 151 days, an additional volume of EJ-13 was added at test restart. The blank UNAUB1 was run concurrently and employed procedures identical to those in the other tests except that no fuel was included in the vessel.

To remove elements sorbed to the vessel and spent fuel holder, the vessel and fuel holder were submerged in 1% HNO_3 overnight, a procedure referred to as an "acid strip." The vessels and fuel holders were then rinsed thoroughly in deionized water and reused. Solutions were submitted for inductively coupled plasma-mass spectrometry (Fisons VG PlasmaQuadII+ series) as described elsewhere [Wolf-1998]. Aliquots were also withdrawn for colloid analysis by dynamic light scattering (400 μL), transmission electron microscopy (5-25 μL on a holey carbon grid), and pH determination (400 μL).

Microscopy was performed using the Hitachi S3000N or RJ Lee[®] Personal scanning electron microscopes (SEM). The Hitachi (PC-EM S-3000, v. 03-04) is coupled to a NORAN energy dispersive x-ray spectroscope (EDS) (Vantage software v. 1.2.1), while the RJ Lee (PSEM v. 4.03) unit uses a Greshan EDS system (Flame v. 4.4.8). The Hitachi uses the PROZA method for standardless quantitative analysis. Backscatter electron images are shown in this report unless otherwise noted. Semiquantitative EDS elemental analysis was performed occasionally. The accuracy of the method was checked against unreacted UAl_x grains on uncorroded fuel samples for general agreement. For sample UNAUT1, the fuel was placed on an aluminum mount without carbon coating or carbon tape. Following characterization the fuel was placed, as is, in the test vessel for continued testing. Sample UNAUT2, in addition, was mounted in epoxy after 16 days and polished to reveal the transverse view of the alteration layer on the fuel meat. The fuel was removed from the epoxy mount, the surface was scraped of

surface products for future analysis, and the surface was repolished to at least 600 grit prior to test continuation. The polished fuel was used in test UNAUT3, which ran for 55 days. Samples were also characterized using a JEOL 2000 FXII transmission electron microscope (TEM) operating at 200 kV. The time needed to complete microscopy of the fuels ranged from 8 to 23 days, during which time the fuel remained dry and in contact with air. (Data discussed in this report can be found in CMT Scientific Notebook #1682 and references therein.)

IV. RESULTS AND DISCUSSION

A.   General Observations

Table 3 presents sampling data for all tests conducted under this program. The initial water amount dispensed into the vessel base to start the test was 4.96-5.11 g. The dates for the test duration are shown, as well as the cumulative number of test days (i.e., days in test and not total days from start of test) and number of injections between particular samplings. The number of days required to complete the analysis and restart the test is shown in the last column and ranged from 8 to 23 days (when not in test the fuel specimens remained at room temperature). The coupon masses did not change appreciably, although a slight weight gain was observed between the 67- to 115-day sampling period for UNAUT1. As shown in Table 3, UNAUT1 test did not hold water very well, registering losses that progressively worsened after 67 days. A nearly dry vessel was sampled at the 115-day period and the 151-day period. There was a large water loss at the 183-day period due to a leak in the plumbing system, not a leak through the gasket seal. Tests UNAUT2, UNAUT3, and UNAUB1 held water very well.

The pH varied with test time, but not systematically. The large water loss in UNAUT1 after 67 days reduced the relevance of the pH data for that period. The pH for UNAUT2 declined to 6.9 after 16 days. When the coupon was repolished and restarted as UNAUT3, the final pH was 8.3 after 55 days. The pH for the blank test UNAUB1 was practically unchanged— 8.9 after 83 days and 8.5 after 151 days. The water retained in the spent fuel holder (SFH) at the first sampling of UNAUT1 (day 31) was due to the Zircaloy screen initially used as the perforated bottom of the SFH.

Table 3. Measured Parameters for UAl$_x$ Unirradiated Fuel Tests

Test No.	Test Description	Fuel ID	Initial Water (mL)	Test Days	# of Injections	Coupon Mass (g)	pH	Water Lost	Days Needed for Analysis
UNAUT1	Mock test 1	571A	5.04	0	-	0.19	8	-	-
		(#409 SFH	5.11	31	8	0.1906	8.6	2.89	12
		#419 vessel)	5.03	67	8	0.1909	8.4 (9.5 in SFH^b)	2.7	23
			4.96	115	13	0.192	--	13.35	16
			5	151	9	-	-	10.25	8
			-	183	6	0.1916	9.5^c	8.8	-
UNAUT2	Mock test 2	571C	5.03	0	-	0.1314	8	-	-
		(#411 SFH #429 vessel)	-	16	5	0.1333	6.9	1.25	
UNAUT3	Mock test 3	571C	5.03	0	-	0.1167	8	-	-
		(#411 SFH #429 vessel)	-	55	15	0.1171	8.3	0.41	-
UNAUB1	Blank	No fuel	5.01	0	-	-	8	-	-
		(#408 SFH	5.01	83	23	-	8.9	2.65	16
		#420 vessel)	-	151	18	-	8.5	0	-

^{a}Entries with two dates describe the sampling date followed by the date for test restart. The time interval was used to examine the fuel coupon.
^{b}Spent fuel holder.
^{c}Excessive loss of water during this period reduces credibility of this pH measurement.

B.   Release Rates

The amounts of each element released during the various sampling periods are shown in Tables 4-6. These tables also report the U-235 content, which was computed based on 19.75% enrichment and checked against ICP-MS semi-quantitative data. (Appendix E gives the elemental concentrations determined from ICP-MS.) The values are given in terms of nanograms of element dissolved in the vessel base, acid-stripped from the spent fuel holder (SFH), and acid-stripped from the vessel, as well as the total nanograms recovered from all three solutions. (Note that for UNAUT1, day 31, the values shown for the SFH are the quantities in the water that were retained in the fuel holder. For all other days and samples, the SFH values refer to quantities in the acid-strip solutions.) Table 7 expresses the data in terms of percentages associated with each of the dissolved and acid-stripped fractions. Note the large percentage of U and Al sorbed onto the SFH and vessel base. In contrast, Na and K were generally removed as the soluble form.

Table 4.   Elemental Masses (in ng) for Released Elements in Test UNAUT1. Values given for masses found in the leachate of the base and spent fuel holder (SFH) and from the acid strip solution, and the total amount released from the fuel.

	Day 31				Day 67			
	Base	SFH	Strip	Total	Base	Base Strip	SFH Strip	Total
Na	3.51×10^5	7.60×10^4	1.28×10^4	4.40×10^5	4.55×10^5	4.07×10^4	4.58×10^4	5.42×10^5
Mg	143	284	1.54×10^3	1.97×10^3	1.55×10^3	7.88×10^3	9.56×10^3	1.89×10^4
Al	1.29×10^3	1.62×10^3	4.66×10^3	7.57×10^3	5.57×10^3	2.97×10^4	3.47×10^4	7.00×10^4
Si	2.13×10^5	5.56×10^4	1.15×10^4	2.80×10^5	2.81×10^5	1.21×10^5	1.29×10^5	5.30×10^5
K	DNA^a	DNA	DNA	DNA	DNA	DNA	DNA	DNA
Ca	DNA	DNA	DNA	DNA	DNA	DNA	DNA	DNA
Fe	8.28×10^2	1.60×10^2	4.17×10^4	4.27×10^4	9.76×10^2	1.38×10^5	1.27×10^5	2.65×10^5
U	71	105	125	301	515	280	1340	2135
U-235	17.8	26.2	31.2	75	129	70	335	534
	Day 115				Day 183			
	Base	Base Strip	SFH Strip	Total	Base	Base Strip	SFH Strip	Total
Na	6.28×10^5	3.86×10^4	4.93×10^5	1.16×10^6	1.16×10^6	7.67×10^4	1.09×10^5	1.35×10^6
Mg	69	2.29×10^3	2.90×10^3	5.27×10^3	14	3349	2.76×10^3	6.12×10^3
Al	4.61×10^2	1.11×10^4	1.03×10^4	2.18×10^4	8.35×10^2	1.14×10^4	2.31×10^4	3.54×10^4
Si	1.13×10^5	1.75×10^5	6.04×10^4	3.49×10^5	2.37×10^5	8.44×10^4	4.23×10^4	3.63×10^5
K	DNA	DNA	DNA	DNA	1.54×10^5	1.86×10^4	3.03×10^3	1.75×10^5
Ca	2.33×10^2	1.20×10^4	3.44×10^2	1.26×10^4	1.63×10^4	1.04×10^5	2.37×10^4	1.44×10^5
Fe	6.02×10^1	5.78×10^4	3.70×10^3	6.15×10^4	2.99×10^3	3.45×10^4	3.24×10^3	4.07×10^4
U	216	1.07×10^3	1.08×10^3	2.37×10^3	54	596	894	1.54×10^3
U-235	54	267	270	592	13.6	149	224	386

^{a}Did not analyze

Table 5. Elemental Masses (in ng) for Released Elements in Tests UNAUT2 and UNAUT3. Values given for masses found in the leachate of the base and from the acid strip solution, and the total amount released from the fuel.

| | UNAUT2 Day 16 | | | | UNAUT3 Day 55 | | | |
	Base	Base Strip	SFH Strip	Total	Base	Base Strip	SFH Strip	Total
Na	4.83×10^5	1.26×10^4	2.31×10^4	5.19×10^5	8.62×10^5	1.17×10^4	1.11×10^5	9.84×10^5
Mg	956	1.57×10^3	4.79×10^3	7.31×10^3	630	3.94×10^3	4.43×10^3	9.00×10^3
Al	1.02×10^4	9.22×10^3	2.67×10^4	4.62×10^4	6.17×10^3	4.26×10^3	1.06×10^4	2.11×10^4
Si	3.25×10^5	2.65×10^4	1.55×10^4	3.67×10^5	5.29×10^5	2.35×10^4	4.26×10^4	5.95×10^5
K	DNA	DNA	DNA	DNA	1.71×10^5	2.73×10^3	3.92×10^3	1.78×10^5
Ca	4.62×10^4	1.25×10^4	1.70×10^4	7.58×10^4	1.52×10^5	9.75×10^3	1.21×10^4	1.74×10^5
Fe	1.62×10^3	1.33×10^5	3.31×10^3	1.38×10^5	9.26×10^2	4.42×10^4	4.20×10^3	4.93×10^4
U	605	290	790	1.68×10^3	925	202	880	2.01×10^3
U-235	151	73	197	421	231	51	220	502

Table 6. Elemental Masses (in ng) for Released Elements in Test UNAUB1. Values given for masses found in the leachate of the base and from the components acid strip solution, and the total amount released from the fuel.

| | Day 83 | | | | Day 151 | | | |
	Base	Base Strip	SFH Strip	Total	Base	Base Strip	SFH Strip	Total
Na	8.50×10^5	8.34×10^3	4.72×10^5	1.33×10^6	9.70×10^5	7.81×10^3	3.20×10^5	1.30×10^6
Mg	997	1.44×10^3	3.65×10^3	6.09×10^3	432	3.23×10^3	3.17×10^3	6.84×10^3
Al	3.17×10^3	4.69×10^3	5.57×10^3	1.34×10^4	4.74×10^3	3.73×10^3	4.98×10^3	1.35×10^4
Si	6.21×10^5	3.90×10^4	3.85×10^4	6.98×10^5	6.05×10^5	2.13×10^4	2.00×10^4	6.46×10^5
K	DNA	DNA	DNA	DNA	1.94×10^5	2.42×10^3	5.64×10^3	2.02×10^5
Ca	1.14×10^5	9.17×10^3	9.87×10^4	2.22×10^5	1.49×10^5	1.64×10^4	1.59×10^4	1.82×10^5
Fe	1.65×10^3	1.33×10^5	7.72×10^3	1.43×10^5	1.07×10^3	3.47×10^4	6.04×10^3	4.19×10^4
U	5.61	9.38	16.6	32	6.66	<7.98	<18.6	6.66
*U235	1.40	2.35	4.14	7.89	1.67	<0.42	<0.98	1.67

Table 7. Percentage of Element Dissolved in the Base of the Vessel and Derived from an Acid Strip of the Base and Spent Fuel Holder

| | UNAUT1 | | | UNAUT2+UNAUT3 | | | UNAUB1 | | |
	Base	Base Strip	SFH Strip	Base	Base Strip	SFH Strip	Base	Base Strip	SFH Strip
Na	74	5.1	21	89	1.6	9	69	0.6	30
Mg	5	45	50	10	34	57	11	36	53
Al	5	41	54	24	20	56	29	31	39
Si	51	30.6	18.6	89	5.2	6.0	91	4.5	4.4
K	88	10.6	1.7	96	1.5	2.2	96	1.2	2.8
Ca	11	72	16	79	9	12	65	6	28
Fe	1.1	63	36.4	1.4	95	4.0	1.5	91	7.5
U	13	32	55	41	13	45	32	25	43
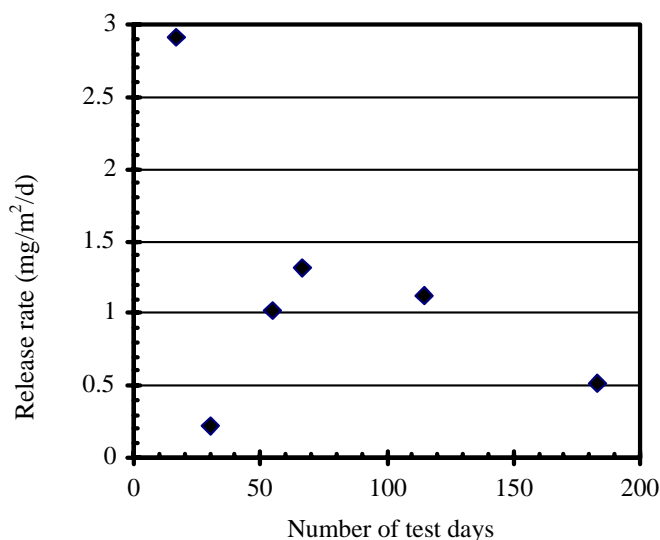
Fig. 4. Uranium Release Rates for UNAUT1 (day 31, 67, 115, and 183), UNAUT2 (day 16), and UNAUT3 (day 55)

The release rates for uranium are shown in Figure 4. The rates are computed from the uranium concentration in the vessel leachate and acid strips during that test interval and normalized to the original fuel meat surface area.[2] A total of a 7.9 µg of uranium (<0.02% of the total inventory[3]) was released after 183 days from fuel UNAUT1 for a normalized rate of 0.8 mg U/m^2/d. The UNAUT2 test showed significantly higher release rates initially at 2.9 mg U/m^2/d. No further testing of UNAUT2 was performed, so it is not possible to determine if the high initial rate would have been maintained at longer test durations. Test UNAUT3 released uranium at 1.01 mg/m^2/d after 55 days. The reason for the discrepancy between day 16 (UNAUT1) and day 31 (UNAUT2) is not known but may be at least partly due to the hydraulics of the drip test. Since the test vessel maintains a water vapor-saturated environment, the fuel will always have a film of water on it. The dripping water provides dissolved cations and anions that may participate in complexation, dissolution, and precipitation reactions and also washes away dissolved products from the surface of the fuel. Test UNAUT1 sustained conditions whereby a thick hydrogel and precipitates formed on the surface. Tests UNAUT2 and UNAUT3 formed comparatively thinner hydrogels and no abundant salt precipitation was observed. Thus, it

---

[2] To compute the release rate normalized to the surface area of exposed UAl$_x$, divide values by 0.5-0.7.

[3] Assuming 70% by mass is fuel, and 49% by mass of fuel meat is U.

appears the dripping water was much more effective at washing the UNAUT2 and UNAUT3 fuel surface of reaction products and produced slightly higher release rates. More about the surface characteristics of the fuel will be explained in Section D, which summarizes the microscopic analysis of the fuel coupons.

Our release rate data are compared with results from flow-through and drip tests on surrogate and irradiated fuels in Table 8. Flow-through tests performed at Pacific Northwest National Laboratory with oxygenated EJ-13 produced uranium release rates an order of magnitude greater than in the present tests [Wiersma-1998]. This result is not surprising given that the flow-through tests are considered a maximum-release test configuration (although this has not been verified). Tests run at 25°C on irradiated aluminum fuels [Wiersma-1998] produced leaching rates of 0.2 mg/m^2/d. The present release rates are comparable to the estimated rates from irradiated UAl$_x$ fuels in flow-through tests and drip tests on irradiated commercial UO$_2$ fuels.

Table 8. Release Rates for Uranium from Various Fuels under Various Test Conditions[a]

Sample[b]	Test	Release rate (mg/m^2/day)	Ref.
UAl$_x$	Drip	0.8-2.3	This report
UAl$_x$	Flow through, 25°C	2	[Wiersma-1998]
UAl$_x$	Flow through	8-27	[Wiersma-1998]
UAl$_x$[†]	Flow through, 25°C	0.1-0.2	[Wiersma-1998]
UAl$_x$[†]	Flow through	0.3-2[d]	[Wiersma-1998]
UO$_2$[†]	Drip	0.5-5[e]	[Finn-1995]
MOX[†]	Flowthrough	~0.7	[Gray-2000]
U-metal	Drip	110[d]	[Bowers-2000]

[a] The author recognizes the dubious choice of uranium as a marker for dissolution instead of more environmentally crucial isotopes such as ^{241}Am, ^{237}Np, or ^{99}Tc, but for the sake of consistency and in view of available data, uranium was chosen.
[b] Dagger indicates irradiated fuel
[c] Test temperatures 90°C unless indicated otherwise
[d] Calculated based on observed temperature dependence of 3-10 times the 25°C value [Wiersma-1998].
[e] Lower value based on measured uranium in solution while the upper value is estimated from the additional sorption of uranium on test vessel
[f] Rate normalized to the initial fuel geometric area and not adjusted for the large increase in the surface area that occurs during the corrosion and dissolution of metallic uranium fuel. The initial corrosion rate in H$_2$-saturated water is <5 mg/cm^2/h [Orman-1964].

C.   Colloid Formation

Colloids in the leachate were analyzed by coupling dynamic light scattering (DLS) and transmission electron microscope (TEM) techniques.   The colloid data for leachate from the 16-day sampling of UNAUT2 (fuel 571C) are shown in Figure 5. The signal intensity (scattering intensity) was as high as 161×10^3 counts per second. This value is quite high and indicates that there was a concentrated colloid population in suspension, much larger than was measured for leachates taken from UO_2 fuel tests. The signal reliability is good, suggested by the proximity of the measured data and the calculated baseline in Figure 5a and by reproducibility (not shown). The data fit for the autocorrelation function is good (Fig. 5b). The CONTIN solution suggests a bimodal population with mean effective radii of 7 and 275 nm and high variances (Fig. 5c).
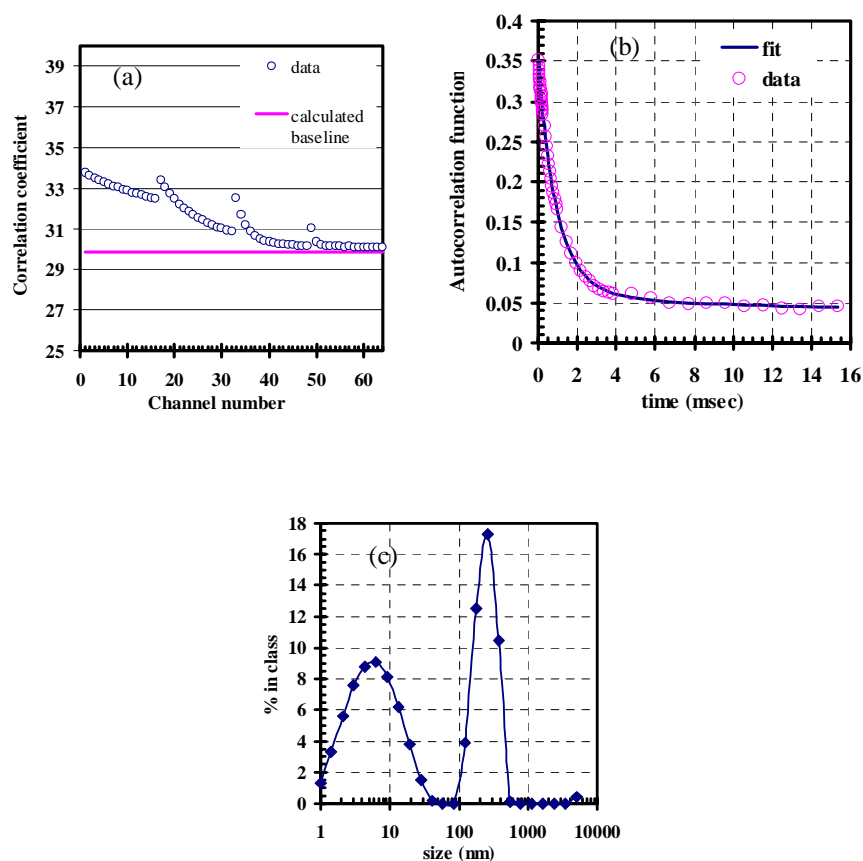
Fig. 5. Results of Colloid Analysis. (a) Collected counts (correlation coefficient), (b) autocorrelation function $G_1(t)$, and (c) size distribution expressed as % of intensity measurements aAssociated with a size range class for aliquot withdrawn from UNAUT2 after 16 days of testing.

As the samples age at room temperature and in plastic vials, the colloid population declines over time but it is still unclear whether these colloids are stable for long periods at room temperature. The reduced count rates for aged samples are given in Table 9. The decline in count rate may be attributable to two possible causes. One is the precipitation or dissolution of colloids from solution. The implication is that there is a general reduction in the total number of colloids. This can occur as a result of slow changes in solution chemistry or slow reaction kinetics. Another possible cause is dispersal of aggregates into smaller particles, since a change in count rate is directly proportional to a change in the particle size. Larger colloids, being more efficient scatterers of light, contribute to a higher count rate per number density of colloids than smaller colloids. This rate decrease would be balanced by the geometric increase in the total colloid density since large colloids are composed of many small colloids.

Dynamic light scattering (DLS) measurements from other sampling periods for UNAUT1-3 failed to converge on a replicable solution, indicating a polydisperse colloid population.

Table 9. Count Rate Data for Selected DLS Runs of UNAUT Leachates

Sample	Sampling Day	Days Stored	Laser Power (mW)	Adjusted Count rate ($x10^3$ cps @ 10mW)	Comments
UNAUT2	16	26	10	100	Good fit
UNAUT2	16	105	20	80.5	Good fit
UNAUT2	16	255	10	12	Unacceptable fit
UNAUT2	55	72	10	70	Unacceptable fit
UNAUT1	183	3	3	181.5	Unacceptable fit
UNAUB1	83		10	10.5	Unacceptable fit
Blanks			10	26	Unacceptable fit

To better characterize the colloids found in the drip tests, we analyzed a filtered leachate from UNAUT2 (day 16) for colloids using TEM (see Appendix D for a complete collection of TEM data). The colloid population appears to consist of silicates and alumino-silicates, either individual particles or large agglomerates. No uranium-bearing colloids were found. Figure 6 represents typical images. The DLS data and the TEM images are consistent with the existence of a population of individual particles in the single-digit nanometer range and of agglomerates as large as a few hundred nanometers. The morphology of the colloids varied from large, isolated spheres, to large fern-like structures, to agglomerates of tiny spheroids.
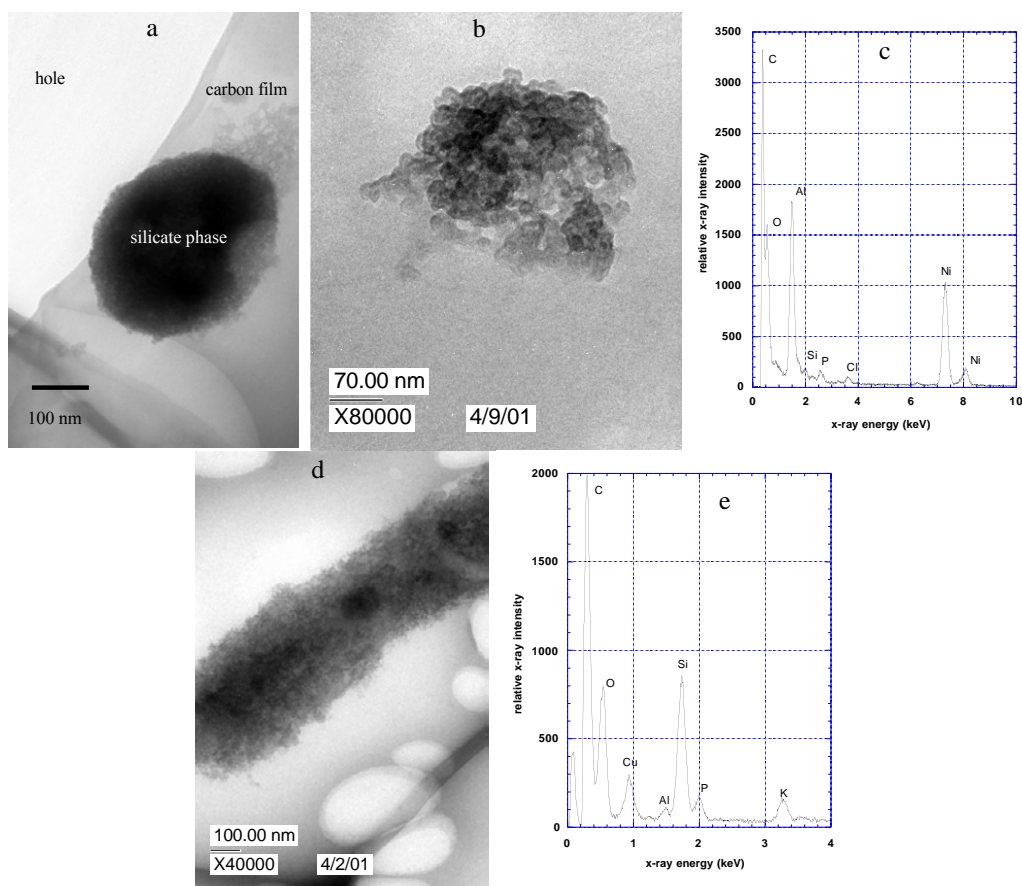
Fig. 6.   Examples of TEM Images of Silicate and Aluminosilicate Colloids: a) silicate colloid, b) aluminum-dominated colloid aggregate and c) EDS signature, d) diffuse, elongated aluminosilicate colloid, and e) EDS signature

The following section provides an electron microscopy investigation of the fuel surface and its progression during the testing program.

D.   Fuel Paragenesis

The original fuel surface is silvery and shiny, as is the aluminum cladding. Figure 7 shows the surface grain structure and cladding. The UAl$_x$ grains are nearly continuous across the fuel face. The exposed surface of individual grains varies from <1 to 100 µm along one length scale. Note the EDS signature for the UAl$_x$ grain, as this will be contrasted with that of altered grains.
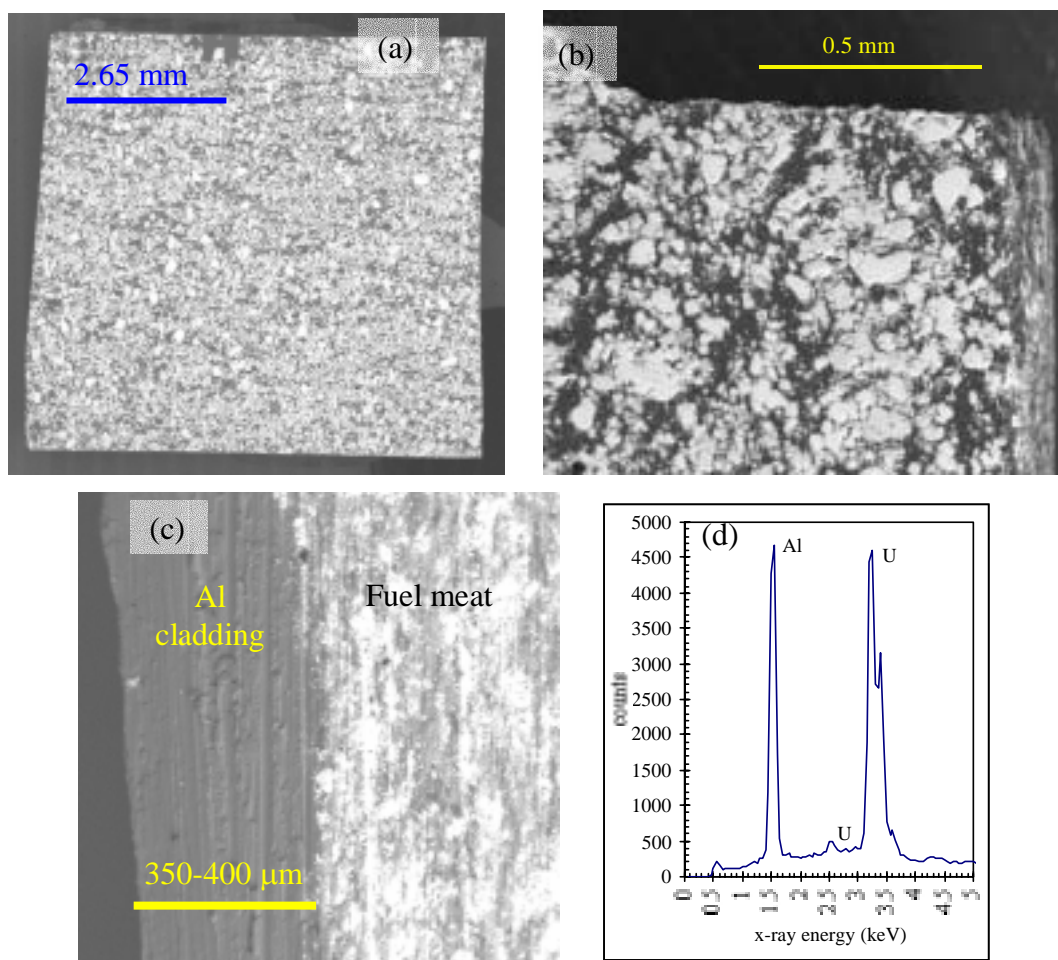
Fig. 7. Electron Micrographs of Fuel Specimen. (a) The fuel face has been polished to reveal the meat. UAl_x grains are indicated by the white, nearly continuous network. The gray regions are aluminum metal. (b) A closer view of the fuel face reveals the close packing of the UAl_x grains. (c) The transverse view of cladding shows the cladding-fuel meat interface. (d) The EDS analysis of UAl_x zones.

Once exposed to test conditions, the fuel surface tarnishes to a dark-gray speckled in white. Only after 183 days were rust-colored and yellow precipitates visible on isolated spots of the fuel surface. Mechanically, the fuel coupon remained stiff and did not spall noticeable products through 183 days of exposure to drip test conditions. Microscopically, the fuel corrosion was consistent with that described in Section I (a complete database of scanning electron micrographs generated under this program is provided in Appendix C). A coherent thin hydrogel of hydrous aluminosilicates formed within 16 days (see Fig. 8). Its thickness varied with time (< 100 nm-5 µm) and was dependent on the amount of water held up on the horizontal

fuel face, the efficiency with which the drip could wash away dissolved species, the time, the fuel sample, and the position on the fuel face. The hydrogel layer thickness did not exceed 5 µm. The hydrogel layer thickness that was measured is thus smaller than the actual gel thickness during test conditions due to shrinkage or syneresis from water loss (samples were stored in air prior to examination). The aluminosilicate hydrogel was readily observed on 60-100% of the surface, with the remainder exposed to the humid atmosphere directly or through an increasingly thin hydrogel layer. The hydrogel contained thick beds of amorphous and crystalline precipitates that covered about 30% of the fuel surface of UNAUT1 (Test 1) by 31 days. The surface coverage depended on the dryness of the surface and may have indirectly indicated reduced release rates for dissolved fuel components, because it signaled that the dripping water was not removing highly soluble dissolved products from the fuel surface. This would explain the very low release rate at 31 days in Figure 4. There was no evidence of oxygen-free zones on the fuel surface.
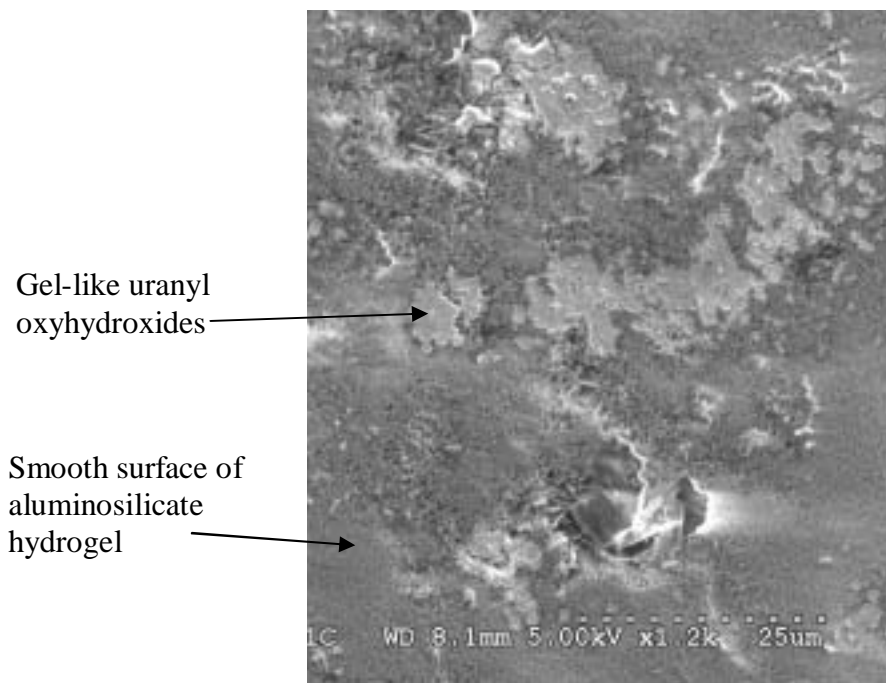
Fig. 8. Electron Micrograph of UAl$_x$ Fuel Surface Showing Aluminosilicate Hydrogel Morphology. As the hydrogel dried or underwent syneresis, cracks riddled the surface. (Magnification and scale bar shown in micrograph; accelerating voltage = 5 kV in secondary electron mode.)

Unlike what was observed initially in static and vapor corrosion tests [Mickalonis-1998], the UAl_x grains do not appear to be cathodically protected from corrosion under drip conditions. The surface UAl_x grains transformed quickly. Note that a single UAl_x grain may contain zones of UAl_2, UAl_3, and UAl_4; UAl_2 will oxidize and dissolve faster than UAl_3, which dissolves faster than UAl_4 [Openshaw-1964, Waber-1952]; zones within a particular UAl_x grain showed preferential corrosion in our tests. Uranium-rich alteration layers formed within 16 days on the surface of exposed UAl_x grains (see Fig. 9a). EDS analysis of the U-rich layer showed oxidation of the UAl_x and significant loss of Al compared with the original fuel shown in Figure 7. Given the previous work [Openshaw-1964] and solid-state and wet-oxidation corrosion mechanisms for UO_2 [Shoesmith-1992], this layer may be uranium oxides containing high impurity levels of Al, Si, and Ca. The cracks that define the alteration layer result from stresses associated with the disparate densities between layers. Above the U-rich layer, there persisted a thin hydrated oxide layer comprised of Al, Si, and some Ca, according to EDS analysis (Fig. 9). Indeed, as will be shown, this aluminosilicate gel layer contains uranyloxyhydroxides formed from uranyl ions released from the oxide surface layer.

Platelet crystals rich in uranium were found strewn across the fuel surface. They formed via the oxidation of the UAl_x, dissolution of the uranium oxide (likely $UO_{2.33}$), and precipitation as the uranyl-oxyhydroxides. Uranyl-oxyhydroxides are well-known to form as early corrosion products of uraninite (UO_2) [Finch-1999]. They were immediately (i.e., within 16 days) observed atop the UAl_x grains alone (see Figs. 8 and 10) and precipitated from circular uranium-rich gels. Another view of the uranium-rich gels in Figure 11 reveals their spheroidal nature. These patches eventually dried (note the surface cracks in Fig. 11), and crystallized to form small platelets 1-2 μm on edge. The platelet morphology is consistent with schoepite, $[(UO_2)_8O_2(OH)_{12}](H_2O)_{12}$, and its presence on the fuel surface was observed at each sampling. X-ray spectroscopy revealed other elements associated with these uranyl-oxyhydroxides, including Ca, Si, Al, and O.

Scrapings from part of the fuel surface (from UNAUT2 day 16) were analyzed by TEM. A micrograph appears in Figure 12. Based on electron diffraction and EDS analysis, disordered uranyl crystal phases were identified as dehydrated schoepite and becquerelite.
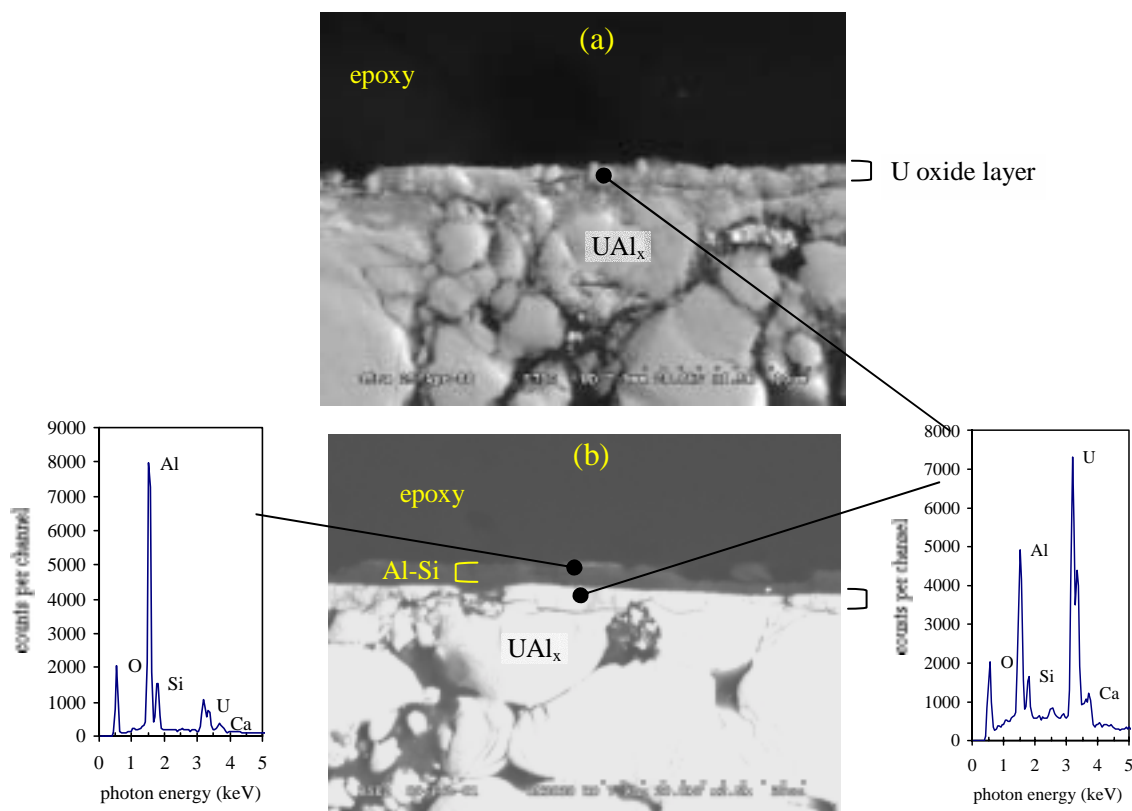
Fig. 9. Micrograph and X-Ray Spectra Showing UAl_x Surface after 16 and 183 Days. (a) Cross-sectional view of fuel profile showing surface of UAl_x after 16 days. The U-rich alteration layer shown is 1.5-2 mm in thickness. The hydrogel layer is not visible in this image due to the contrast level but is similar to (b) the transverse image of the reacted UAl_x layer after 183 days. Note the presence of Ca and Si in these alteration layers. (Magnification and scale bar shown in micrographs; accelerating voltage =20 kV.)
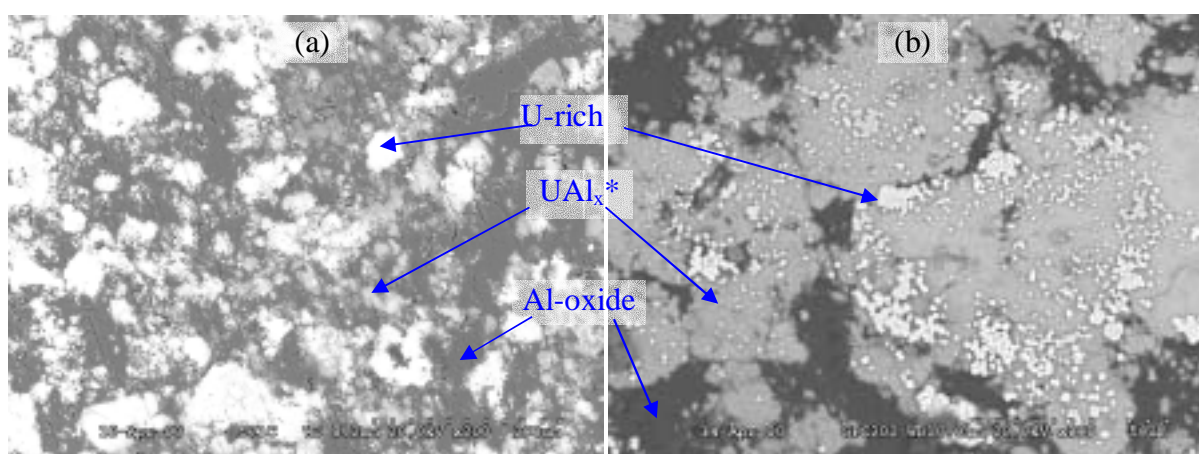
Fig. 10. Micrographs of UNAUT2 Fuel Meat Surface after 16 Days of Testing. White regions are rich in uranium, gray regions are obscured UAl_x grains (i.e., a view of the UAl_x through the thin aluminosilicate hydrogel), and black regions are oxidized aluminum seen through the hydrogel . (Magnification and scale bar shown in micrographs; accelerating voltage = 20 kV).
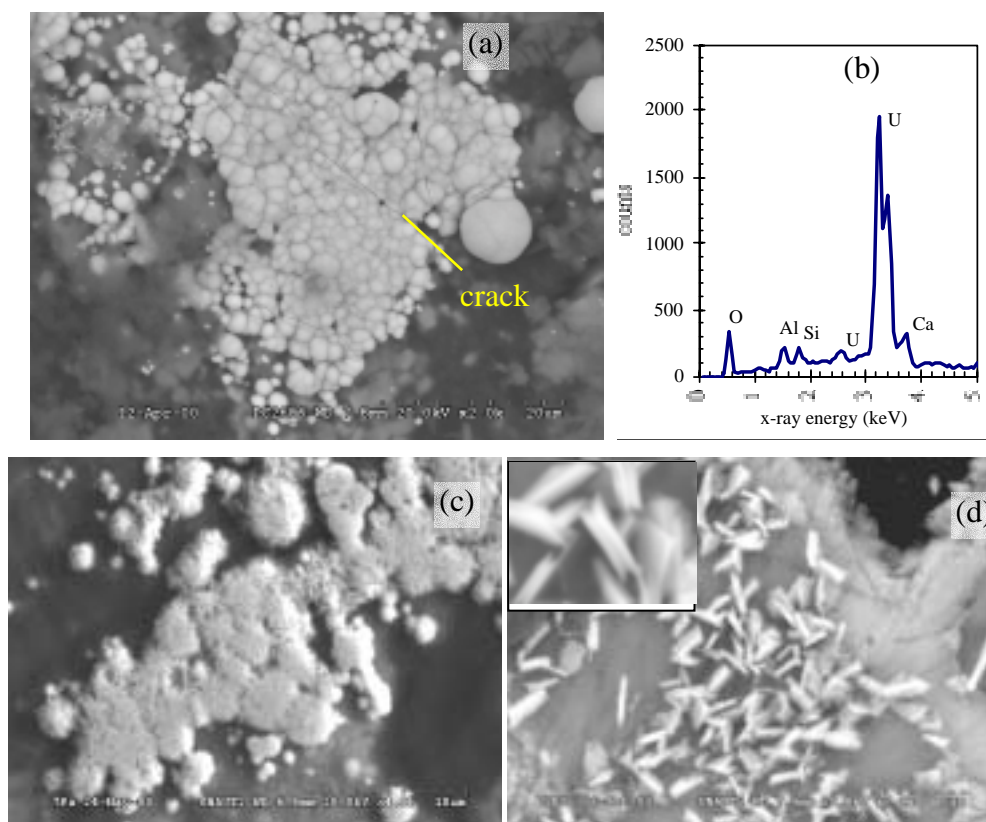
Fig. 11. Micrographs of Uranium-Rich Gels Showing Spheroidal Nature. (a) Uranyl-oxyhydroxides atop the corroded UAl$_x$ grains after 16 days on 571°C (UNAUT2) and (b) x-ray spectrum of the uranyl-oxyhydroxides. After a few days of air exposure, (c) platelets begin to crystallize and (d) were found across the fuel surface (UNAUT2) after 55 days. Note the platelet splitting, magnified in the inset, a phenomenon consistent with dehydration of the oxyhydroxides of uranium. (Magnification and scale bar shown in micrographs, accelerating voltage = 20 kV.)
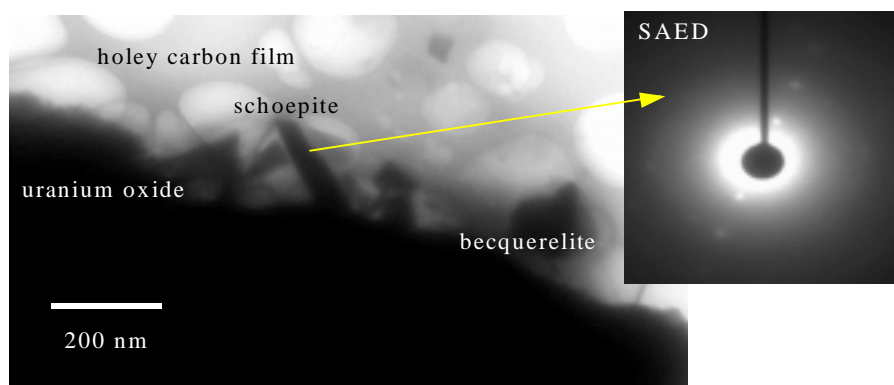
Fig. 12. Image Showing Alteration Phases on the Surface of Uranium Oxide. Left, TEM image; right, selected area electron diffraction.

Besides the occurrence of the platelets atop fuel grains, dissolved uranyl species diffused through the hydrogel, diffuse nodules formed (see Fig. 13) and platelet structures precipitated in the hydrogel during syneresis. These were scattered within isolated regions of the fuel and had dimensions ~1 μm on edge.
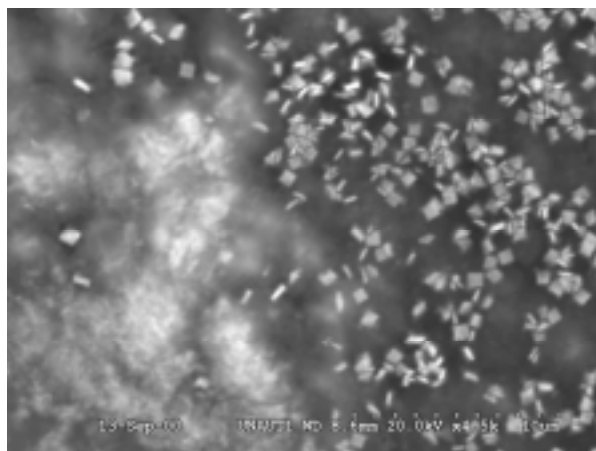
Fig. 13. Micrograph of Hydrogel Layer. Diffuse nodules of uranium crystallized to form smaller, more sparsely distributed platelet populations than shown in Figs. 10 and 11. These were seen as early as 16 days and persisted through the test. This particular area of the fuel was at the boundary between a dried gel (right) and moist hydrogel (left).

These relatively sparse platelet populations were not the unique habit for these uranyl-oxyhydroxides. Worm-like textures were observed in a couple of instances. This morphology can be viewed in Figure 14a and appears to be consistent with the dehydrated schoepite described by Taylor et al. [1995]. Other mineral structures, shown in Figure 14b, were observed in the 115-and 183-day samplings of UNAUT1 when the hydrogel had dissolved sufficiently. Highly fractured/altered UAl_x grains (Fig. 15b) gave rise to thin, elongated structures with triple terminations (Fig. 14c). Other elongated crystals with flat terminations were observed within and above the hydrogel (Fig. 14d).
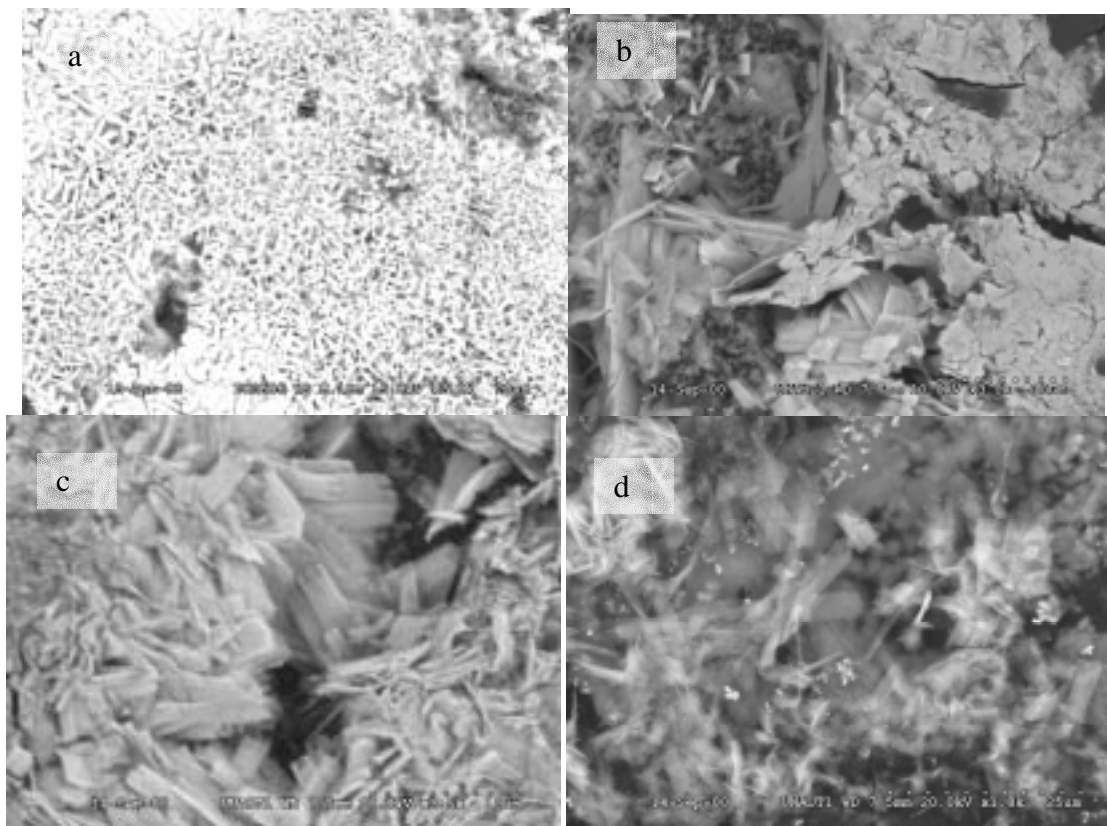
Fig. 14. Micrographs of Uranyl Structures Formed in Aluminosilicate Hydrogel. (a) Worm-like patches; these are similar in morphology to dehydrated schoepite found on polished UO_2 samples oxidized in humid air [Taylor-1995]. (b-c) Elongated uranium-rich crystals found after 183 days of testing. In (d), most of the crystals are buried within the Al-oxide gel layer, while most are exposed to the atmosphere in (b) and (c). (Magnification and scale bar shown in micrographs, accelerating voltage = 10-20 kV.)

There is evidence that dissolved uranium had sufficient time to concentrate and precipitate to form relatively dense beds of uranyl-oxyhydroxide crystals. One such patch grew within the thick evaporite region of the UNAUT1 fuel specimen. Shown in Figure 15b, the patch stretched more than 150 μm and was composed of thin platelets 3 μm on edge. During later sampling periods, this patch was reduced noticeably because of dissolution. This patch was growing inside the thick hydrogel that formed on this fuel specimen.
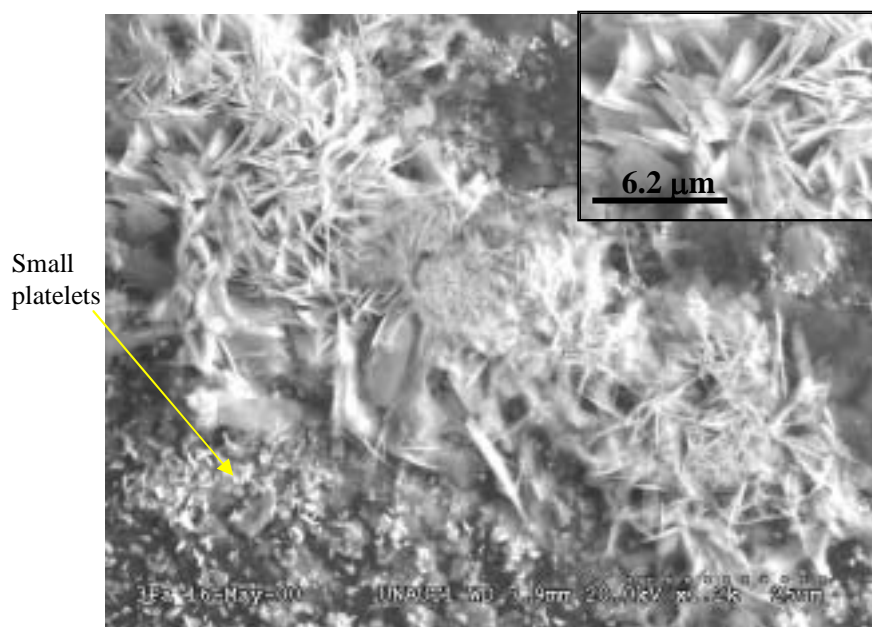
Fig. 15. Area of UNAUT1 Fuel Specimen after Exposure for 115 Days.
The inset provides a higher magnification of the platelets.
(Magnification and/or scale bar shown on micrographs, acc.
voltage = 20 kV.)

Just below the patch shown in Figure 15 is a swarm of much smaller platelet growths. The dimensions of these uniform plates is 2 mm square and <250 nm in thickness. Within the EDS limits, these growths are identical in composition to the platelets in Figures 11 and 12. The EDS spectrum of the UAl_x revealed Si and Ca in the U oxide (i.e., other silica and calcite precipitates or uranyl-silicates or calcium uranyl-oxides like becquerelite).

X-ray diffraction was attempted after placing the fuel directly on an aluminum diffraction planchet. The sensitivity was insufficient to detect the diffraction from the uranyl-oxyhydroxide crystals.

V. SUMMARY AND CONCLUSIONS

The degradation of the UAl_x fuel under the action of dripping well water is characterized by the oxidation of the fuel grains and aluminum to form a variably thick aluminosilicate hydrogel containing hydrated uranyl-oxyhydroxides. The initial corrosion of UAl_x occurs by the diffusion of water and oxygen-derived species (although water species probably dominate). If metallic aluminum is released from the UAl_x and from the intergranular Al, it will oxidize and hydrate to form a hydrogel. Dissolution and reprecipitation of the hydrogel lead to the formation of an aluminosilicate hydrogel. These reactions can be written as

$$UAl_x + \left(\frac{3}{2}x + 2 + n\right)H_2O \rightarrow UO_2 + \left(\frac{3}{2}x + 2\right)H_2 + \left(\frac{x}{2}Al_2O_3\right) \cdot nH_2O \qquad (8)$$

$$Al(OH)_3 \bullet nH_2O + SiO_4^- \rightarrow Al(OH)_2 SiO_4 \bullet nH_2O + OH^- \qquad (9)$$
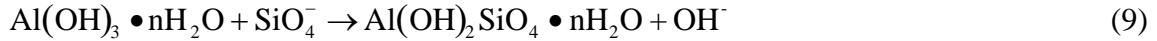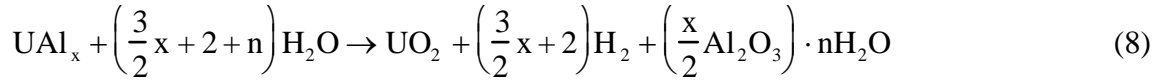
where $Al_2O_3 \bullet 3H_2O$ is identical to $2Al(OH)_3$. Inclusion of silica within the gel would thus require the release of hydroxyl anions and a concomitant rise in pH. Depending on the pH, the hydrogel may be buffered by the dissolution of aluminum in higher pH solution and formation of Al-hydroxide complexes and hydrated precipitates. Thermodynamically, both the aluminum and uranium favor oxidation [Openshaw-1964]. The Gibbs free energies of oxidation for aluminum and uranium are high given the propensity of both metals to form oxide layers. The diffusivity of aluminum in UAl_x is exceeded by that of uranium, meaning that uranium atoms will diffuse more readily to the reaction front to react with diffusing oxygen species [Openshaw-1964]. This behavior is dependent on the U/Al ratio. A higher ratio afforded by UAl_2 and UAl_3 will inhibit selective corrosion of aluminum. In burned Al-fuels, UAl_4 will dominate and will favor selective oxidation and may promote the formation of a passive layer. Given the faster diffusion of uranium in UAl_x compared with aluminum, it has been postulated that a thin layer of UO_2 would develop at the water-UAl_x interface [Openshaw-1964]. We believe that our solution conditions do not promote the growth of a thick UO_2 layer since such a layer could not be confirmed in our experiments. Oxidation to a higher state is expected to be quite rapid since no crystallographic rearrangement is necessary. Moreover, the solution chemistry – oxidizing with prevalent

hydroxide species -- favors the continued oxidation of this layer and rapid dissolution of the uranyl species where

$$3UO_2 + H_2O \rightarrow U_3O_7 + 2H^+ + 2e^- \qquad (10)$$

$$UO_{2.33} + 2H^+ \rightarrow 3UO_2^{2+} + H_2O + 4e^- \qquad (11)$$
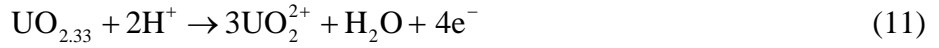
The uranyl cation is released into the hydrogel or remains adsorbed to form oxyhydroxide precipitates.

$$UO_2^{2+} + \frac{1}{2}O_2 + xH_2O + 2e^- \rightarrow UO_3 \bullet xH_2O \qquad (12)$$
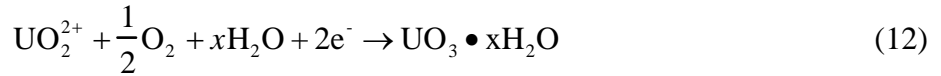
The oxyhydroxides are preferentially formed at defect sites on the layer of oxidized UAl_x, a phenomenon best illustrated in Figures 10 and 16 where the precipitated material is isolated to regions immediately above the UAl_x grains and to specific regions of the grain itself.

The uranyl cations or complexes that detach from their site of origin diffuse through the gel, where they can be washed from the fuel surface or crystallize as the hydrogel dries, as shown in Figure 13.

U-oxyhydroxide
platelets
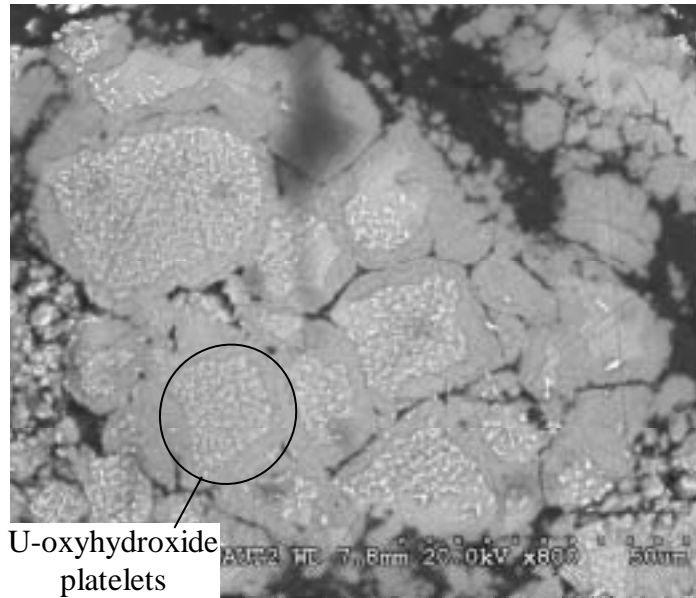
Fig. 16.   Precipitation of Uranyl-Oxyhydroxide Crystals at Defect Sites Created by Corroding UAl_x. The position of these crystals at the center of the grain is consistent with the position of UAl_2 regions of the UAl_x grain, which are thermodynamically less stable to corrosive attack.

The prevalence of dissolved calcium and silicates leads to the formation of becquerelite, which was present as early as 16 days into the test, and eventually uranophane or other uranyl-silicates, which may be kinetically limited.

The availability of water afforded by the hydrogel disfavors the crystallization process and promotes the existence of the uranyl species in a gel-like state. Assuming that the water content of the aluminosilicate hydrogel is maintained, the hydrated uranyl gels are given an environment in which to grow and eventually (when dried) crystallize larger oxyhydroxide crystals as shown in Figure 15. Sorption of uranyl species may also serve as nucleation sites for crystallization.

Silica-alumina colloids (i.e., silica colloids with aluminum substitutions) can have base-exchange capacities explained by the substitution of aluminum in terminal positions of the lattice [Plank-1947]. The composition of the gel will reflect the relative concentration of silicate and aluminate in the solution from which it was formed [Krznaric-1997]. In the UAl_x fuel, EDS revealed that the hydrogel is dominated by aluminum, but some areas have comparable silicon concentrations, which suggests that the local dissolved silicon concentration in the hydrogel varied with position on the fuel surface. In the pH range of EJ-13, the gelation or syneresis time is probably near its minimum and could be less than a few hours [Plank-1947]. This is significant because it reveals that the hydrogel has time to stabilize between incoming drips and may not form as readily under a flowing or bathtub system. The peptization of alumina-dominated gels is not always possible and is complex [Morgado-1997], the process being highly dependent on the structure of the amorphous, hydrated Al_2O_3.

Peptization of the gel by the dripping water results in the formation and release of colloids, often referred to as "primary" colloids. It is impossible to predict the size distribution of these colloids from previous studies, although bimodal and multimodal distributions have been produced previously from peptized aluminosilicate gels [Morgado-1997]. Those results are consistent with the present data where the polydispersity of colloid samples made analysis by DLS mostly ineffective. According to Plank's work [1947] on silica-alumina gels, aluminum from the gel is much more soluble during acidic washing. The electron microscopy of the colloids (see Fig. 5) appears to corroborate this finding, since most colloids observed were dominated by silicon, even though the hydrogel is dominated by aluminum. In addition to peptized colloids, the aluminum and silicates dissolved from the fuel would be free to hydrolyze

in the reservoir at the bottom of the vessel. Although no uranium was detected on the colloids, the adsoprtion of radionuclides is certainly possible. In fact, it would be expected, given the zeolitic properties of aluminosilicate hydrogels. We would not be surprised to find that these colloids have appreciable cation exchange capacity.

With regard to the rate of release of radionuclides, uranium is our only available marker. Comparing uranium release from UAl_x fuel to other fuel types, we find that it is comparable to irradiated UO_2 fuels. Uranium was released into solution at an average rate among the three experiments of 0.97 mg/m^2/d (range: 0.23-2.92 mg/m^2/d).

In short, except for tarnishing, the UAl_x fuel surface was changed little after half a year of testing. The fuel corrodes by first forming a coherent hydrous aluminum oxide layer or hydrogel and a layer of uranium oxide on exposed UAl_x grains. The thickness and coherence of the hydrogel layer varied with the drip conditions and position on the sample. Uranyl-oxyhydroxide platelets were found strewn atop corroded UAl_x grains and spread within the thin hydrogel. Released uranium was comparable to that of UO_2 fuels. Colloids were found and were composed of both silica (dominant) and aluminosilicates. The long-term stability of these colloids and fundamental properties is still to be determined.

VI. FUTURE WORK

The program is tentatively scheduled to test fully radioactive samples from the bench-scale melt-dilute experiments being conducted by the Savannah River Site. The release of radionuclides will depend not only on the corrosion of the UAl_x grains, but also on fission and neutron capture product disposition in the fuel. Neutron poison material may affect radionuclide release, as well. Future work includes testing of irradiated melt-dilute fuels, comparing primary alteration phases with this work, and assessing fission product and actinide disposition among secondary solid phases, colloids, and dissolved species. For a short discussion on the melt-dilute process, see Appendix B.

ACKNOWLEDGMENTS

REFERENCES

Adams-1999
T. M. Adams, H. B. Peacock, Jr., F. C. Rhode, and N. C. Iyer, Mat. Res. Soc. Symp. Proc., 556 (1999) 495–503.

Bowers-2000
D. Bowers, Argonne National Laboratory, private communication of unpublished work (August 2000).

Colmenares-1984
C. A. Colmenares, Prog. Solid St. Chem. 15 (1984) 257–364.

Finch-1999
R. Finch and T. Murakami, "Systematics and Paragenesis of Uranium minerals," in Reviews in Mineralogy, 38 (1999) 91-179.

Finn-1994
P. A. Finn, J. C. Hoh, J. K. Bates, S. F. Wolf, ANS DOE Spent Nuclear Fuel Meeting: Challenges and Initiatives, Salt Lake City, UT, December 13-16, 1994, American Nuclear Society, in Proceedings, ANL/CMT/CP-83895, 421-429 (1994).

Finn-1995
P. A. Finn, E. C. Buck, J. C. Hoh, and J. K. Bates, in the Proceedings to Global 1995, International Conference on Evaluation of Emerging Nuclear Fuel Cycle Systems, Versailles, France, September 11–14 (1995).

Gaiter-1989
G. Gaiter, A. Francois, M. Deliens, and P. Piret, Mineralogical Record, 20, July–August (1989).

Gray-2000
W. J. Gray and D. W. Wester, Proc. DOE Spent Nuclear Fuel and Fissile Material Management, San Diego, CA, June 4–8 (2000).

Krznaric-1997
I. Krznaric, T. Antonic, and B. Subotic, Zeolites 19 (1997) 29–40.

Lam-1998
P. Lam, R. Sindelar, and K. Barrett, "Corrosion of Aluminum-Uranium Alloys in Water Vapor at 200 °C," WSRC-MS-98-00858 (1998).

Mickalonis-1998
J. Mickalonis and B. Wiersma "Test Protocol for Aluminum Based Spent Nuclear Fuel," WSRC-MS-98-00860 (1998).

Morgado-1997
E. Morgado, Jr., Y. L. Lam, and L. F. Nazar, J. Colloid Inter. Sci., 188 (1997) 257–269.

Openshaw-1964
P.R. Openshaw and L.L Sheir, Corros. Sci. 4 (1964) 335–344.

Orman-1964
S. Orman, Uranium Compatibility Studies Part 2: The Effect of Water Vapour Pressure in an Oxygen Free Atmosphere on the Corrosion Rate of Uranium at 100 °C, Atomic Weapons Research Establishment, United Kingdom Atomic Energy Authority (1964).

Plank-1947
C. J. Plank, J. Colloid Sci. (1947) 413–427.

Shoesmith-1992
D. W. Shoesmith and S. Sunder, J. Nucl. Mater. 190 (1992) 20–35.

Sunder-1981
S. Sunder, D. W. Shoesmith, M. G. Bailey, F. W. Stanchell, and N. S. McIntyre, J. Electroanal. Chem., 130 (1981) 163–179.

Taylor-1995
P. Taylor, D.D. Wood, and D.G. Owen, J. Nucl. Mater. 223 (1995) 316–320.

Taylor-1991
P. Taylor, D.D. Wood, and D.G. Owen, J. Nucl. Mater. 183 (1991) 105–114.

Taylor-1989
P. Taylor, D. Wood, A. Duclos, and D. Owen, J. Nucl. Mater. 168 (1989) 70–75.

USDOE-2002
U.S. Department of Energy, National Spent Nuclear Fuel Program, program web site, http://nsnfp.inel.gov/ (2002).

Vinjumari-1983
K. Vinjumari and R. Hobbins, "Aqueous Corrosion of Uranium Aluminide Fuel," Nucl. Techn. 62 (1983).

Waber-1952
J. T. Waber, "Review of the Corrosion of Uranium and Its Alloys," Los Alamos Scientific Laboratory Report, Los Alamos National Laboratory (1952).

Wiersma-1998
B. Wiersma, "Preliminary Report on the Dissolution Rate and Degradation of Aluminum Spent Nuclear Fuels in Repository Environments (U)," WSRC-TR-98-00290 (1998).

Wolf-1998
S. F. Wolf, J. Radioanal. Nucl. Chem., 235, 1-2 (1998) 207–212.

APPENDIX A

GENERAL PROPERTIES OF THE ALUMINUM-BASED FUELS

WITHIN THE DOE INVENTORY

Aluminum based nuclear fuels were conceived for operation in low-temperature reactors, namely, test and research reactors within DOE and in research institutions around the world. For an exhaustive discussion of the aluminum-based nuclear fuels see Samoilov [1968]. The fuel fabrication method is peculiar to dispersion-type fuels, of which Al-based fuels are a subcategory. Casting was the initial manufacturing technique but powder metallurgy is almost exclusively in use today. Of the different geometries, the thin-plate design is predominant. These plates, as thin as 0.060 in., offer many attractive features for use in this type of nuclear reactor assembly. The fuel meat is as thin as 0.020 in. and consists of fissile fuel powders and aluminum matrix powders pressed together. The porosity that is inherent with powder technology is advantageous for this application and serves a dual purpose. Initially, the fuel meat contains sufficient porosity to allow for easy fabrication. During irradiation, the porosity helps to accommodate fuel swelling, resulting from density changes in the fuel and gas evolution from fission products.

Typically, aluminum-clad spent fuels were stored in the light-water-filled storage basins for cool-down periods of 9-12 months prior to reprocessing [Howell-1993]. Because of the short turnaround times in previous years, the basin waters were not fitted with special filters to maintain ultra-cleanliness, although the water chemistry was controlled. However, with the cessation of reprocessing activities, some fuel elements have been in underwater storage for 10–12 years. Water conductivity in the SRS basins was at least 200 mS/cm before measures were taken to clean up the pools. The Receiving Basin for Off-site Fuel (RBOF) at SRS is currently kept at 1-3 mS/cm and has never experienced corrosion problems in almost 20 years of storing aluminum fuels [Howell-1999]. Other basins around the country that stored aluminum fuels converted to sophisticated water purification systems to control the chemistry and have been very successful in avoiding aluminum corrosion.

The aluminum fuels were fabricated in many different geometries. The melting temperature of the aluminum constrained the dimensional thickness to very thin elements

because of the potentially excessive centerline fuel temperatures reached during reactor operation. Most were thin (0.06-0.1 in.), flat plates a few inches wide and up to a couple feet long. Some were thin and curved, as in the Mark III fuel elements for the Advanced Test Reactor, which had curved radii of 2.6-4.6 in. and a length of 49.5 in. [Hobson-1964].

For plate-type fuels, the fuel meat is intimately bonded to the cladding in a picture frame design (see Fig. A1). Subsequent roll bonding of the plate metallurgically seals the meat to the cladding frame. Heat transfer from the meat to the coolant is excellent because of the thermal conductivity of the cladding, the intimate contact between the meat and cladding, and the thickness of the fuel plate. The aluminum also offers excellent chemical stability in aqueous solution.
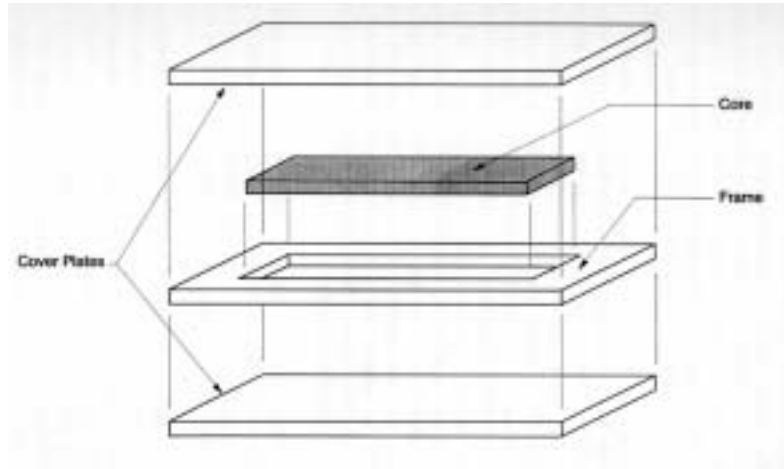
Fig. A.1. Picture Frame Design Used to Fabricate Al-Based Fuel Plates

Table A.1. Thermal Conductivity and Density Data for Some Fissile Dispersions

Material	Conductivity (W/m/K)	Density (g/cm^3)
UAl_x	150	5.5
UO_2	~10	10.0-10.8
U_3O_8	1.8	8.4
UC	20-25	10.2
UC_2	34	10
UN	21	14.3
U_3Si	15	15.6
U_3Si_2	14.7	12.2
US	10	10.8
PuO_2	4.2	11.5

Many types of Al dispersion fuels have been studied in the past (see Table A.1). Of them, there are three predominant types in the DOE inventory. The first is the oxide fuels composed of U_3O_8 or UO_2 dispersions in aluminum. The UO_2 dispersion was used sparingly and does not represent a significant volume of DOE fuel. The U_3O_8 fuels have been studied very little with regard to water corrosion. The second category is the silicide fuels, which are composed of U_3Si_2 or U_3Si dispersions in aluminum. The U_3Si dispersions also were not fabricated in large quantities as they exhibited detrimental irradiation swelling characteristics. The U_3Si_2 is the choice of fuel composition in today's market for test and research reactors employing aluminum fuels because of the superior irradiation and uranium loading characteristics. The silicides are not considered a high-priority fuel for testing. The final type is the intermetallic uranium-aluminide or UAl_x fuels. Generally, these comprise dispersions of UAl_2 (d-phase), UAl_3 (e-phase), and UAl_4 (z-phase), or simply UAl_x, in aluminum but can also be cast to form an aluminum-uranium alloy.[1] The aluminide fuels are considered top priority for various reasons, including the relative volume of these fuels in the DOE aluminum inventory (see Table A.2), their high enrichment, and their properties related to the final alloy form from the melt-dilute process (proposed by Savannah River as the stabilizing waste form option for the aluminum-based fuels; see Appendix B).

Table A.2. Estimated DOE Inventories for Aluminum-Based Fuels to 2035. Comparative data are provided for other high-priority fuels in the DOE inventory.

Fuel Type	No. of Units	Mass (kg)	Volume (m^3)	Fissile Mass (kg)
Al-U Oxide	7,600	58,000	96	2,600
UAl_x	18,000	130,000	150	6,000
U-Silicide	7,400	47,000	53	1,200
N-Reactor U metal	100,435	2,284,500	218.7	25,123
Mixed Oxide	2,620	116,100	35.1	2640

---

[1] The melt-dilute process converts all aluminum fuels into cast eutectic aluminum-uranium metal.

Oxide-Based Al Fuels

The rapid reaction between UO_2 fuel particles and the aluminum matrix during irradiation, forming U_3O_8, was catastrophic to the integrity of these fuels, leading to swelling and pillowing. For this reason, the UO_2 fuels were dropped as candidate materials. This problem was alleviated by using U_3O_8 powders. The Cermet fuels, as they are often called, were fabricated as early as 1952. The inherent porosity of these ceramic U_3O_8 particles results in high diffusion of volatile fission products, although much less so than in commercial reactor UO_2 fuels, which operate at extremely high temperatures and thermal gradients. During irradiation, several important phenomena transpire that affect fission product release during corrosive attack of the fuel. The first involves the chemical/metallurgical evolution of the fissile U_3O_8 grains. In high-burnup fuels, the porosity of the fuel grain and the evolution of gaseous fission products lead to the formation of small fission bubbles and their eventual coalescence into a large fission bubble.

Accompanying this phenomenon is the redox interaction between the aluminum and the oxide fuel. This reaction leads to the formation of reduced uranium oxides (Eq. A.1) and, eventually, aluminide regions in the fuel grain at the expense of the protective aluminum matrix, as described in Equation A.2.

$$\begin{aligned} U_3O_8 + \frac{5}{6}Al &\rightarrow \frac{3}{4}U_4O_9 + \frac{5}{12}Al_2O_3 \\ \underline{U_4O_9 + \frac{2}{3}Al \rightarrow 4UO_2 + \frac{1}{3}Al_2O_3} \\ 4Al + 3U_3O_8 &\rightarrow 9UO_2 + 2Al_2O_3 \end{aligned} \tag{A.1}$$

$$\begin{aligned} 4Al + 3U_3O_8 &\rightarrow 9UO_2 + 2Al_2O_3 \\ \underline{16Al + 3UO_2 \rightarrow 3UAl_4 + 2Al_2O_3} \\ 52Al + 3U_3O_8 &\rightarrow 9UAl_4 + 8Al_2O_3 \end{aligned} \tag{A.2}$$
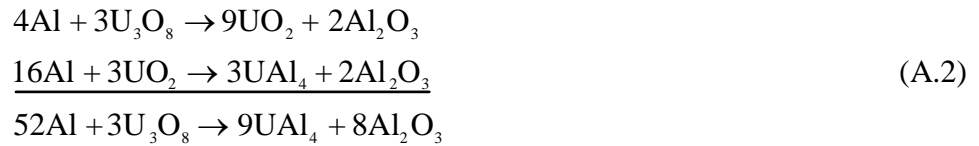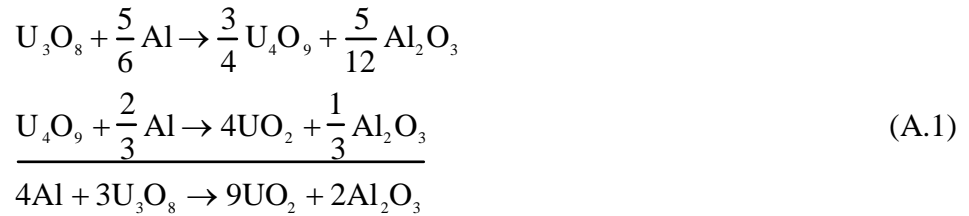
Perplexing enough, the formation of UO_2, as shown in Equation A.1, progresses to completion before any UO_2 reacts further with aluminum to form the intermetallics. In addition, even though the amount of UO_2 is the same as would be present in UO_2-based dispersions, the growth of the fuel is reduced by an order of magnitude—a phenomenon not well understood [Belle-1961]. This phenomenon explains the consumption of aluminum in high-burnup fuels leading to

a discontinuous network of aluminum and thus a loss of protection. Direct evidence for this was documented by Hofman [1986].

Another result of the irradiation and chemical transformation of the fuel is grain refinement (see Fig. A.2). Grain refinement results in reduced grain sizes, large grain boundaries, and an overall increase in grain surface area. Coupled with the porosity of the U_3O_8 grain and the disappearance of the protective aluminum matrix, grain refinement provides a facile path for leaching of fission and activation products and high surface area for grain alteration.
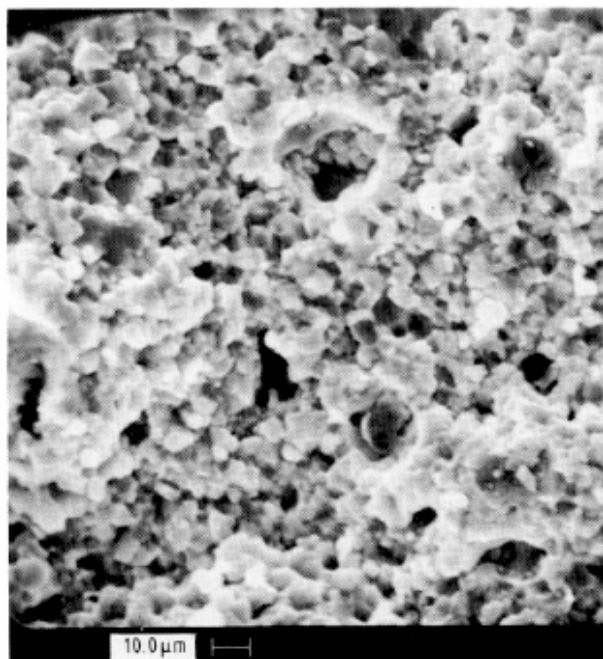
Fig. A.2. SEM Micrograph Showing Grain Refinement in a Transformed U_3O_8 Fuel Particle [from Hofman-1994].

Another important property of the U_3O_8 fuels is the oxidation state of the uranium and its relation to dissolution kinetics. For uranium to dissolve appreciably, it must first exist in the hexavalent state, as in U_3O_8 and UO_3. The oxide of U_3O_8 is a complicated molecule. In terms of acidic dissolution, it was initially thought of as a mixture of two UO_3 and one UO_2 (i.e., mixed hexa- and tetravalent states). However, x-ray and magnetic measurements contradicted this philosophy [Katz-1951]. Instead, the U_3O_8 is better interpreted as a mixture of hepta- and

hexavalent states as $U_2O_5 \bullet UO_3$. Therefore, in order for UO_2 to dissolve it must transform, at least partially, into the hexavalent state (U_3O_8 and UO_3). Relative to uranium metal fuels where uranium exists in the zero-valent state, U_3O_8 is in a much more thermodynamically favorable position to dissolve when the rate is normalized to surface area.[2]

Silicide-Based Al Fuels

U_3Si

One of the goals of the DOE New Production Reactor (NPR) and Reduced Enrichment Fuels for Research and Test Reactors (RERTR) programs was to develop fuels with the metallurgical characteristics that would allow for very high uranium loading and burnup to counteract the lowered fuel enrichment. Investigation of the U_3Si fuels produced the desired loading characteristics, but these fuels did not possess satisfactory irradiation characteristics due to high fuel swelling. As-fabricated porosity was not sufficient to overcome the "break-away" swelling that these fuels experienced. There is not a significant amount of U_3Si fuels in the DOE inventory.

U_3Si_2

To overcome the undesirable swelling characteristics of the U_3Si fuels, the U:Si ratio was reduced to produce U_3Si_2 fuels. These fuels displayed very admirable irradiation characteristics and were much different than the oxide fuels in many ways: (1) There does not appear to be a significant reaction between the silicide fuel and aluminum matrix, even after very high burnup (90%). (2) Fission bubbles form in these fuels but do not coalesce or present swelling problems. (3) The as-fabricated porosity is sufficient to accommodate the modest swelling. (4) There is some evidence that the peripheral regions of the silicide grains may be metallurgically transformed during irradiation by the diffusion of matrix aluminum and replacing the silicon to form $U(Al, Si)_3$ compounds [Snelgrove-1987].

Almost no data have been obtained on the aqueous corrosion of these fuels or the evolution of alteration layers on the silicide materials. Snelgrove et al. [1987] performed short-

---

[2] It is worth clarifying the importance of surface area. For instance, metallic uranium will corrode when in contact with liquid water to form tiny spalled UO_2 products that characteristically are porous structures with high surface area. The high surface area will greatly increase the absolute rate of dissolved uranyl ions over large grains. Therefore, metallic uranium may dissolve faster than U_3O_8 simply because of a surface area effect.

term corrosion tests by submerging U_3Si_2 samples (with a hole drilled through the meat) in distilled water at 100°C over a period of one week. They noted no radioactivity in the water or on the plate, with only a noticeable darkening of the plate surface.

Aluminide Fuels

The first-generation research and test reactors employed Al-U alloy fuels. The first of these was the Materials Test Reactor (MTR) in 1952. The alloy fuels consisted of UAl_3 and UAl_4 grains in metallic solution with aluminum. The need for higher-density fuels led to the use of powder metallurgical techniques and the UAl_x fuels. Metallurgically, the UAl_x and U-Al alloy fuels are similar, and after short irradiation times, they are essentially identical. The phase diagram for uranium and aluminum in Fig. A.3 shows that the thermodynamically stable mixture contains UAl_4 in aluminum, but equilibrium is rarely achieved. Instead the fuel consists of a mixture of UAl_2, UAl_3, and UAl_4, with the predominant component being UAl_3 (60-75%) at preirradiation [Hofman-1994].

Fig. A.5. Binary Phase Diagram for Aluminum and Uranium [from Hofman-1994].
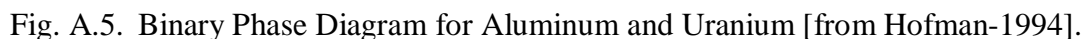
During irradiation, metallurgical transformations progress toward higher stoichiometries of UAl_x and, therefore, lower densities. Radiation-induced phase transformation causes the UAl_2 grains to convert to UAl_3, and UAl_3 to convert to UAl_4. This leads to a growth in fuel grain size as depicted in Fig. A.4. Surprisingly, little swelling is associated with this conversion. The excellent swelling and fuel loading characteristics of the UAl_x fuels led to their widespread use.
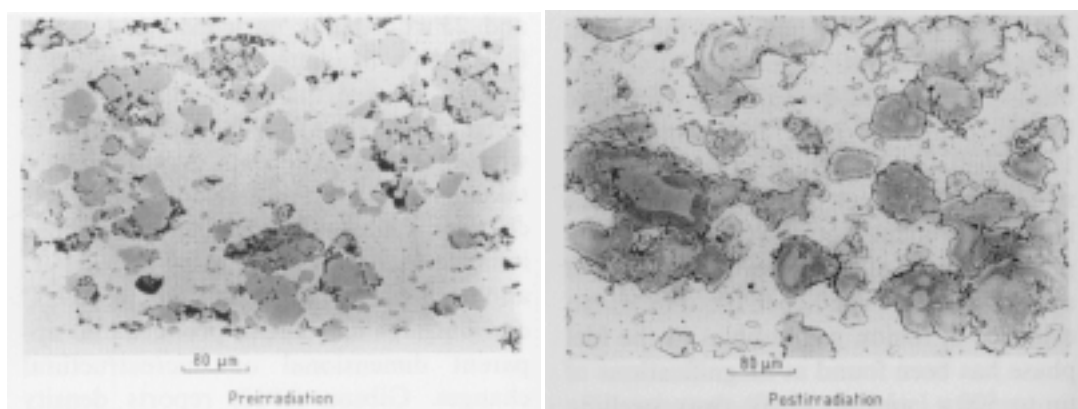
Fig. A.4.   Pre- and Post-Irradiation SEM Micrographs of UAl_x Fuel Showing Fuel Grain Growth [from Hofman-1994]. Before irradiation, many fuel grains are <80 mm, while there are few of that size after irradiation.

The phase transformation that occurs in these fuels reduces the amount of protective aluminum matrix ($UAl_x + Al \rightarrow UAl_{x+1}$) but less dramatically than observed with the U_3O_8 fuels. Figure A.5 is an excellent illustration of these various UAl_x stoichiometries.
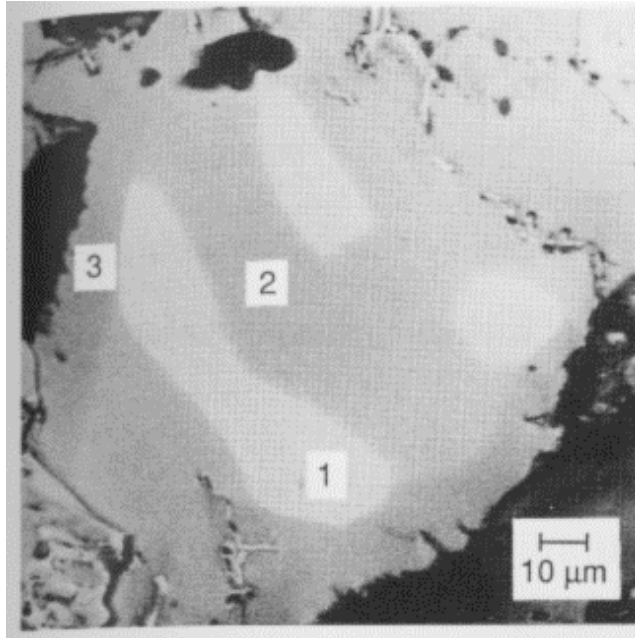
Fig. A.5.   SEM Micrograph of Individual UAl$_x$ Fuel Grain After
Irradiation.   Region 1 is UAl$_2$, region 2 is UAl$_3$, and
region 3 is UAl$_4$.   No free uranium could be detected
[from Hofman-1987].

The UAl$_4$ crystallography is that of a body-centered orthorhombic structure with unit cell dimensions of a=4.41 Å, b=.27 Å, and c=13.71 Å [Reinke-1963].   Each uranium atom is surrounded by thirteen aluminum atoms at a minimum distance of 3 Å.   The theoretical density is 6.12 g/cm^3 but the measured density is 5.7 $\pm$ 0.3 g/cm^3.   It has been surmised that the discrepancy between the theoretical and observed density accounts for the fuel's ability to adsorb fission products in a highly stable configuration without release.

Even at high burnup (70%) there is no evidence of fission bubble formation.   All the fission bubbles and products appear to be completely soluble in the aluminide grains.   Hofman [1987] explored irradiated fuel grains for evidence of fission bubbles and was unsuccessful except for small, isolated regions in the fuel where UO$_2$ particles apparently existed (see Fig. A.6).   Hofman attributed the existence of these UO$_2$ particles to the fabrication process (which was conducted in air) and subsequent oxidation of uranium.   He believed that if the fuels were fabricated in an inert atmosphere, the UO$_2$ particles would not have been present during irradiation, and no fission bubbles would form.
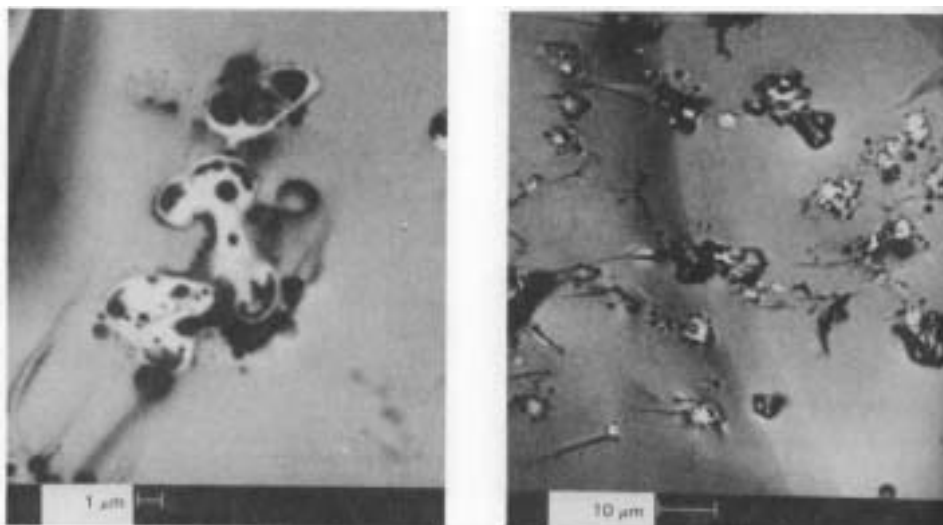
Fig. A.6. Micrographs Showing Fission Bubbles Found in Isolated Regions of UAl$_x$ Fuel Grains Where UO$_2$ particles Were Found. These marked the only occurrence of fission bubbles in aluminide fuels and were of minor importance [from Hofman-1987].

REFERENCES

Belle-1961
J. Belle, *Uranium Dioxide: Properties and Nuclear Applications*, U.S. Government Printing Office, Washington, DC. (1961).

Hobson-1964
D. O. Hobson, R. L. Heestand, C. F. Leitten, *Fabrication Development of U$_3$O$_8$-Aluminum Composite Fuel Plates for the Advanced Test Reactor*, Oak Ridge National Laboratory Report ORNL-3644 (1964).

Hofman-1986
G. L. Hofman, Nucl. Technol., 77 (1986) 110–115.

Hofman-1987
G. L. Hofman, Nucl. Technol., 77, (1987).

Hofman-1994
G. Hofman and J. Snelgrove, "Dispersion Fuels," in Material Science and Technology, 10A (1994).

Howell-1993
J. Howell, *Effect of Water Conductivity on Corrosion of Aluminum Alloys in Spent Fuel Storage*, Westinghouse Savannah River Company Report WSRC-MS-93-299 (1993).

Howell-1999
J. Howell, *Extended Wet Storage for Research and Test Reactor Spent Fuel for 2006 and Beyond*, Westinghouse Savannah River Company Report WSRC-MS-99-00602 (1999).

Katz-1951
J. J. Katz and E. Rabinowitch, <u>The Chemistry of Uranium, Part I: The Element, Its Binary and Related Compounds</u>, McGraw-Hill Book Company, New York (1951).

Reinke-1963
C. F. Reinke, *Irradiation and Postirradiation Annealing of Some Aluminum-Base Fuels*, Argonne National Laboratory Report, ANL-6665 (September 1963).

Samoilov-1968
A. G. Samoilov, A. I. Kashtanov, and V. S. Volkov, <u>Dispersion-Fuel Nuclear Reactor Elements</u>, translated from Russian, Israel Program for Scientific Translations, Jerusalem (1968).

Snelgrove-1987
J. L. Snelgrove, R. F. Domagala, G. L. Hofman, T.C. Weincek, G. L. Copeland, R. W. Hobbs, and R. L. Senn, *The Use of U_3Si_2 Dispersed in Aluminum in Plate-Type Fuel Elements for Research and Test Reactors*, Argonne National Laboratory Report ANL/RERTR/TM-11 (1987).

APPENDIX B

THE MELT-DILUTE PROCESS FOR ALUMINUM FUEL TREATMENT

The melt-dilute process has been approved for the treatment of aluminum-based fuels [Adams-1998, -1999; Vinson 2000]. As these fuels are generally $>20\%$ enriched in ^{235}U, the purpose of the melt-dilute process is to reduce criticality (reduce ^{235}U to <20% to achieve k_{eff} <0.95 for some configurations), produce better waste form characteristics, and potentially reduce volume. In short, the spent fuel assemblies are melted at <1000°C in a crucible (e.g., carbon steel or graphite) using an induction furnace, depleted uranium is added to lower the enrichment, aluminum is added if necessary, and neutron poisons are added. The mixture is furnace-cooled to produce ingots for storage. The target mixture is <20% U (a eutectic is located at 13.2 wt% of uranium) to obtain a low liquidus temperature for U-Si and UAl$_x$, of which most of the inventory is composed. These fuels will require a melt temperature of 646-850°C while oxide fuels may require higher temperatures. The U$_3$O$_8$ will require 850°C and additions of Ca (~5%) to make the reaction kinetics adequately rapid (<1 h mixing). Some small-scale engineering testing (off-gas, melt configuration, duration, additives) and microstructural investigations have begun on U-Al alloy, UAl$_x$, U-Si, and Al-U$_3$O$_8$ and also static and flow-through corrosion experiments under galvanic coupling, solution pH change, and varied electrochemical potential. Surrogate tests have investigated Cs, I, Se, Sr, Ce, Mo, Re, and Pd additions to the melt. Neutron absorbers are expected to be integrated into the melt to reduce criticality risk. Candidate neutron-absorber materials are Gd and Hf, added to <3%.

With regard to the experimental and theoretical discussion incorporated in this report, the melt-dilute configuration will introduce many important variables. The high melt temperature will induce restructuring of the fuel components and increase diffusion for all elements. An equilibrium melt with pure Al and U will precipitate UAl$_4$ in Al, exclusively. The effects of fission product and actinide disposition are unknown, although a finite amount of material will report to the aluminum solid solution and grain boundaries. If the fission products and actinides remain quantitatively dissolved in the uranium-aluminide grains, then one would expect the release rates for these elements to be lower than for unirradiated fuel. The reason, explained in the main text, centers on the thermodynamic stability of UAl$_4$ grains. However, introduction of depleted uranium and aluminum into the melt may affect this stability. In practice, it is difficult

to obtain an equilibrium melt under casting conditions [Hofman-1994]. A homogeneous melt will result in the precipitation of UAl_3 and possibly UAl_2 grains, essentially adding *unirradiated character* to the matrix. In this case, one might expect the fission products and actinides to redistribute into all the UAl_x grains (assuming that they report with the uranium).

In addition, the effect that absorber material will have on the corrosion and paragenesis is unknown—solid, dissolved, or colloidal.

REFERENCES

Adams-1998
T. M. Adams, H. B. Peacock, and N. C. Iyer, "Development of the Melt-Dilute Treatment Technology for Aluminum-Base DOE Spent Nuclear Fuel," Proceedings of the Am. Nucl. Soc. DOE Spent Nuclear Fuel Conf., Charleston, SC (September 1998).

Adams-1999
T. M. Adams, H. B. Peacock, F. C. Rhode, and N. C. Iyer, "The Melt-Dilute Treatment of Al-Base Highly Enriched DOE Spent Nuclear Fuels: Principles and Practices," Mat. Res. Soc. Symp. 556 (1999) 495–503.

Hofman-1994
G. L. Hofman and J. L. Snelgrove, "Dispersion Fuels," in <u>Materials Science and Technology – A Comprehensive Treatment</u>, Eds., R. W. Cahn, P. Haasen, and E. J. Kramer, 10A (1994).

Vinson-2000
D. W. Vinson, "Evaluation of Neutron Absorbers for the Melt-Dilute Treatment of Aluminum-Based Spent Fuel," Proceedings of the Embedded Topical Meeting on DOE Spent Nuclear Fuel and Fissile Material Management, San Diego, 276-283 (2000).

APPENDIX C

SCANNING ELECTRON MICROGRAPHS OF UNAUT1, UNAUT2, and UNAUT3

This section is a compilation of electron micrographs of the fuel meat surface, cladding, and transverse view of cladding-fuel meat interface. See the picture captions for specific information derived from the photos. The SEM/EDX systems were the Topcon/NORAN and Hitachi/NORAN Instruments housed in Chemical Technology Division laboratories. Backscatter images are shown, unless otherwise noted, and the uranium-containing solids appear white or white-gray. Aluminum and aluminum oxide appear as gray or black. The Topcon SEM used during the 31 and 67 day observations did not have adequate resolution at moderate magnification, so it was difficult to see tiny or subtle structures. The test number and analysis period are indicated in the subheadings of this section.

TEST UNAUT1 (FUEL PIECE 571A)

UNAUT1 after 31 Days of Testing
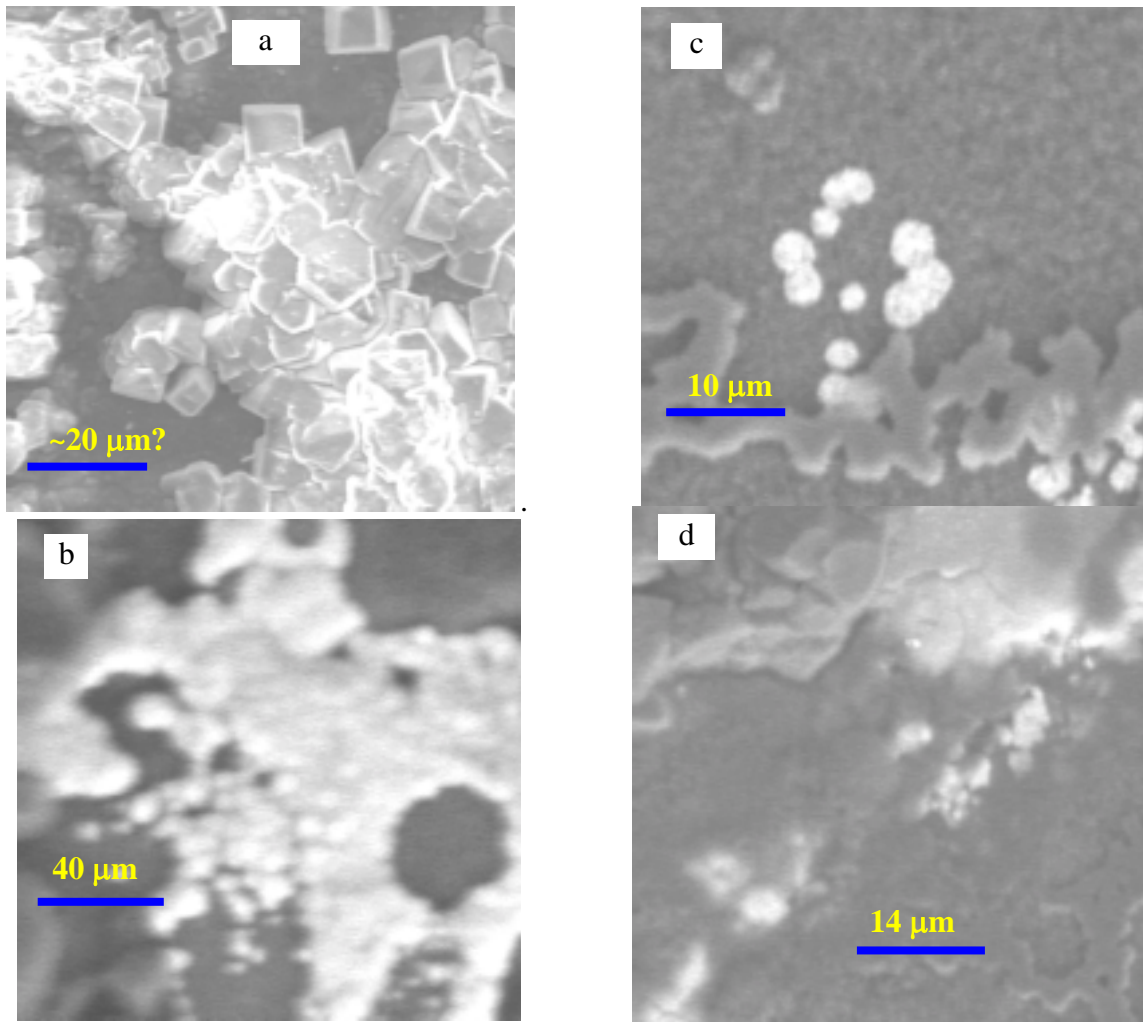
Fig. C1. a) Blocky crystals of hydrated aluminum oxide. b) Uranyl oxyhydroxide precipitate patches (bright) on the hydrated aluminum oxide layer. EDS spectrum shows U, Si, Al, and O. c) Some gold flakes (bright circles) were observed on the fuel face from the gold screen of the spent fuel holder, d) Regions enriched in uranium (bright regions).
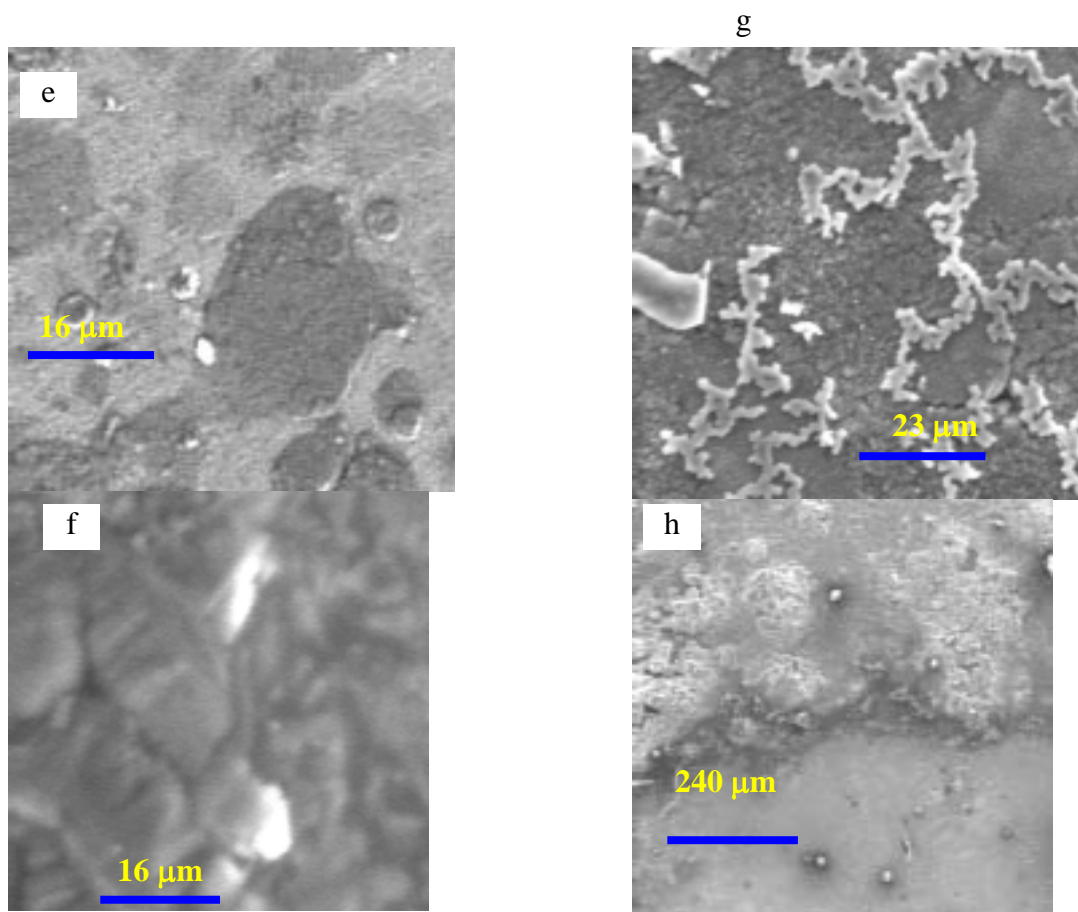
Fig. C1 (Contd.). e) Differing contrast shows general surface corrosion, f) Uranium particles (bright) appear out of the growing oxide surface, g) Precipitates strung together in a network atop the dark contrast of the hydrous aluminum oxide layer, h) This view shows the edge of the evaporation ring. At the bottom of the photo the drip apparently washed the surface smooth of precipitates. The dissolved components precipitated at the top of the photo.
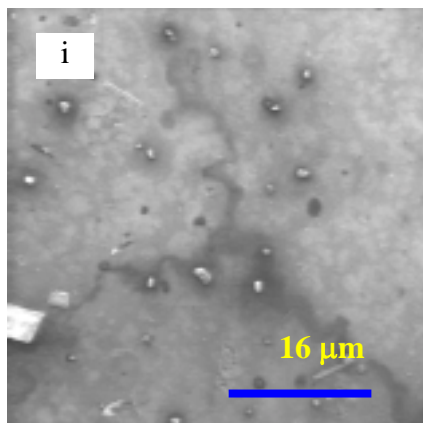
Fig. C1 (Contd.).   i) another view of the smooth hydrogel formed by the oxidation, dissolution, and precipitation of the silicon-containing aluminum hydrogel.

The following pictures were taken of the backside (C2) of the fuel piece (the cladding side) and the side view showing the cladding-fuel meat profile (C3).
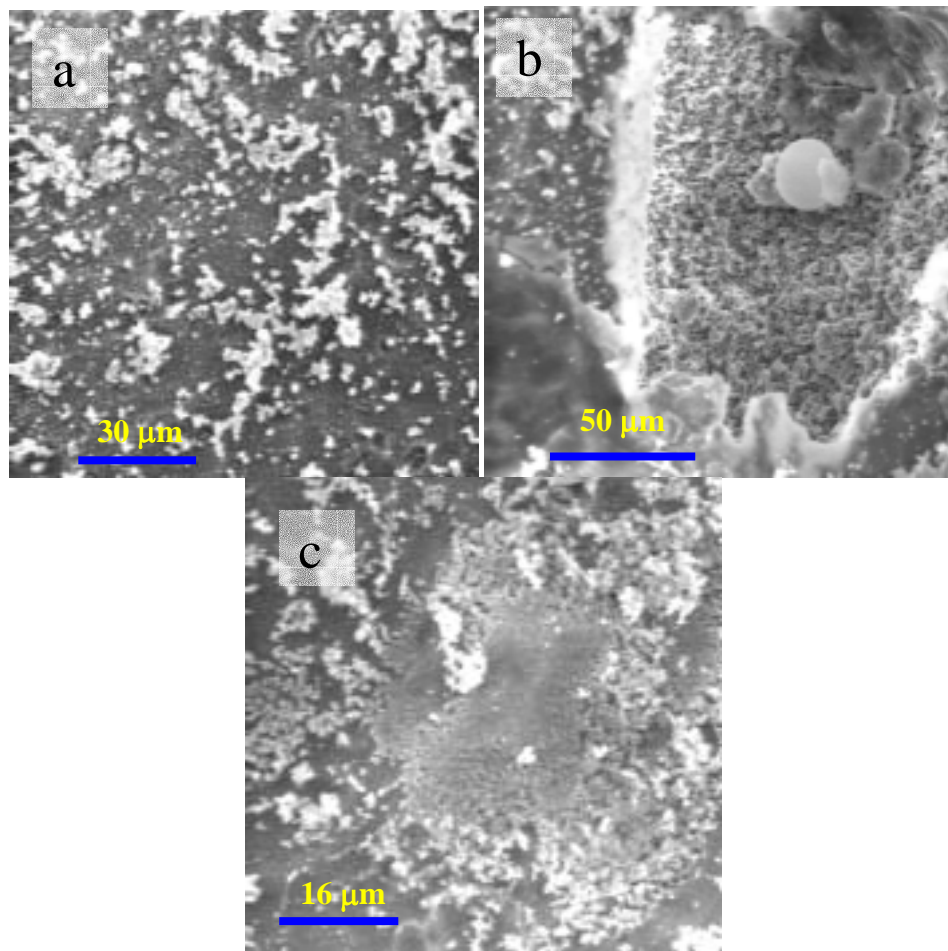
Fig. C2. a) A general picture of the cladding. This was typical of the piece where there were precipitates strewn across the aluminum. EDS shows that the precipitate has a copious amount of Si. The cladding surface contains Al, Mg, O, Si, and C with Si and O in less abundance than on the precipitate. A 120-μm wide pit in the cladding is shown in b) The refined grain structure is composed of a similar EDS spectrum as the cladding surface, i.e., Al with small peaks of Mg, O, and Si. c) Another view of the refined grain structure typical of gels.

The next set of images shows the secondary electron mode (left-hand side) and the complimentary backscatter mode (right-hand side). From this one can determine the surface morphology while capturing the location of any uranium (appearing white in the backscatter mode).

Secondary electron mode   Backscatter electron mode
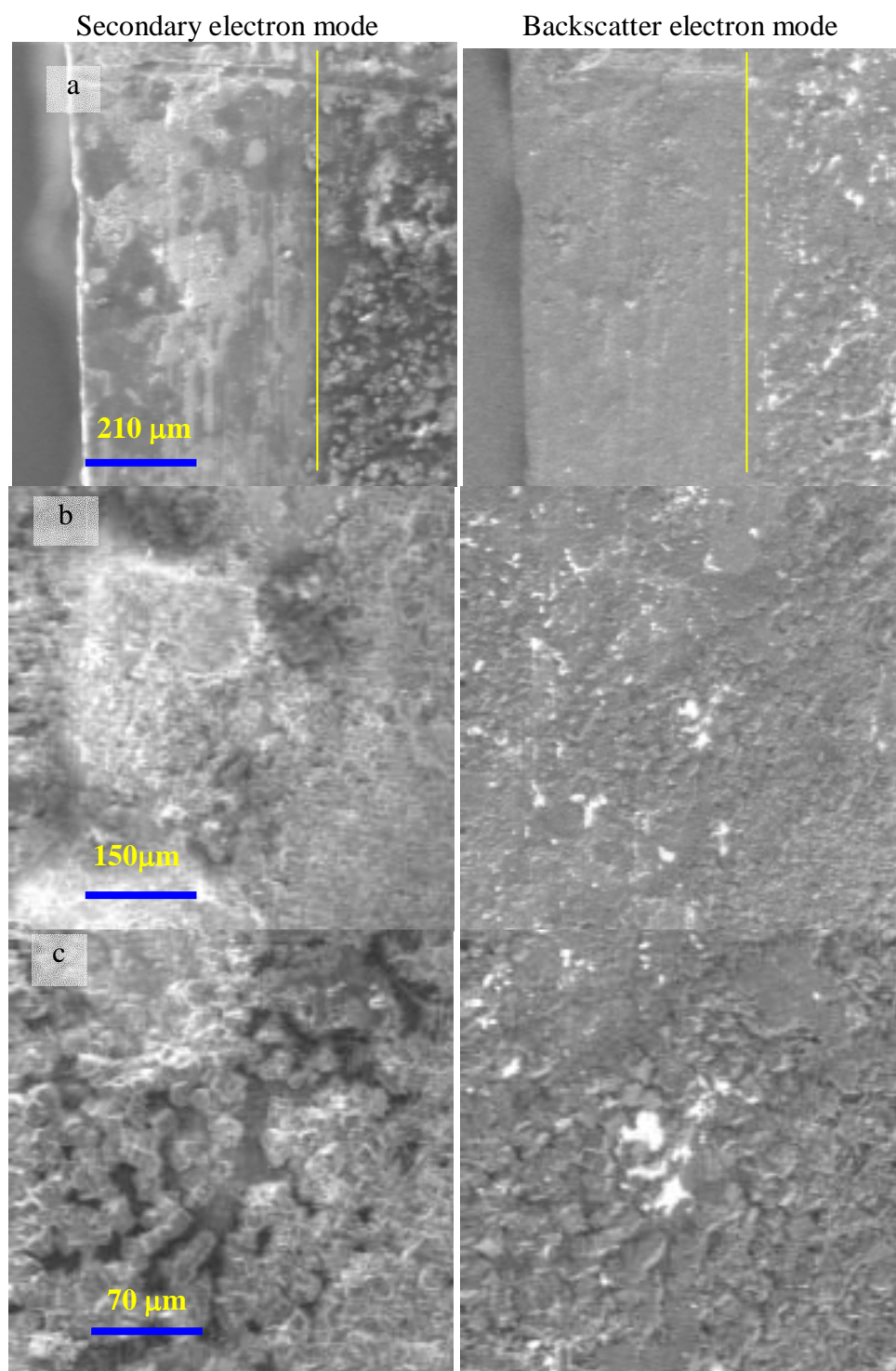
Fig. C3. Secondary and complimentary backscatter images of areas of the fuel. a) Shows cladding-fuel meat profile and edge of cladding. The line highlights the cladding side (left) from the fuel meat side. Note the hydrous Al-oxide growth has almost completely hid the underlying UAl_x. b) Wide view image of meat showing lack of visible U particles. c) Closer view showing U deposits embedded around the oxidized Al.

Secondary electron mode   Backscatter electron mode
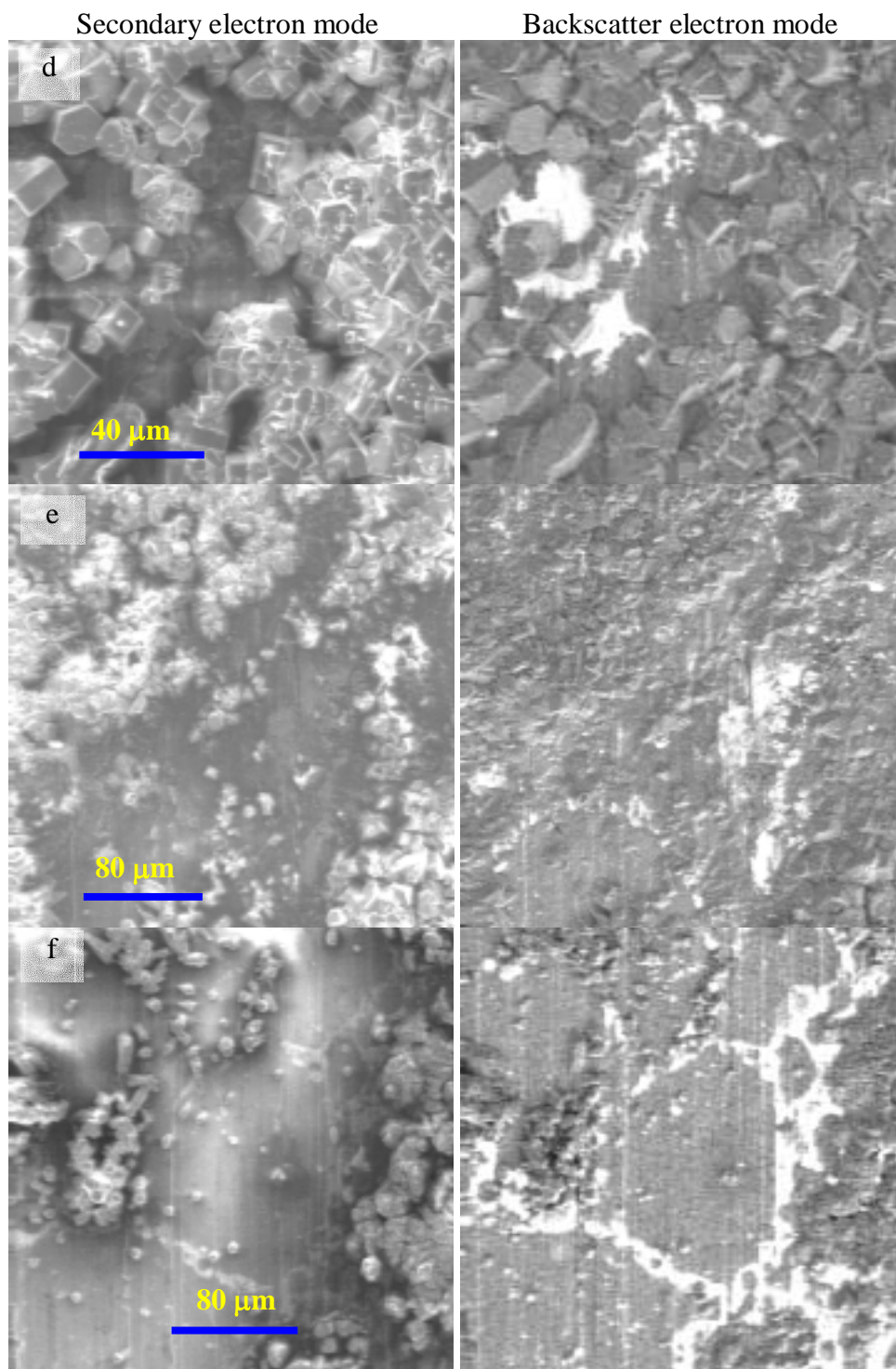
Fig. C3 (contd.).   d) Aluminum oxide corrosion blocks and uranium deposits. e) Again showing the difference in appearance of uranium from original fuel specimen. f) A photo showing what looks to be uranium seeping from around the grain of aluminum oxide. The "grain" size is 134 µm at its widest.

Secondary electron mode   Backscatter electron mode
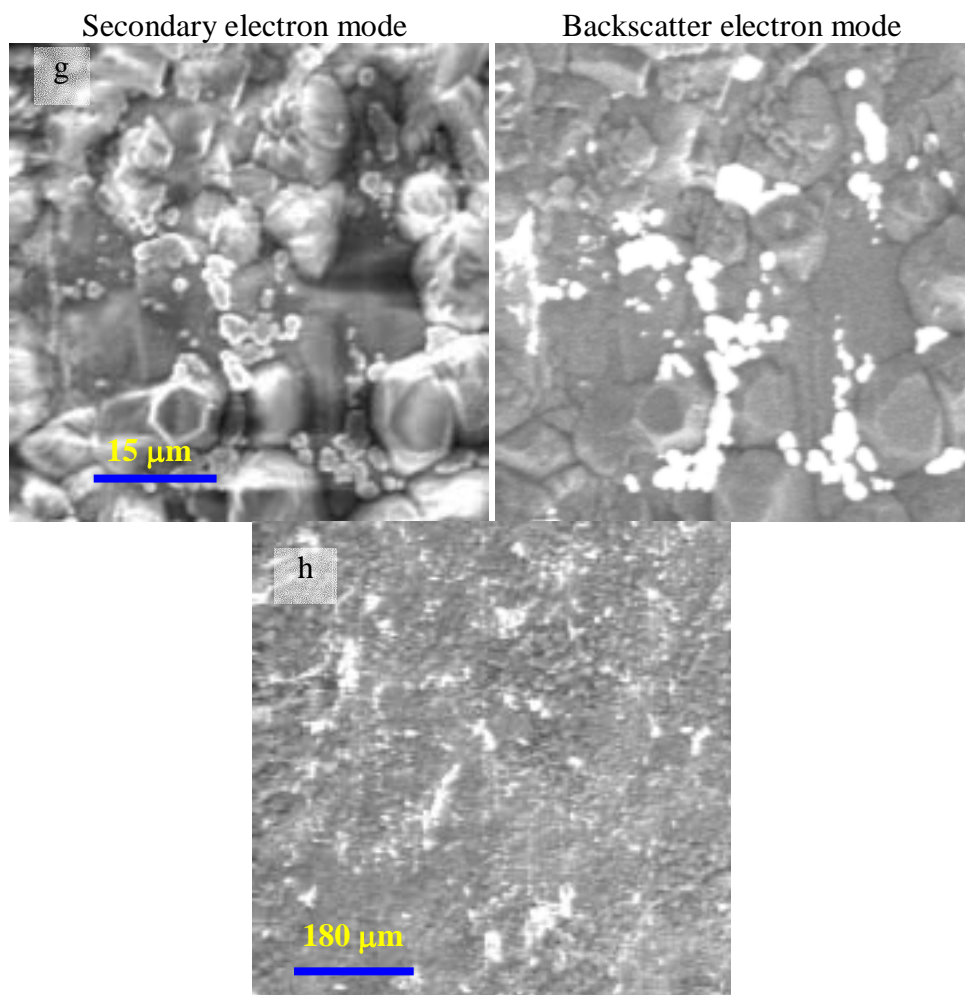
Fig. C3 (contd.).   g) Close up of uranyl-oxyhydroxide precipitates in a bed of aluminum oxide products. The uranium particles range from <1 µm to > 10µm. h) Wide field image of the fuel shows the lack of visible uranium (bright spots) in the corroded aluminum matrix. This is in stark contrast to appearance of fuel in the original specimen.
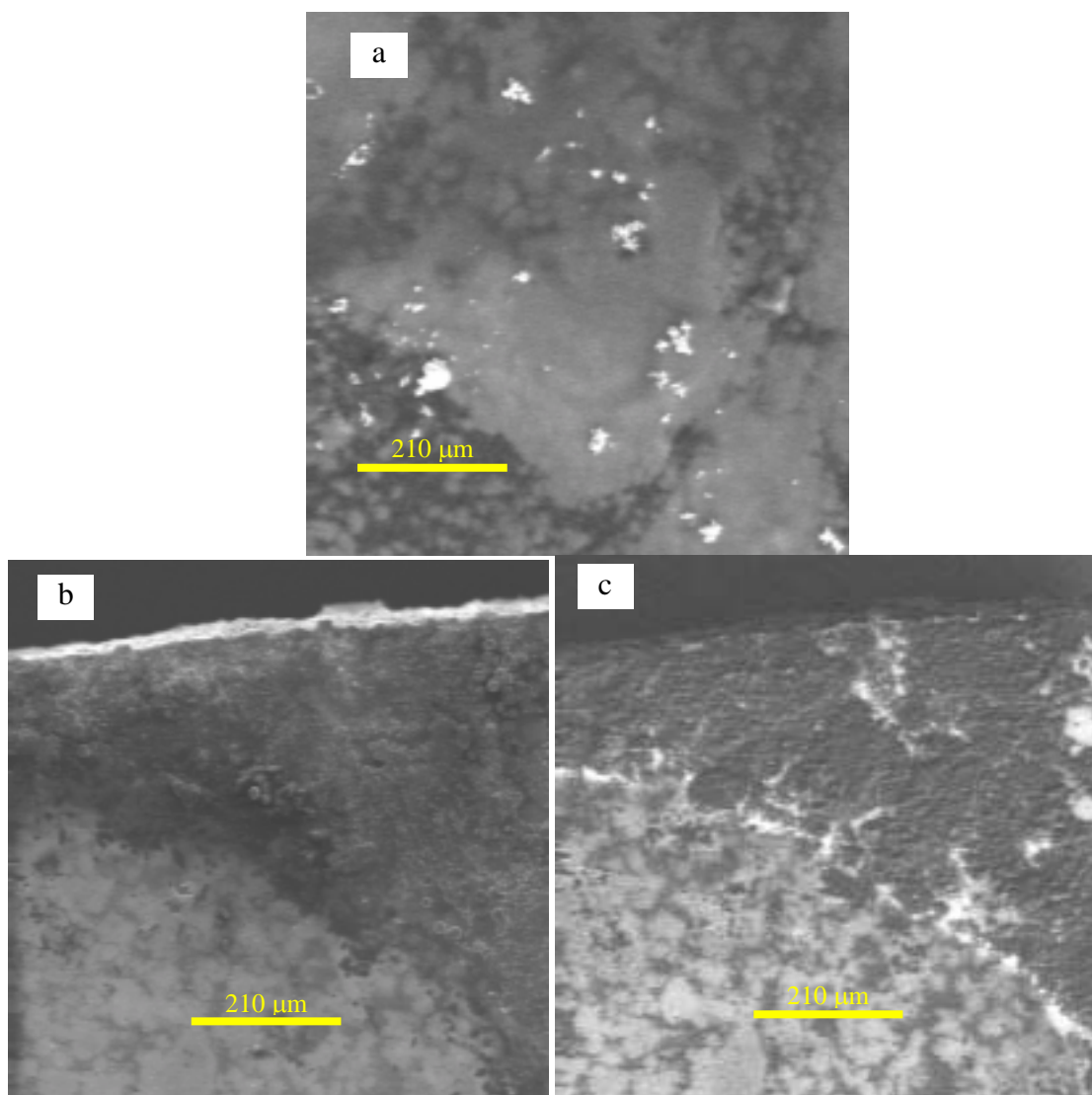
Fig. C4. a) Backscatter electron micrographs show clusters of gold from the grids of the spent fuel holder strewn across the UAl$_x$ surface. The specimen inadvertently flipped and was facing the gold mesh for an unknown number of days during this past test period. The gold clusters are composed of very fine (1 µm) particles. Secondary (b) and backscatter (c) image of the interface of the visible fuel meat surface and the abundant surface precipitates. The backscatter image highlights the UAl$_x$ grains (gray-white patches) in the aluminum (dark gray) and the aluminum oxide bed (dark gray). Note the brightest regions at the interface and in isolated patches within the aluminum oxide bed. The brightest regions are rich in uranium with no apparent aluminum.
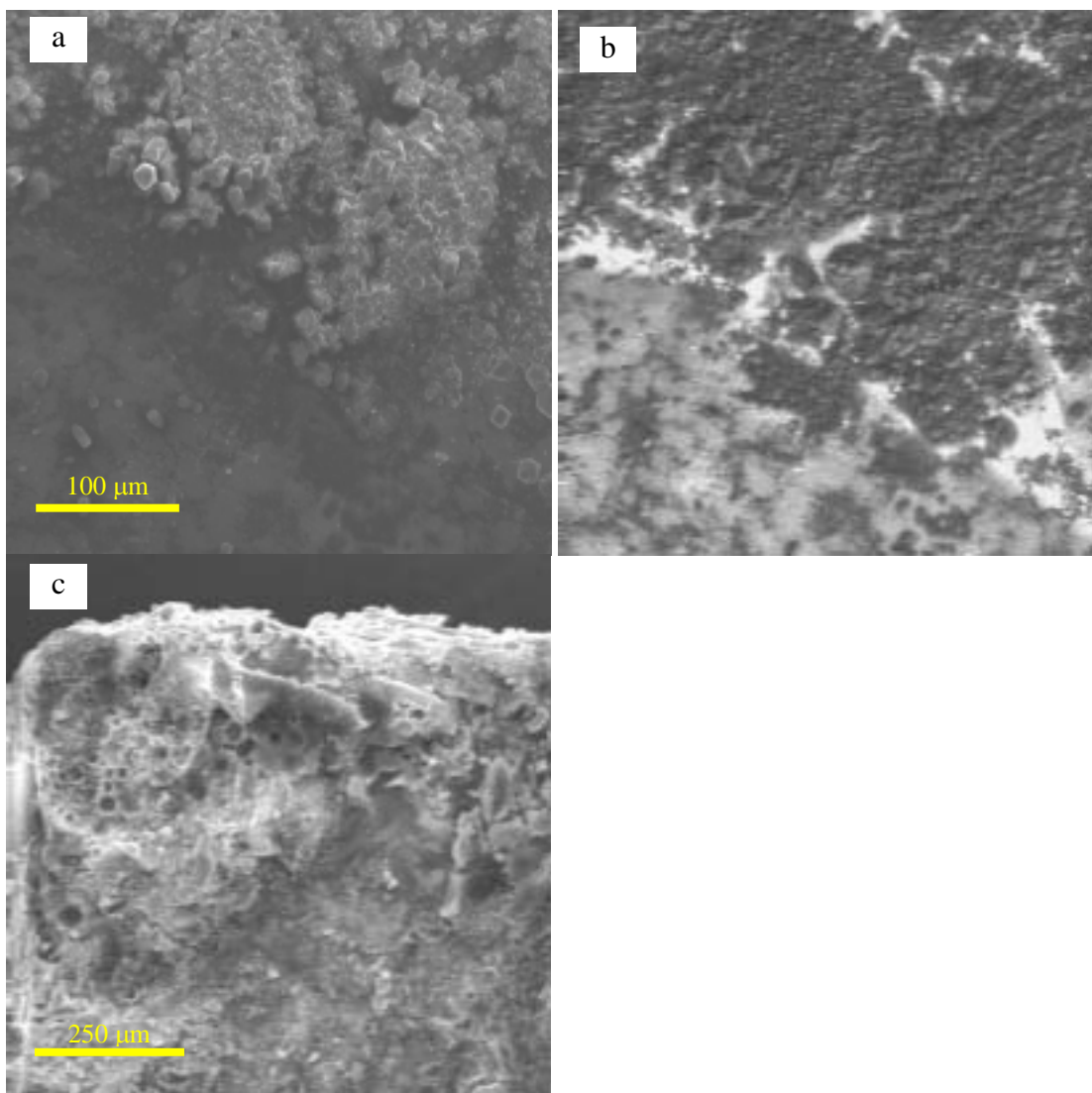
Fig. C5. A closer look at the area in C4 is provided here, in secondary (a) and backscatter mode (b). c) Precipitate on the corner of the fuel piece. The fuel was turned upside down and one corner apparently accumulated the moisture. This area is heavily laden with evaporites. A wide-area EDS scan showed the dominance of aluminum, with some silicon and oxygen. Calcium may also be present.
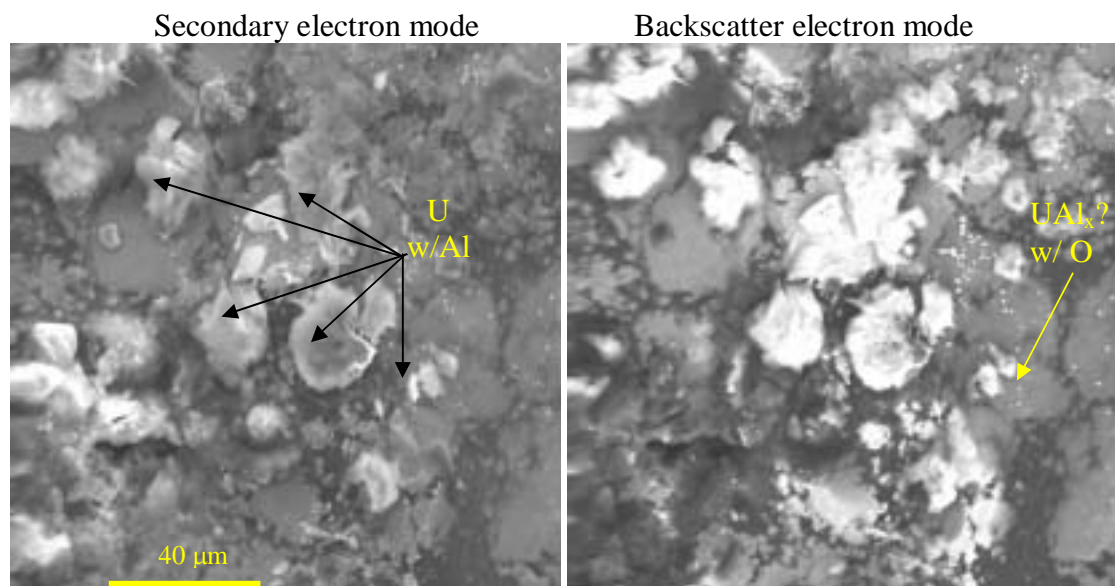
Fig. C6. A closer look at one of the gaps in the precipitate bed in secondary and backscatter electron mode, where the UAl$_x$ can be seen underneath. An abundance of uranium (oxides?) on the surface of the fuel meat is shown. Gold can be seen speckled across the surface. EDS of the bright uranium particles indicates the presence of Fe, Cr, and Al in addition to the strong presence of uranium.
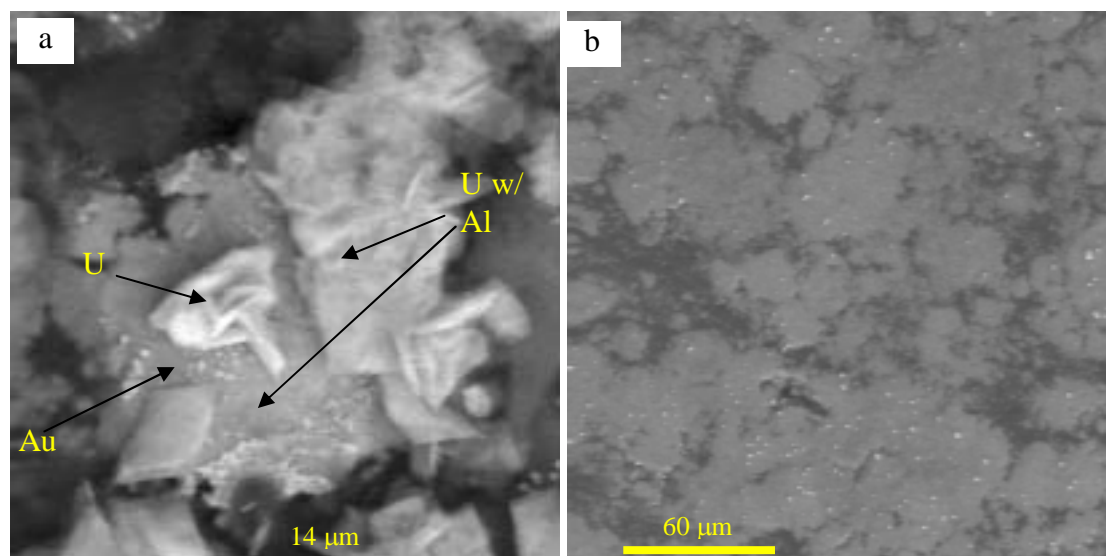
Fig. C7. a) A closer look at the uranium deposits shown in Fig. C6. The central bright mass is pure uranium (no oxygen detected). The less bright conglomerate to the right contains uranium and some aluminum with variable signal strength. It is certainly plausible that these masses represent uranium oxide with variable or no aluminum diffused within. Both of the aforementioned masses rest atop a similarly contrasted grain. This grain also is characterized by uranium with small amounts of aluminum. Again, tiny speckles of gold can be seen on the surface. b) The fuel meat surface. Here the fuel grains look completely intact. This area is part of the circular region of the fuel where it looked as though water had consistently fallen leaving the ring of evaporite surrounding this clear area. The hydrogel layer here appears to be passivating in nature. Speckles of gold are seen.
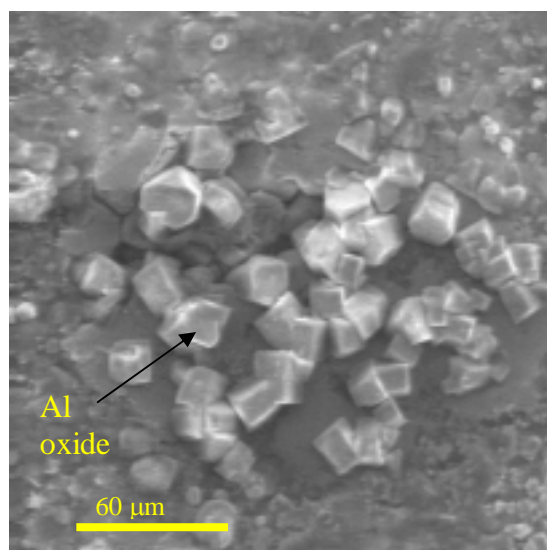
Fig. C8.   A transformation region of the fuel meat where
aluminum oxide blocks grow atop UAl$_x$ grains.

UNAUT1 after 115 Days of Testing
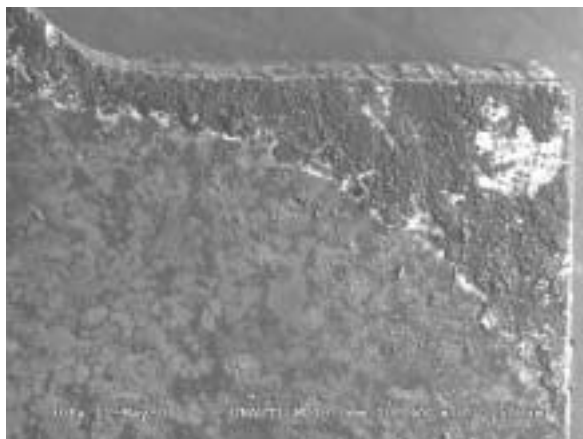
Fig. C9.   Top right corner of fuel piece. In general, the surface does not look much different than after the Day 30 sampling.

Fig. C11.   This is a closer look at that chain of diffuse uranium-rich material.

Fig. C10.   Taken from the area of the drip that covers almost the entire right half of the fuel face. Here we see a chain of uranium material that stretches from the top left of the picture to the middle bottom (the brighter white string). The mottled appearance on the fuel is due to growths from the fuel surface.
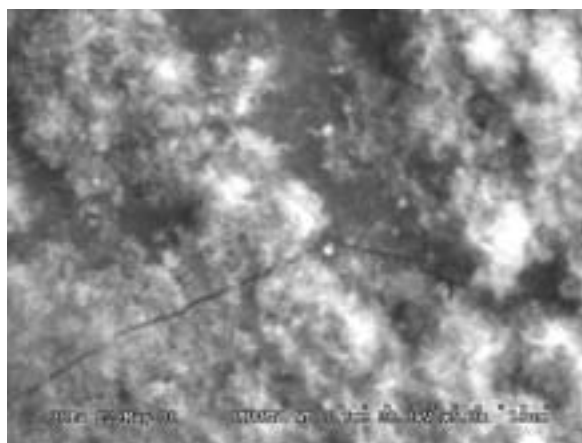
Fig. C12.   An even closer look shows the diffuse nature of these growths seen in C11. They look like clouds draped over the fuel surface. EDS suggests U enrichment but it is difficult to say for sure since the density of these growths is obviously very low. Perhaps, significant silicon enrichment and some detectable Na. A scan of the background gives evidence to this hypothesis.
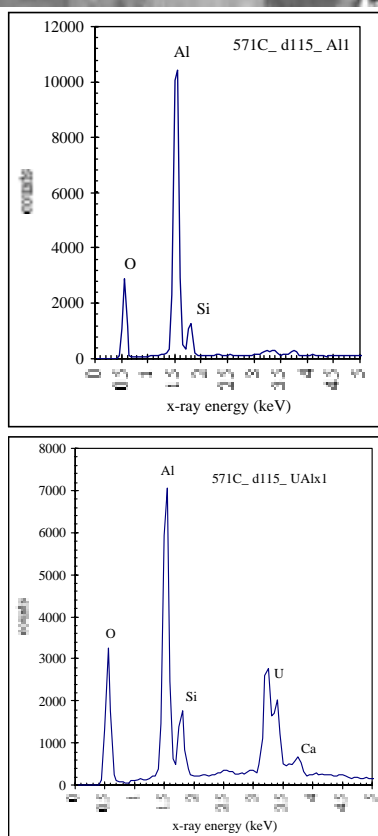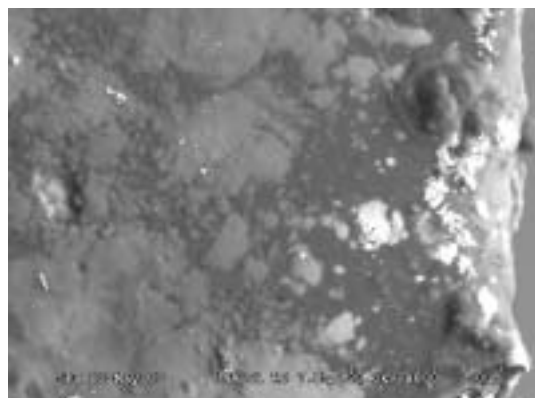
Fig. C13.   This is the right edge of the fuel. Note how the extreme right edge does not have a cloudy covering. The uranium regions appear bright and clear. To the left one can see the uranium regions progressively lose their clarity as they are submerged under a coating of aluminum oxide. EDS shows the aluminum region and typical spectrum of UAl$_x$ patch that is submerged under a hydrous aluminum oxide blanket.
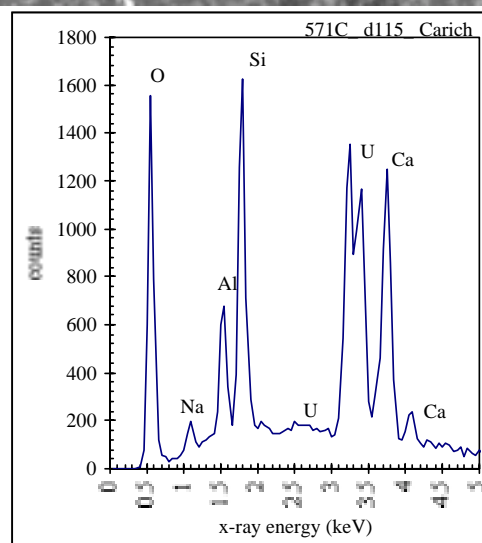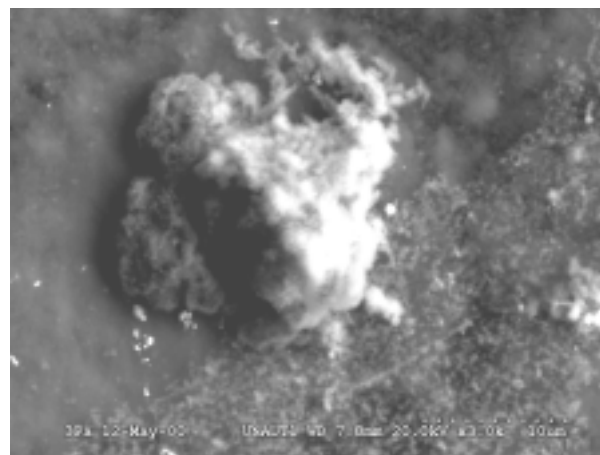
Fig. C14.   The fuel surface also contained calcium-silica rich precipitates. Also included is Na, and of course Al, O, and U.
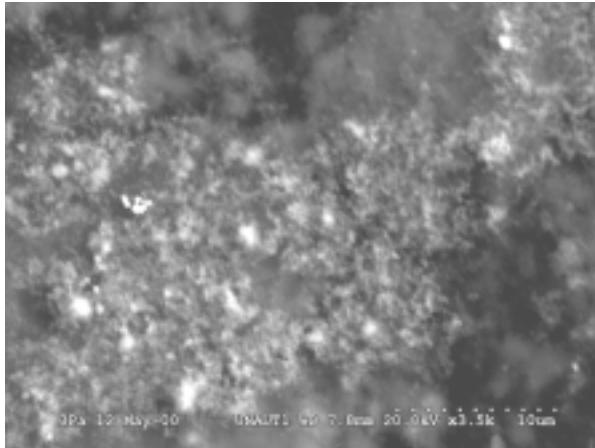
Fig. C15.   These wispy growths seem to be constrained to the UAl$_x$ regions.
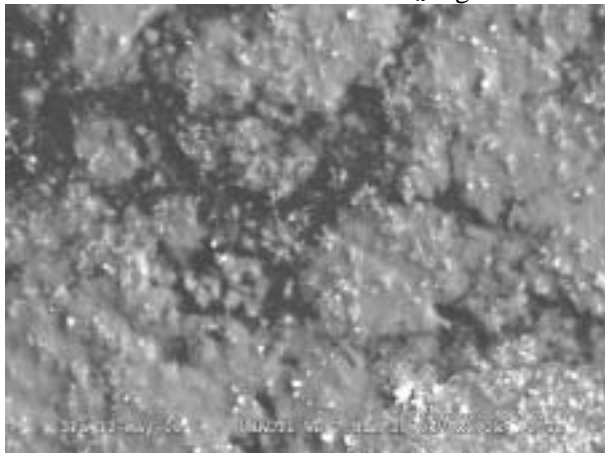
Fig. C16.   Another view of these growths.
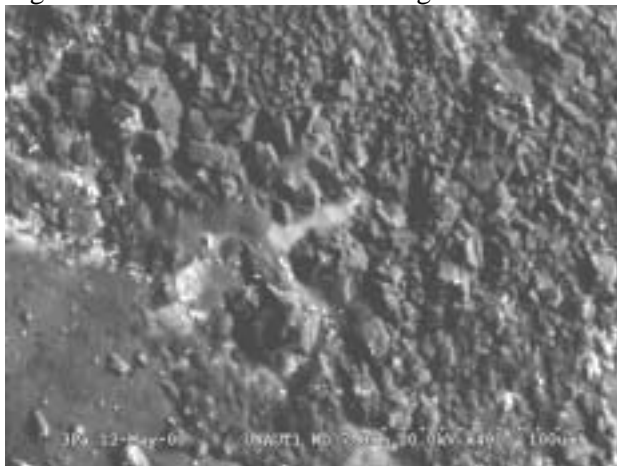
Fig. C17.   Top right corner of fuel. One can see the rubbled surface of aluminum oxide. At the bottom left one can see the flat surface where the suspected drips landed.
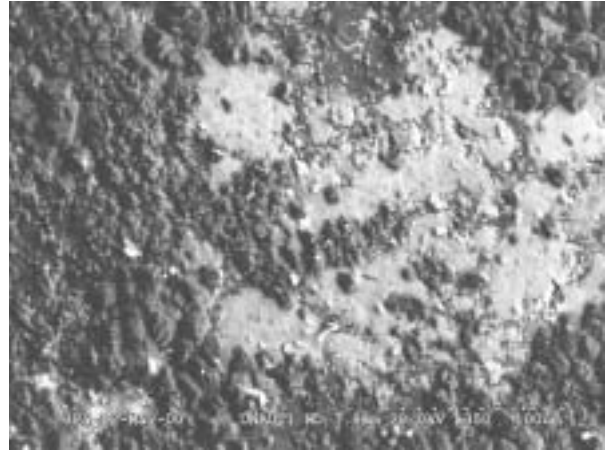
Fig. C18. Top right corner of fuel. Here is a region where there is a break in the aluminum oxide bed. Lying underneath is the UAl$_x$. There are a few bright growths atop the exposed UAl$_x$ surface. These were identified by EDS as U enriched with Ca, Si, and Al. Some Mg was detected in a few growths.
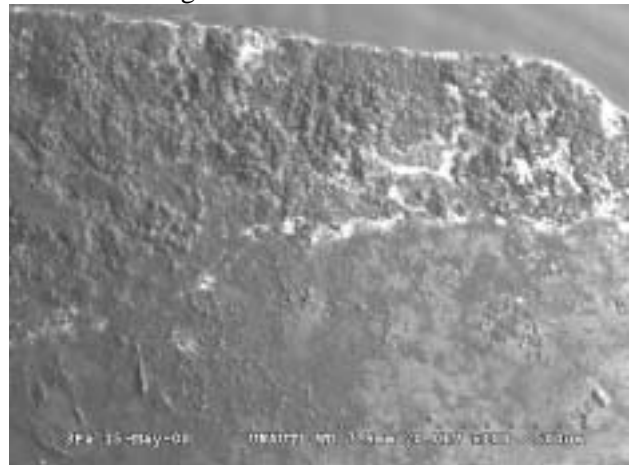
Fig. C19. Wide view of the top middle of the fuel piece.
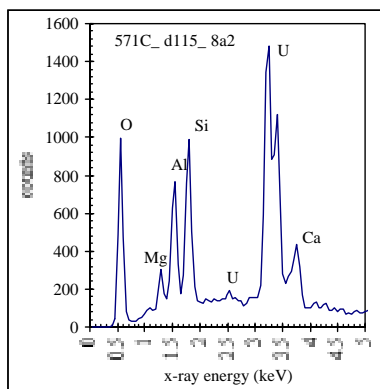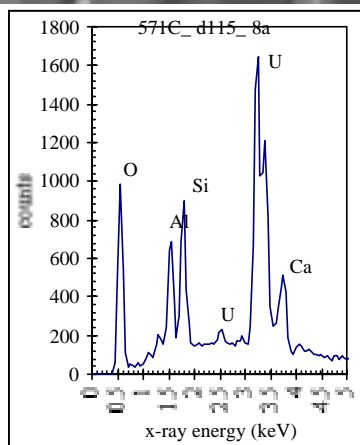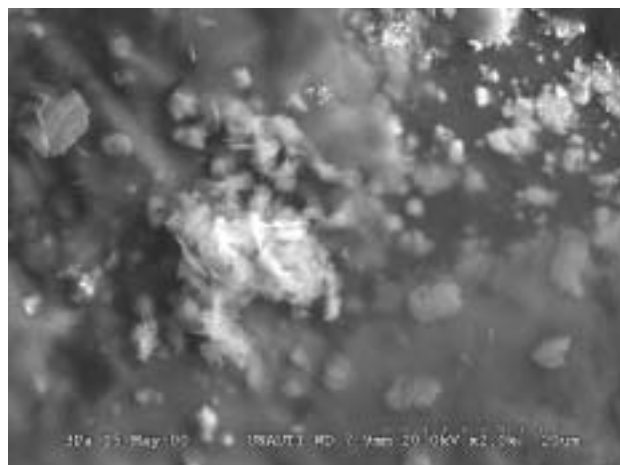
Fig. C20. EDS of the central bright conglomerate showed appreciable U enrichment along with strong Ca, Al, Si, and some Mg.
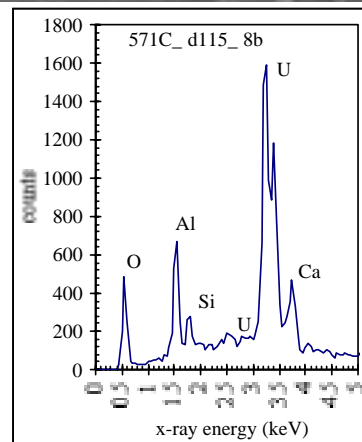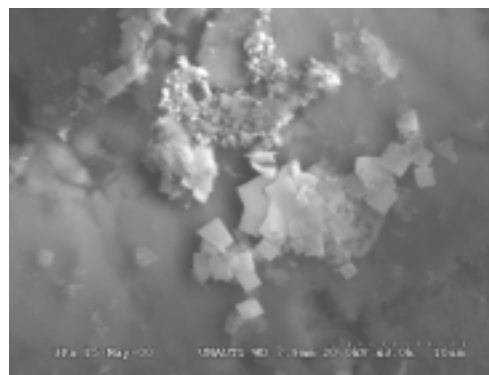
Fig. C21. The platelets that have been first seen during these tests. They are each about 2 m squares and very thin. EDS shows pattern similar to what we see with any U-enriched growth – Ca, Al, Si, and O.
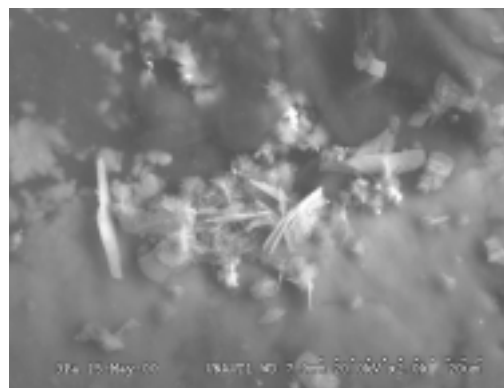
Fig. C22 This collection of growths revealed U enrichment, Al and Si (same peak heights), some Mg, and O. The real bright, very small spot just above the center of the photo, is a speck of gold.

Fig. C24.   These balls that grow atop Al oxide bed were identified by EDS to contain, besides Al, Si, and O, the elements Ca, Mg, and U.
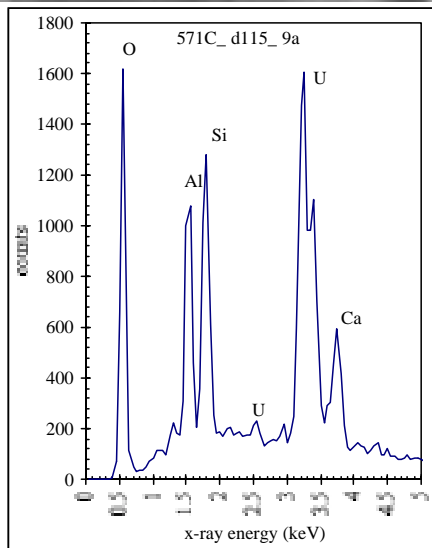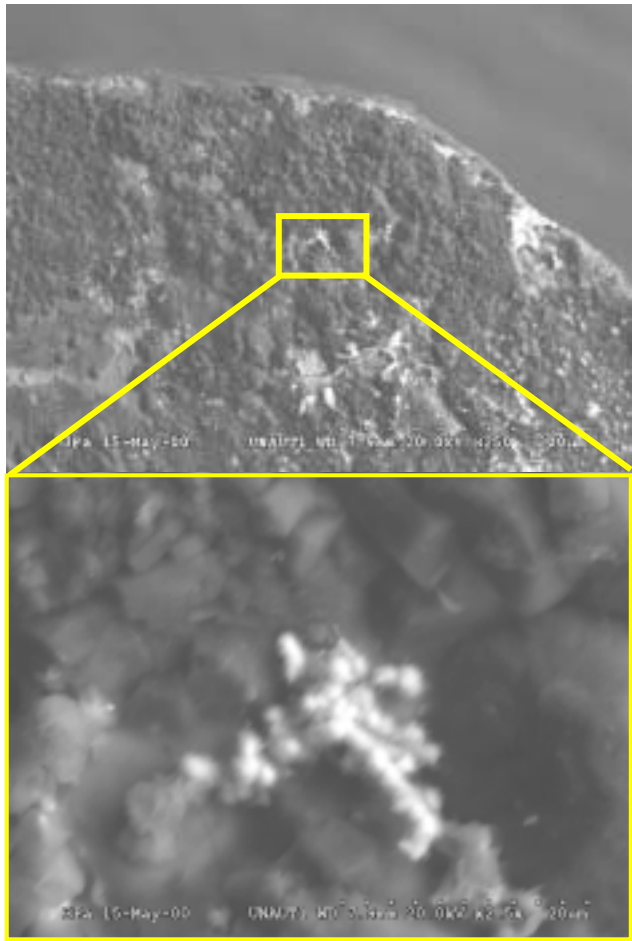
Fig. C23.   The thick precipitates in this area of the fuel contained some very small U-enriched growths. A closer view is shown. EDS is shown. Much O was detected.
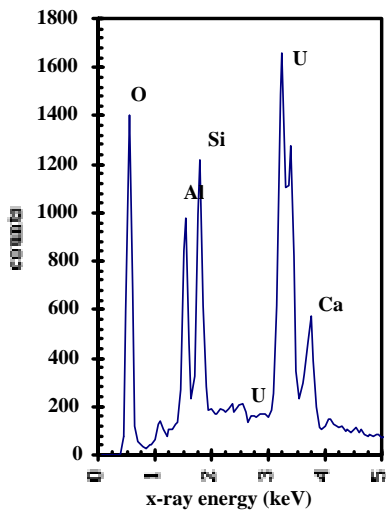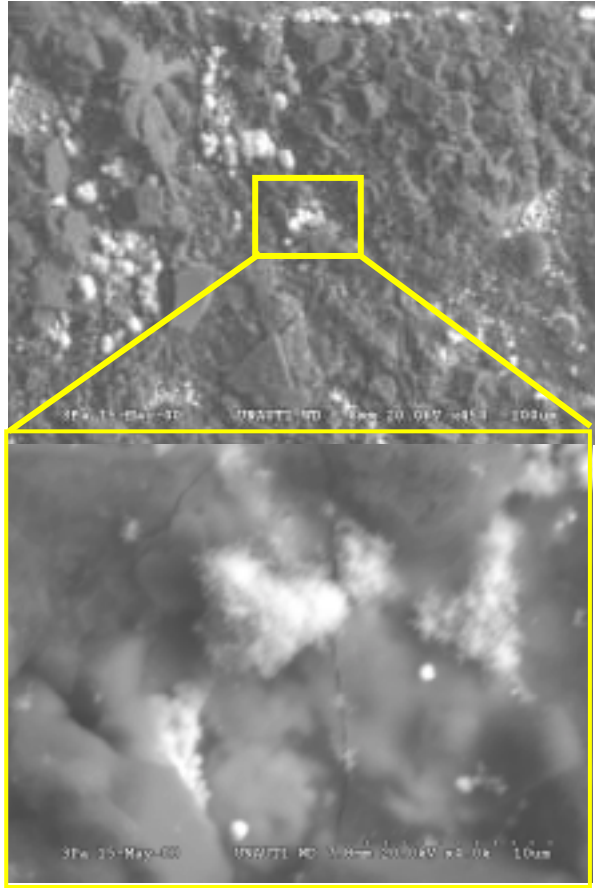
Fig. C25. Here is another look at the wispy U growths, a closer view, and x-ray spectrum.
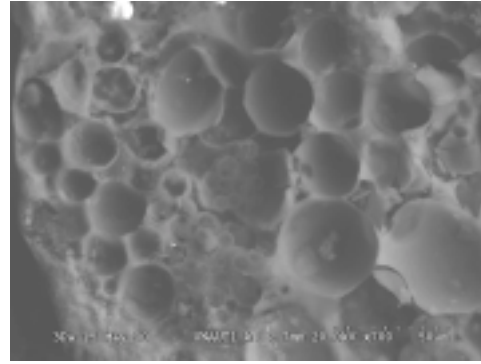
Fig. C26. This is taken from the left side of the fuel where the evaporated deposits are heaviest. These could be seen early on in the testing.

Fig. C27. Also in the left side of the fuel there are some large bright patches. They stand out because there is nothing but aluminum oxides on this side of the fuel except for these isolated patches. A view of the boxed area is shown in Fig. C28.
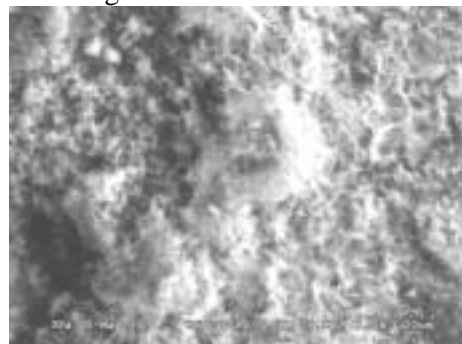
Fig. C28. A closer look at the patches seen in Fig. C27 shows that they are made up of a couple of different structures. Here we see a very expansive, thick patch of the U-rich material that appears in many other photos.

.
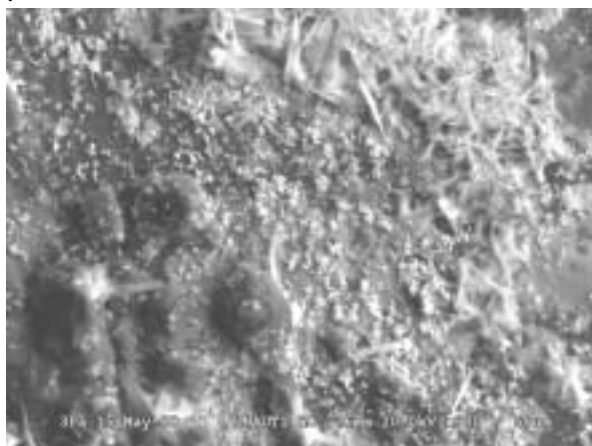
Fig. C29.   A look around reveals some other types of growths directly adjacent to the thick patches.
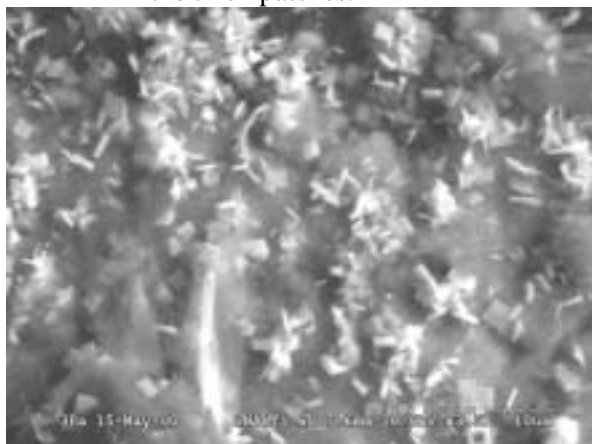
Fig. C30.   Upon closer inspection, we see that these growths are the familiar U-enriched wafers we have seen before. Now, though, we can see how they grow out of the surface of the fuel. Some of these wafers are half embedded in the surface.
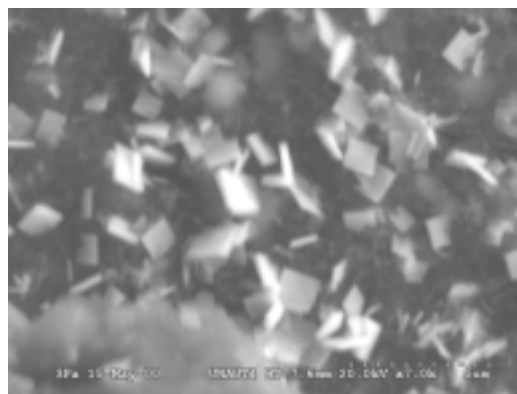
Fig. C31.   A closer look at the U-rich wafers. Same elements are seen by EDS as before – U, Al, Si, Ca, and O.

Fig. C32.   Here is another look at the thick U-rich patches. Below this one can be seen the wafers growing.
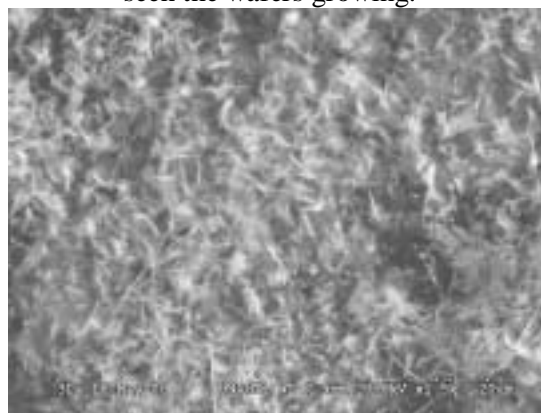
Fig. C33.   A view of another area nearby where a more sparse U-rich patch has precipitated.
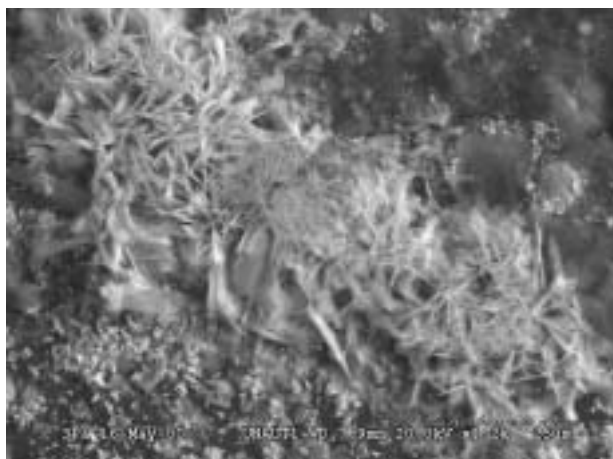
Fig. C34. This is basically the same image as in Fig. C32. Spot mode mapping shows that the individual plates comprising this patch are very enriched in U and Ca. The U peaks dominate the spectra (~700 cts for primary U compared to around 100 cts for Al and Si). The Ca peak is around 180 cts for comparison.
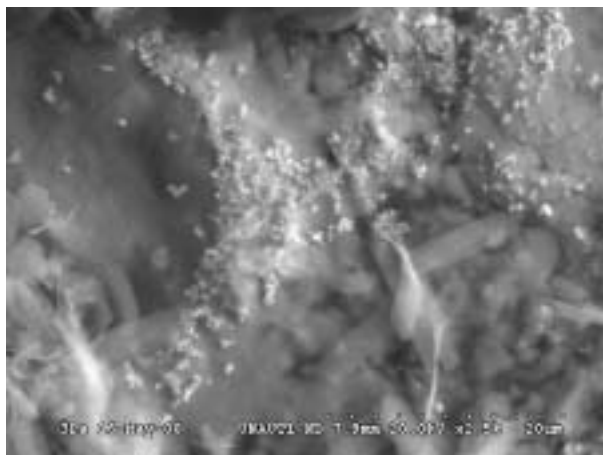
Fig. C35. Gold fines from the spent fuel holder.
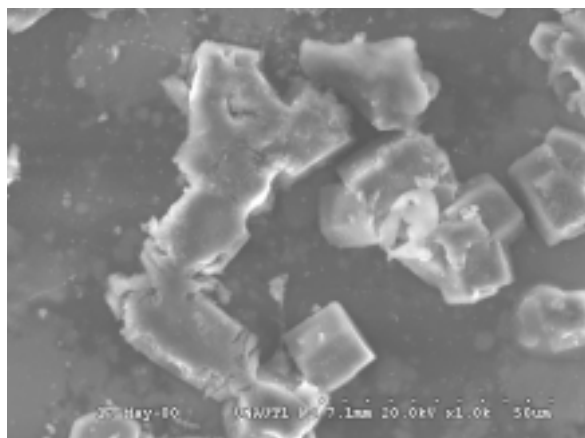
Fig. C36. Here is some Al, Si, O blocks.
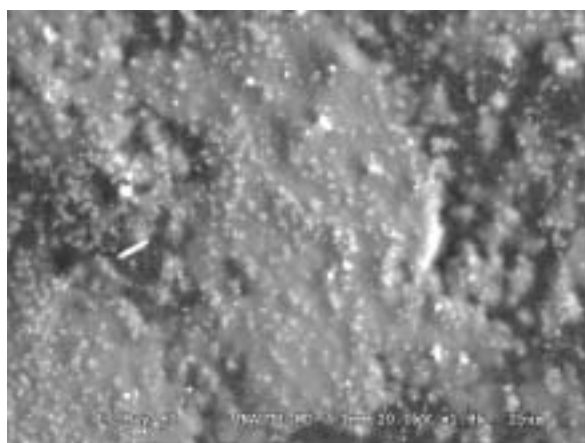
Fig. C37. Tiny nodules rich in U speckle the layer of aluminum oxides.
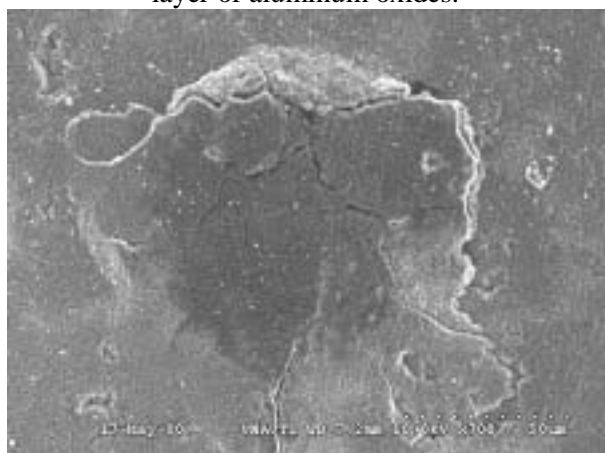
Fig. C38. Here is a surface image of the flat region where the drips landed. The surface is very smooth except in spots where the layer has upheaved and cracked.
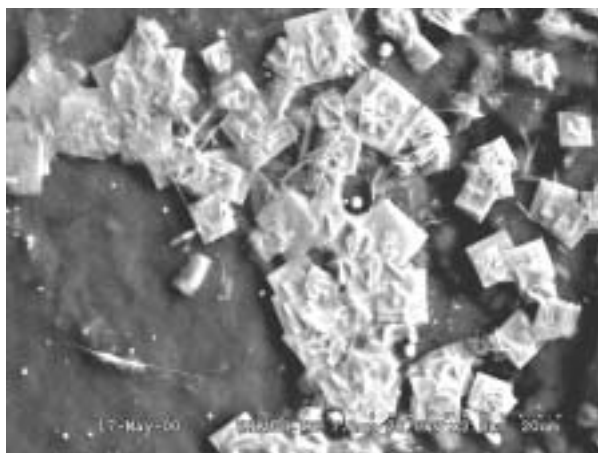
Fig. C39. Here is a thicker patch of the wafers. Some Si (not as intense), Al, O, Ca, and strong U signals detected. A background scan below the wafers shows a typical UAl_x altered spectrum. Thus, these are growing atop a UAl_x (or at least altered UAl_x) grain.

Fig. C41. Balls of uranium-enriched growths on the side of the coupon.
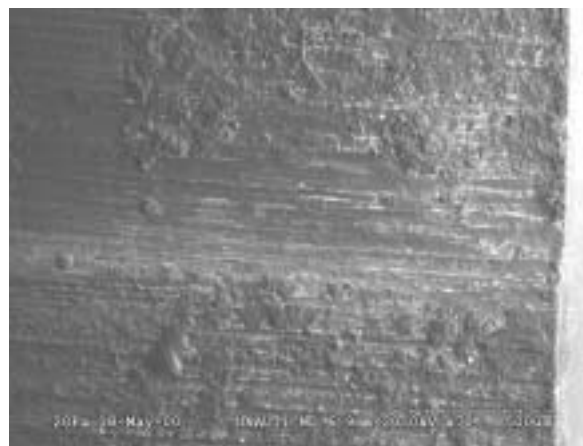
Fig. C42. Transverse view shows the overgrowth of Al oxide such that it is difficult to see any uranium (white lines). This part of the fuel piece is similar in morphology to parts of the fuel face that was covered in evaporites. It is likely that the standing water on the fuel face offers an environment by which the Al can dissolve and synerize into a hydrogel. Thus, most of the fuel face was covered in this hydrogel. Water is not as static on the sides of the coupon and in some parts of the coupon. Thus, these areas "dry" sufficiently to form amorphous boehmite.

Fig. C40. Tipped to its side, a view of the cladding/fuel meat is shown. Where the fuel meat could be easily distinguished at test start, the bright patches of uranium can only be seen in streaks across the sample.

UNAUT1 after 183 Days of Testing (Test Terminated)
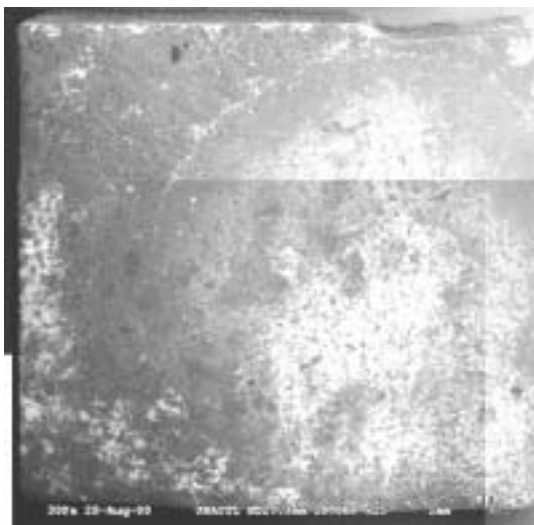
Fig. C43. Composite of the fuel surface. Note the circular outline of the evaporite ring. Patches of uranyl-oxyhydroxide precipitates can be seen at the left edge of the fuel and running along the bottom edge. The large bright areas in the center of the picture were captured at very high contrast to highlight the altered UAl_x grains below the Al-silicate hydrogel. The hydrogel is characteristically smooth as opposed to the precipitates found surrounding the smooth gel. See UNAUT2 day 67 pictures to contrast the surface appearance.

Fig. C45. A closer look at the Al-silicate precipitates that surrounded the smooth Al-silicate hydrogel.
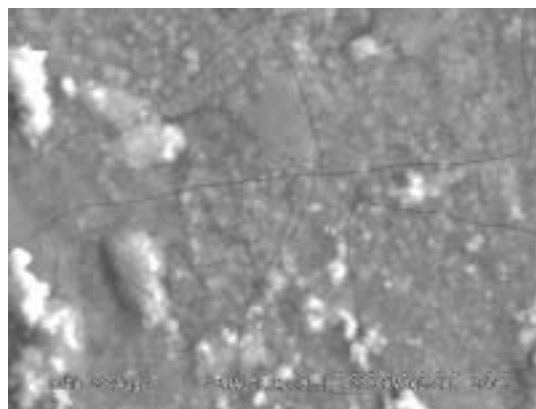
Fig. C46. The smooth gel region shows signs of cracking due to ambient drying.

Fig. C44. The smooth gel layer is shown at the bottom left. The gel precipitates corner the gel region in this picture.
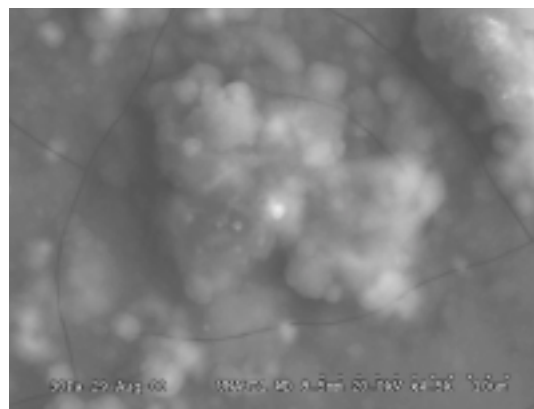
Fig. C47. A small nodule of precipitated uranyl-compound embedded in the gel. Note the cracks on the gel surface.
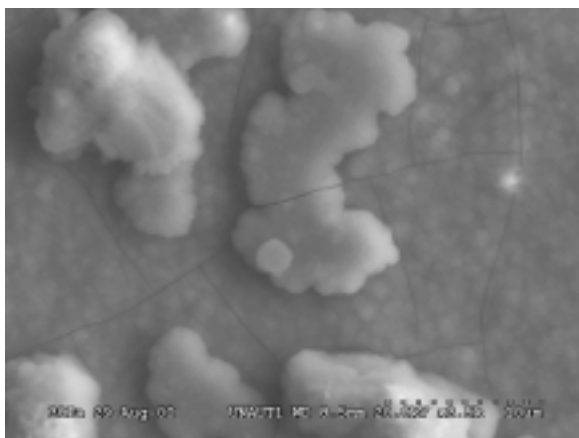
Fig. C48. Some precipitates formed from the gel.
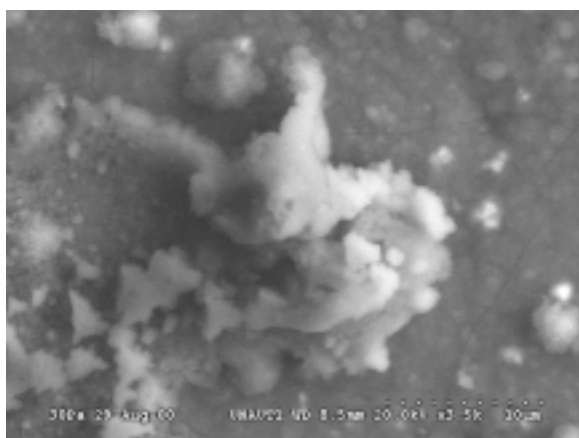
Fig. C49. Some U-rich precipitates forming in the gel.
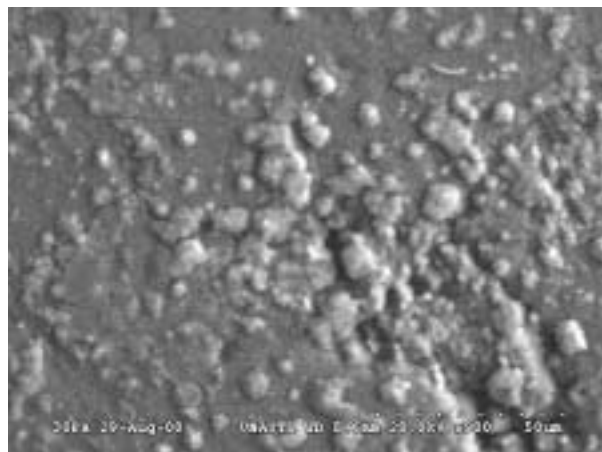
Fig. C50. More precipitates.
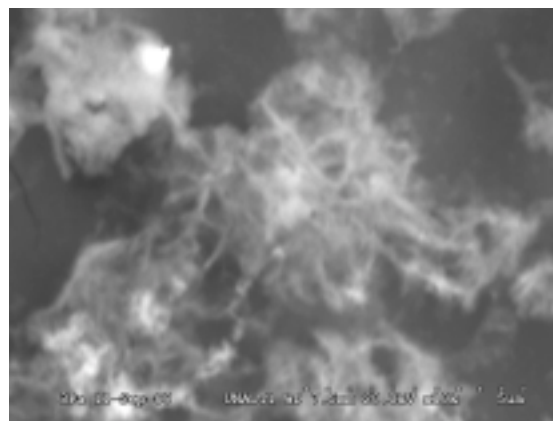
Fig. C51. A close look at U oxides coagulating. These spider-like structures may be precursors to the plate structures typical of the uranyl oxyhydroxides.
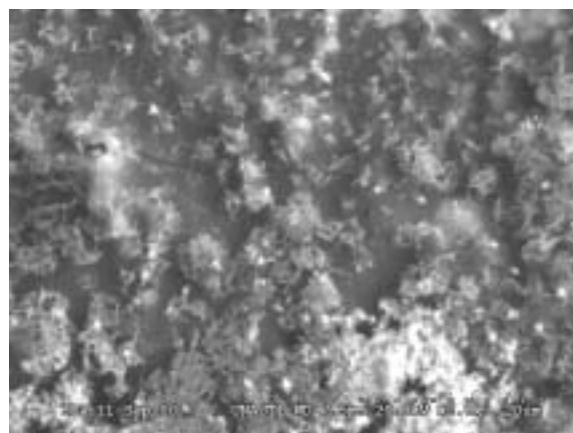
Fig. C52. The area shows an abundance of structures as in Fig. C51.

Fig. C53. This is a closer look at the uranyl-oxyhydroxide patch at the left side of the fuel in Fig. C43.
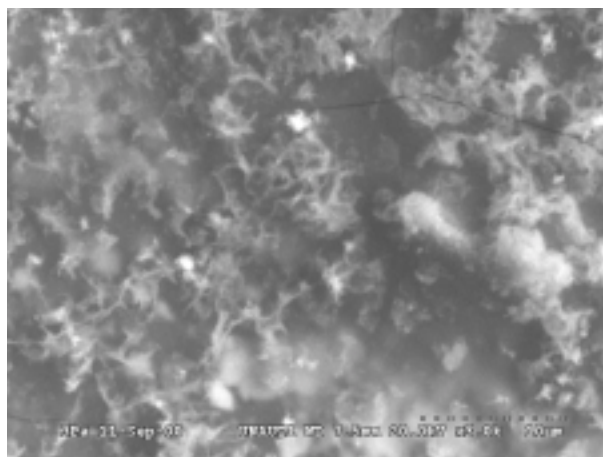
Fig. C54. More precipitates forming in the gel.
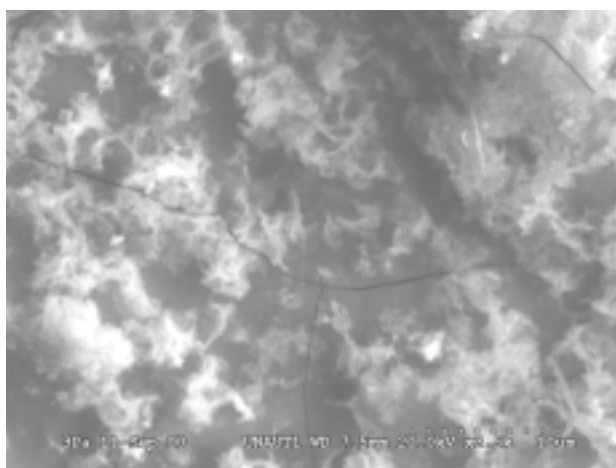
Fig. C55. A closer look at the precipitates in Fig. C54.

Fig. C56. This part of the fuel is slightly below that shown in Fig. C53. The two dark spots near the top of the fuel are the same as the two dark spots in the center of the picture in Fig. C43.
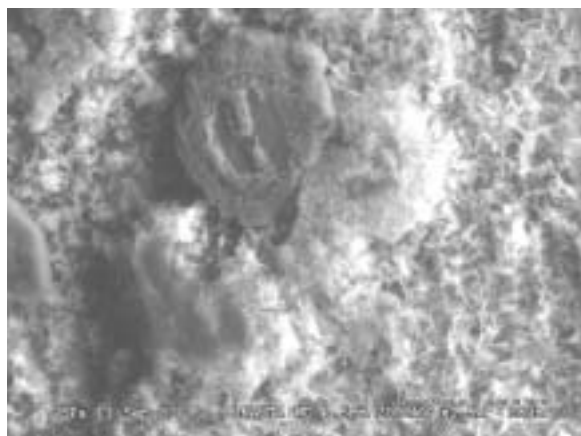
Fig. C57. Uranyl-oxyhydroxide platelets are crystallizing in this area of the fuel (closer view of regions shown in Fig. C56).
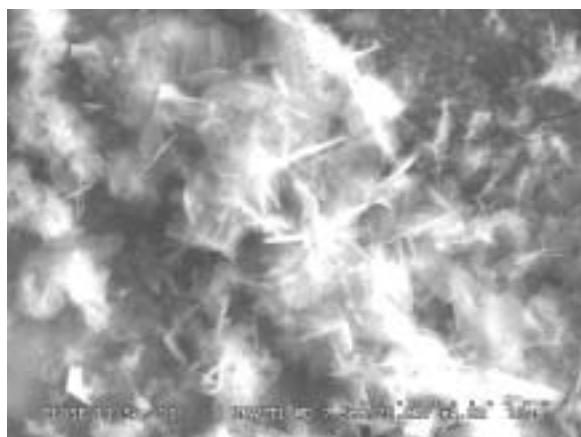
Fig. C58. Still another view of the U-rich precipitates.
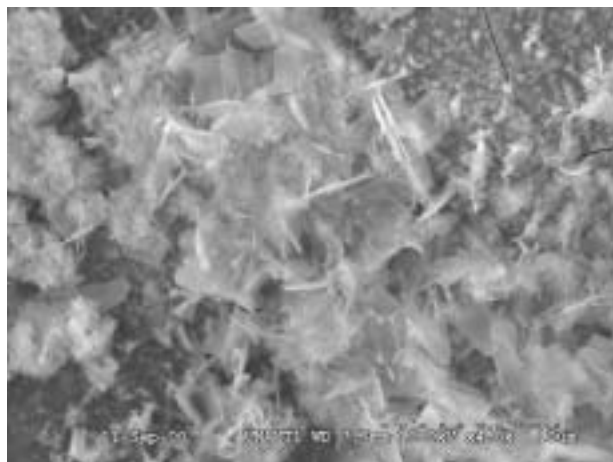
Fig. C59. Same view as in Fig. C58 except in secondary electron mode.
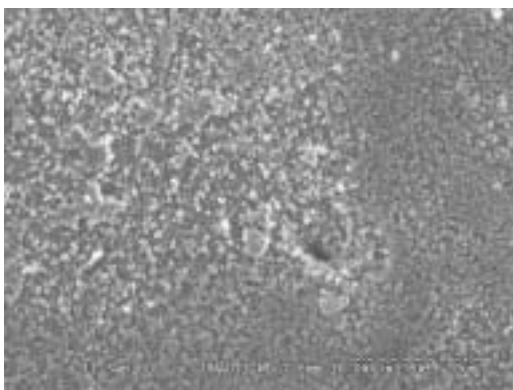
Fig. C60.   Uranium dissolved within the gel layer coagulating to form nodules. These will later form the platelets seen in previous figures or be partially washed from the fuel surface.
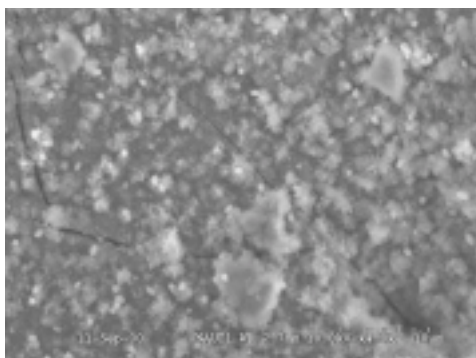
Fig. C61.   A closer view of Fig. C60 shows the tiny nodules of uranium coagulating within the gel.
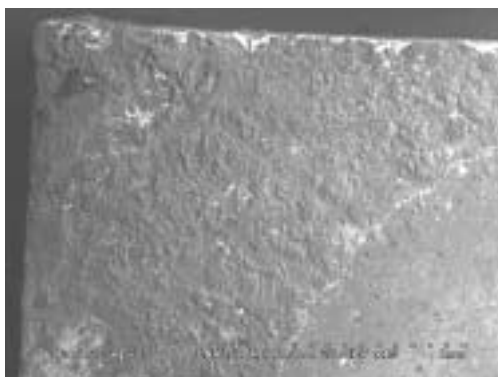
Fig. C62. Figs. C62-64 show a closer view of the left side of the fuel moving from top to bottom. In Fig. C62, some U-rich spots (bright white) can be seen at the top edge of the fuel and as a few speckles in the precipitated gel. The top end of the U-rich patches can be seen at the bottom left of this photo.
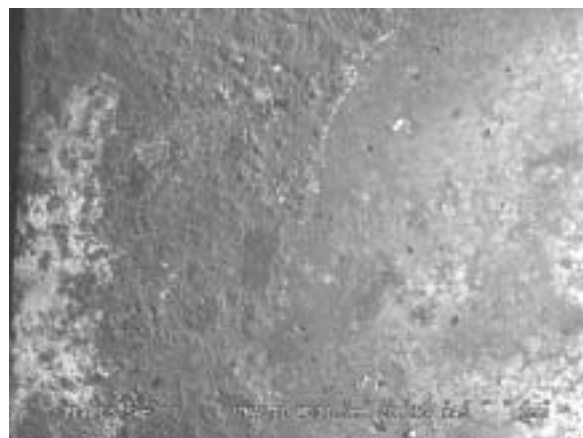
Fig. C63.   The middle of the left-hand side of the fuel contains a large U-rich patch (at left, bright white) that extends almost the entire field of view. The UAl_x patchwork can be discerned from underneath the Al-silicate hydrogel in the right-hand side of the photo.
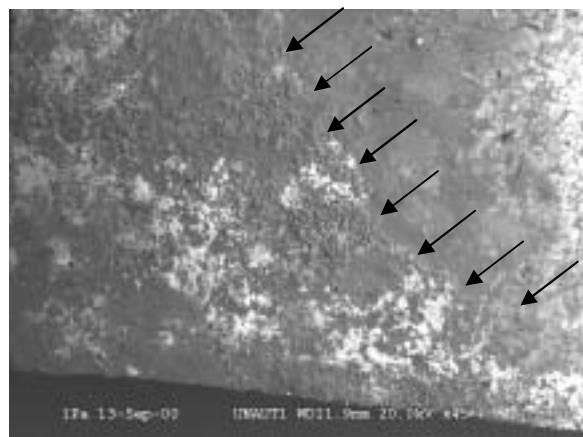
Fig. C64.   The view of the bottom left of the fuel face shows another, more discontinuous string of uranyl-oxyhydroxide precipitates formed in the Al-silicate precipitates. The border between the Al-silicate gel and precipitates is shown with the arrows.
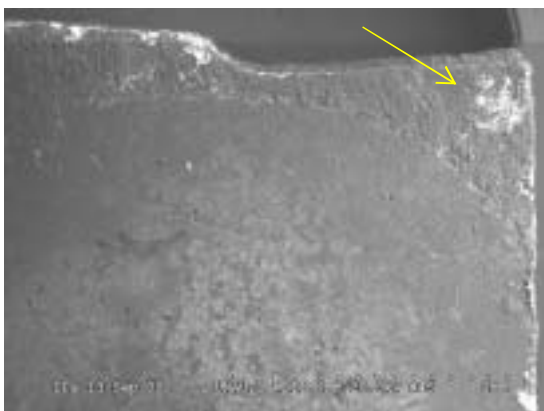
Fig. C65. The top right of the fuel face is mostly occupied by the smooth gel. At the top right of the photo a patch of uranyl oxyhydroxide is shown (also at the top, center and bottom, right.)

Fig. C66. Moving further down the fuel piece from Fig. C65, the UAl$_x$ patchwork can be seen through the gel layer. The arrow highlights a string of U-rich nodules (see Fig. C71).
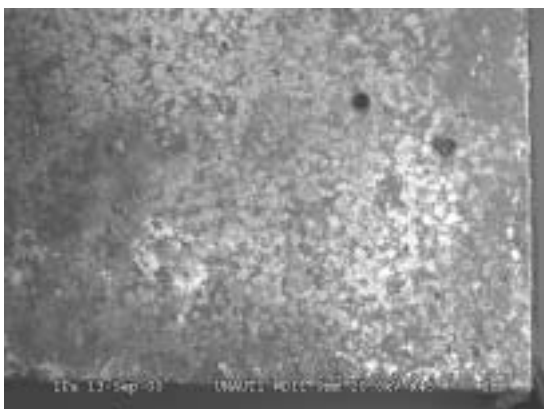
Fig. C67. As in Fig. C66, the smooth region occupies the bottom, right region of the fuel.
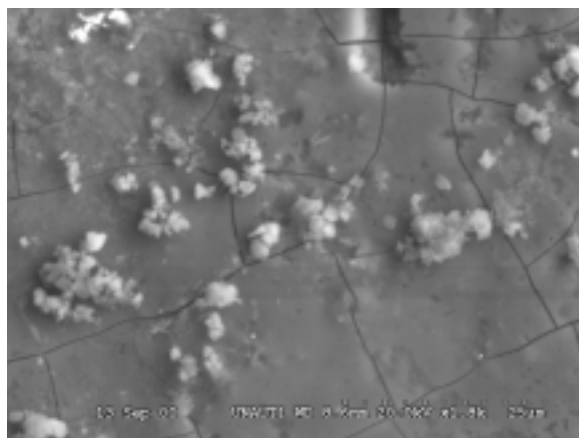
Fig. C68. Close-up view of the gel drying and forming cracks.
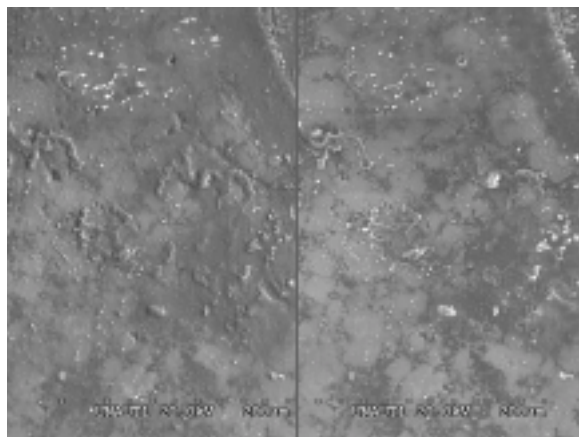
Fig. C69. Backscatter (left) and secondary (right) detection mode of the same region of the fuel.
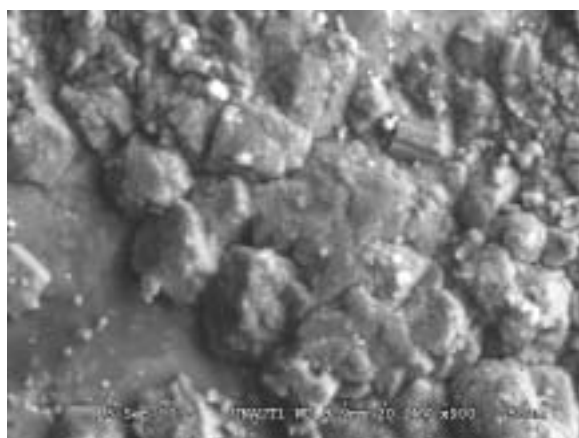
Fig. C70. This is a view of the top, right of the fuel face at the boundary of the smooth gel (bottom, left in this view) and precipitate regions.
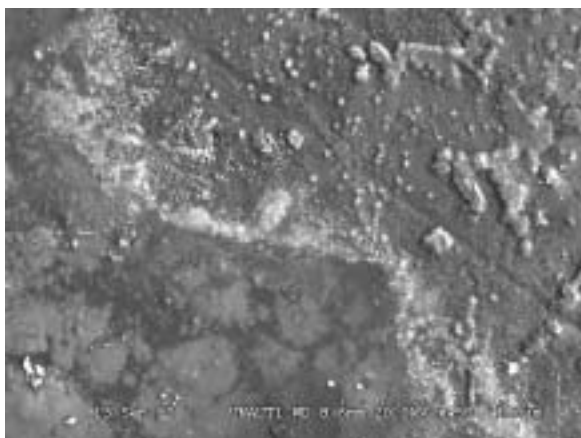
Fig. C71. This is a closer view of a string of U-rich nodules forming.
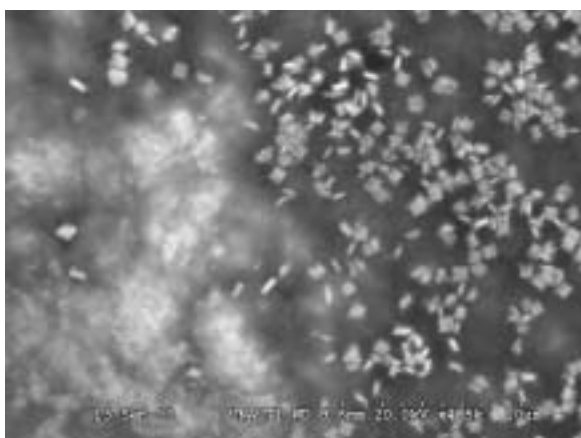
Fig. C72. Upon closer examination of the gel-region, some precipitated uranyl-oxyhydroxide platelets were found.
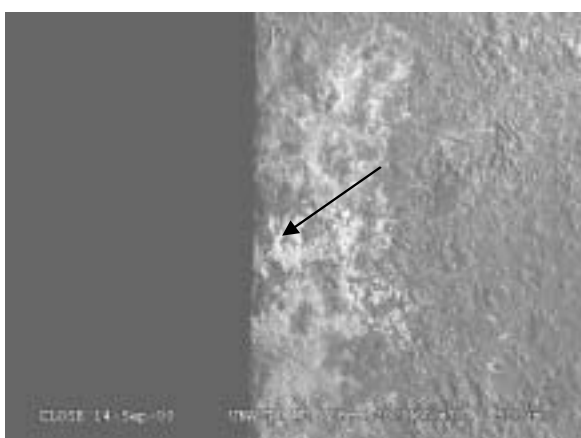
Fig. C73. Left-hand side of the fuel. A close-up of the region pointed out by the arrow is shown in Fig. C74.
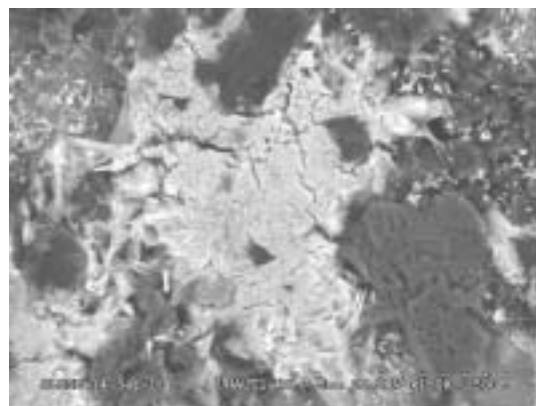
Fig. C74. This patch is poorly crystallized. Calcite precipitates (dark gray masses) nearly surround the uranyl-oxyhydroxide patch.
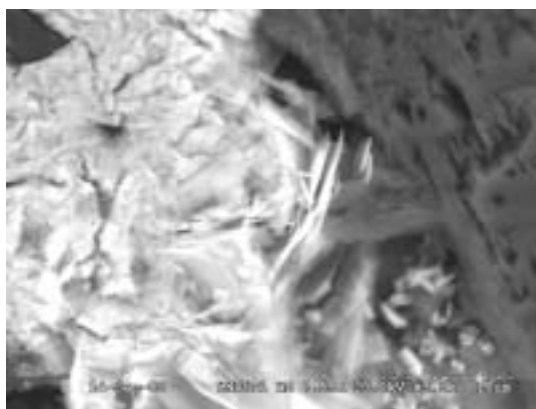
Fig. C75. A slightly closer view of Fig. C74. Calcite is to the right. Tiny uranyl-oxyhydroxide platelets can be discerned in between the calcite and the bright patch.

Fig. C76. Same view as in Fig. C75 except the accelerating voltage was reduced to 10 kV.

Fig. C77. A closer view of the left side of the patch in Fig. C74. Elongated structures are beginning to crystallize from the amorphous mass.
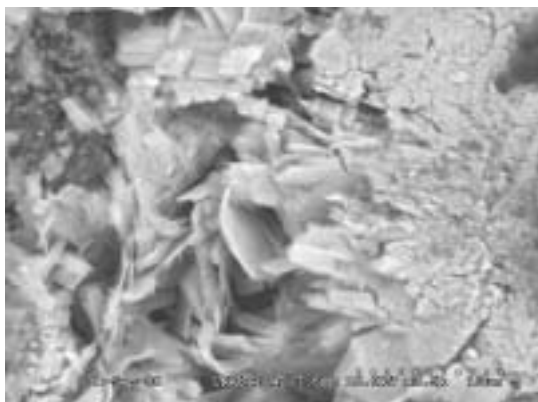
Fig. C78. This view of the patch is slightly lower than shown in Fig. C77.
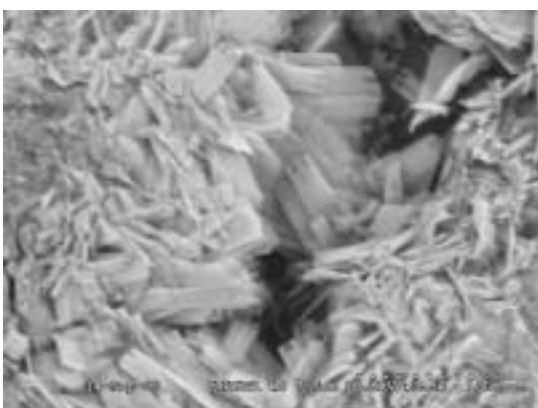
Fig. C79. Another patch nearby that shown in Fig. C78 has produced interesting elongated, flat structures rich in uranium. Note the triple terminations on these structures.
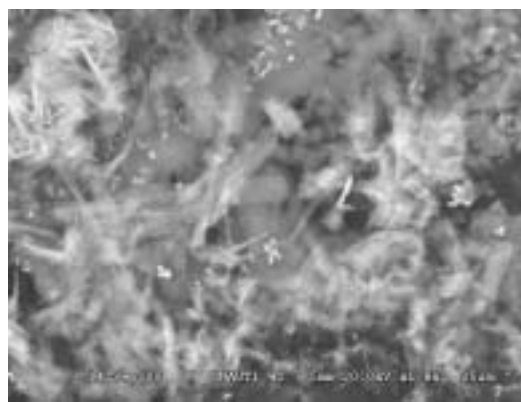
Fig. C80. Elongated structures were also found crystallized under the underlying gel.

Fig. C81. This is the same picture as Fig. C80 except that the accelerating voltage was reduced to 10 kV.
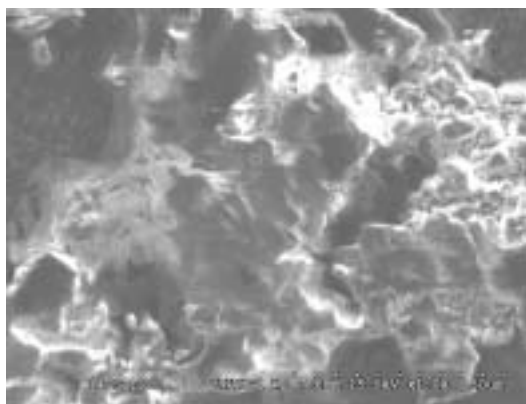
Fig. C82. Secondary image of the surface.
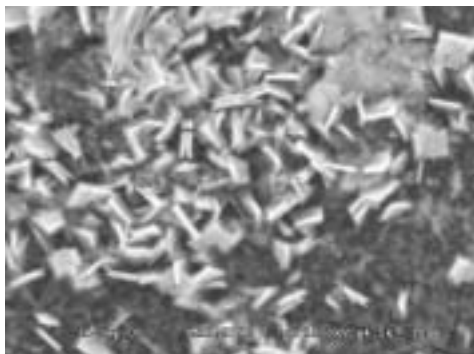
Fig. C83. A close-up view of the platelets formed on the fuel surface reveals that some are splitting, a typical phenomenon of schoepite as it dehydrates.

Fig. C84. A split-view image of the fuel surface (secondary image, left; back-scatter image, right). Patches of the uranyl-oxyhydroxides are shown.

Fig. C85. View of the smooth gel-region of the fuel at the bottom of the fuel. The mottled appearance is due to the UAl_x grains below the gel surface. The bright patch at center is the uranyl-oxyhydroxide patches seen in the previous images.

Fig. C86. These uranyl-oxyhydroxides are crystallizing in the Al-silica hydrogel. One can distinguish the elongated structures and platelets.

Fig. C87. A closer view of Fig. C86 shows the cracks in the gel surface.
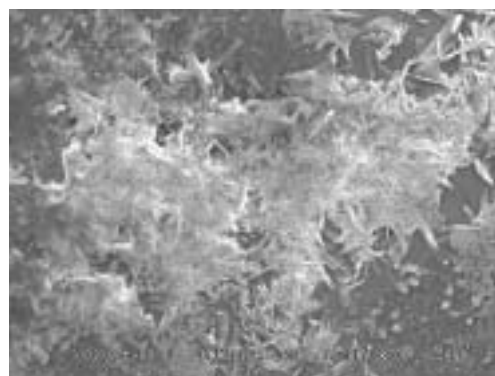
Fig. C88. This image is the same view as in Fig. C86 but taken at 15 kV.
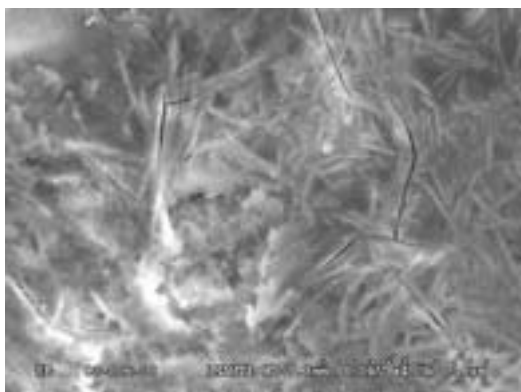
Fig. C89.   A lower accelerating voltage (10 kV) and secondary imaging produced this photo of the patch in Fig. C86.

Fig. C89.   A secondary image of Fig. C90 shows the uranyl surface structures.

Fig. C90.   The outline in this image shows a single UAl_x grain lying below the gel layer.

Fig. C91.   The outline of the UAl_x (gray) as seen through the gel layer (UOH=uranyl-oxyhydroxide).

Fig. C92.   A secondary image of Fig. C91 provides a look at the surface of the hydrogel.
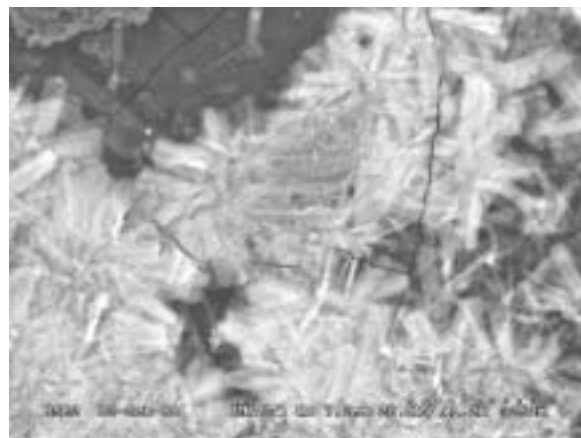
Fig. C93.   Cracks propagate through patches of elongated uranyl-oxyhydroxide crystals.
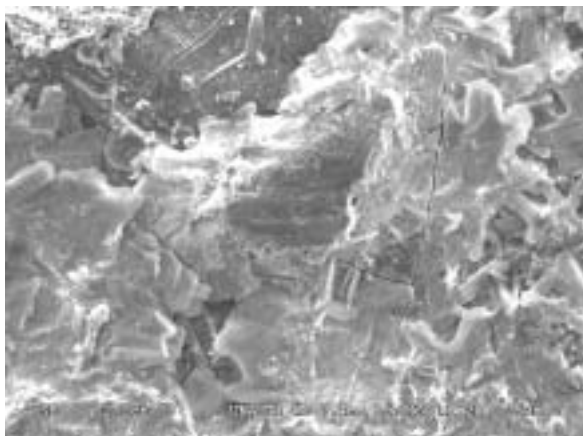
Fig. C94.   A secondary electron image of Fig. C93. Comparison between this surface image and the backscatter electron image of Fig. C93 highlights the growth of these elongated crystals within the gel layer.

The following set of pictures (Figs. C95-C103) shows the fuel UNAUT1 (571A) from the UAl$_x$ drip tests. The fuel was tipped on its side, mounted in epoxy, and polished with a diamond paste. In this manner, the thickness of the gel layer and the depth at which the fuel had been corroded could be discerned. A surface layer is apparent. In few areas of the fuel profile, one cannot distinguish the alteration/oxidized layer. This could be because the layer was dissolved away or was too thin to discern with the resolution of the SEM. Some U-rich material was seen in this layer, but EDS could not determine its composition because of the minute dimensions compared to the EDS spot size. The layer does contain appreciable amounts of Si along with the Al and O signals. At times Na, K, and Ca were found. The alteration layer varies in thickness and is shown as the medium contrast gray layer between the bright UAl$_x$ grains and the black epoxy.
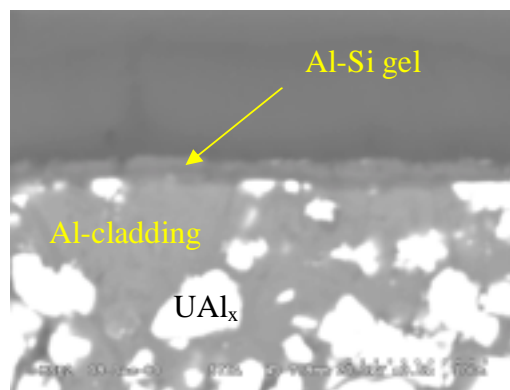
Fig. C95.
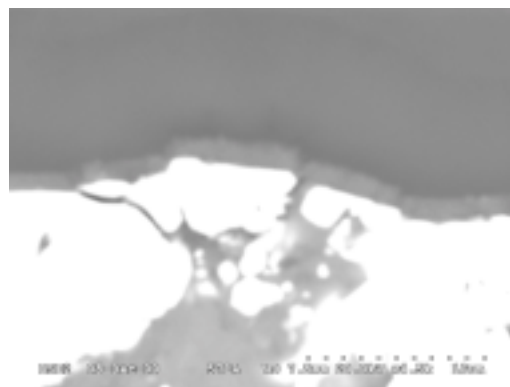
Fig. C96a.
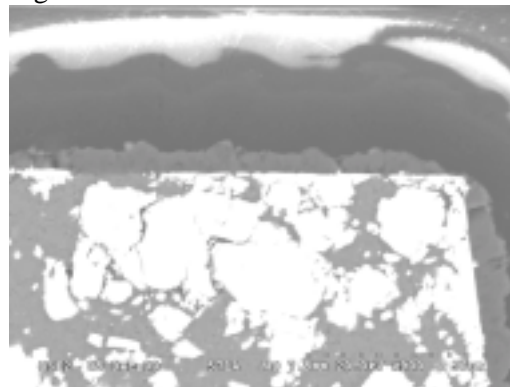
Fig. C96b.
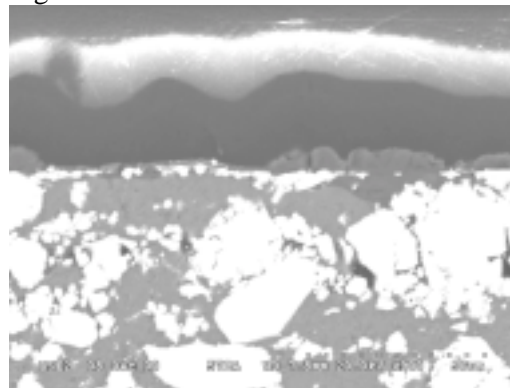
Fig. C97.
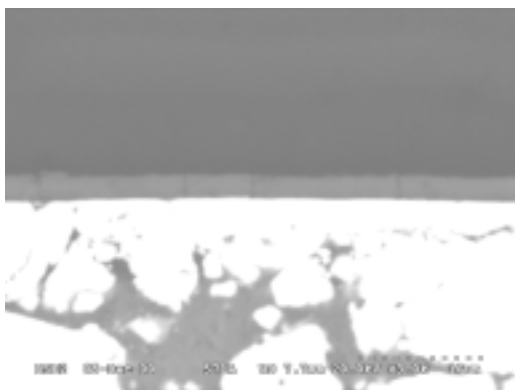
Fig. C98.
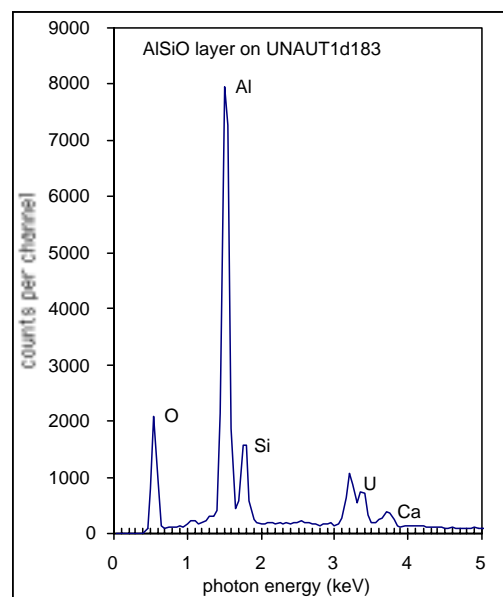
Fig. C99.

Fig. C100.

Fig. C101.   Spot A in Fig. C100.
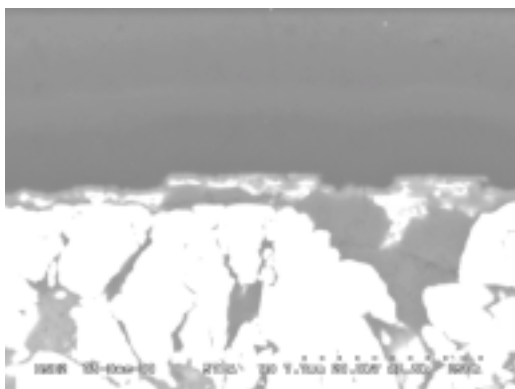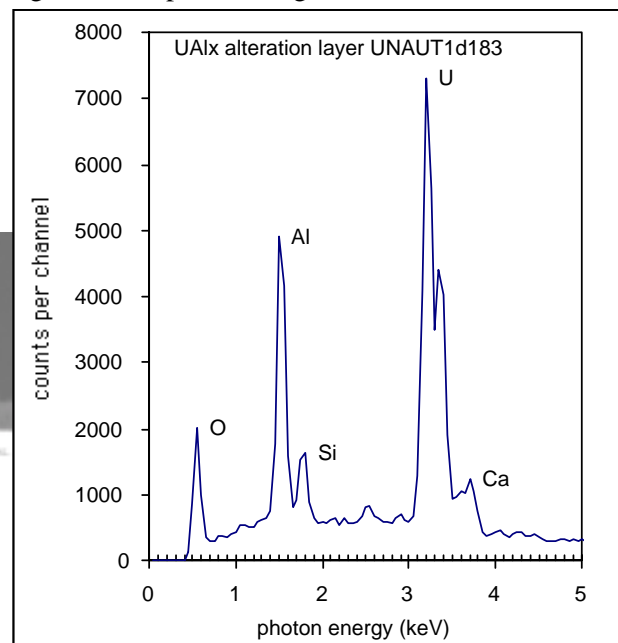
Fig. C102.   Spot B in Fig. C100.
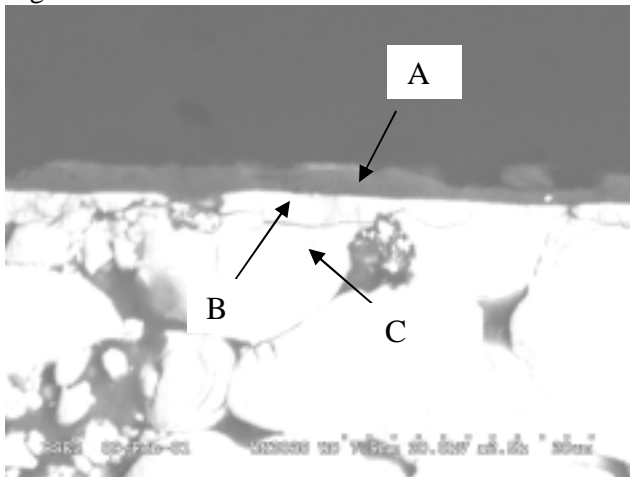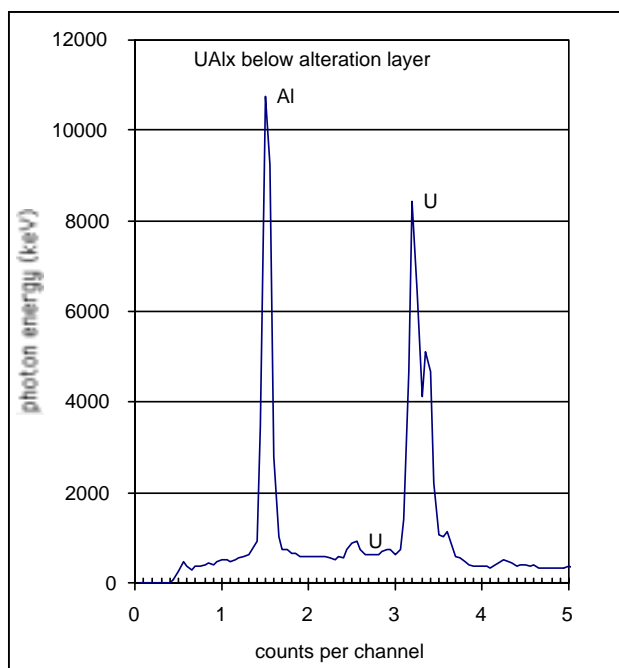
Fig. C103. Spot C in Fig. C100. This is the
          typical x-ray scan for UAl$_x$.

TEST UNAUT2 (FUEL PIECE 571C)

UNAUT2 after 16 Days of Testing
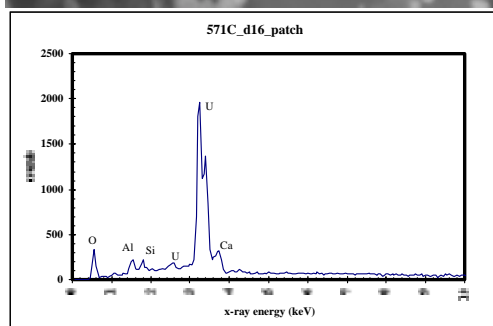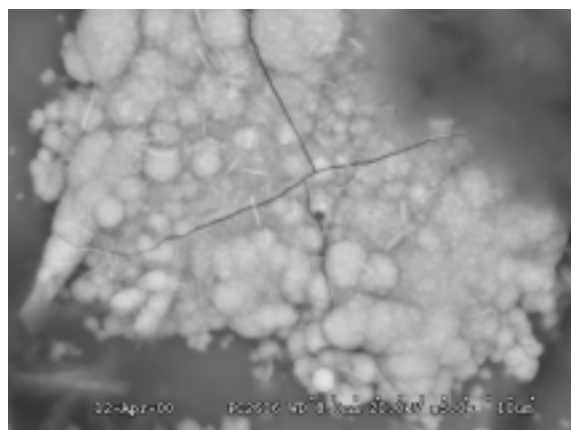
Fig. C104.   Closeup of uranium oxide patch. One can still see the remnants of the filaments (or the beginning growth of them). EDS shows uranium and oxygen and presence of Al, Si, and Ca. This is most likely an amorphous, hydrated uranyl oxyhydroxide containing inclusions of aluminosilicates.
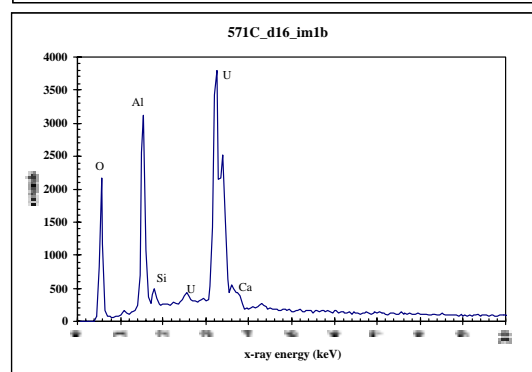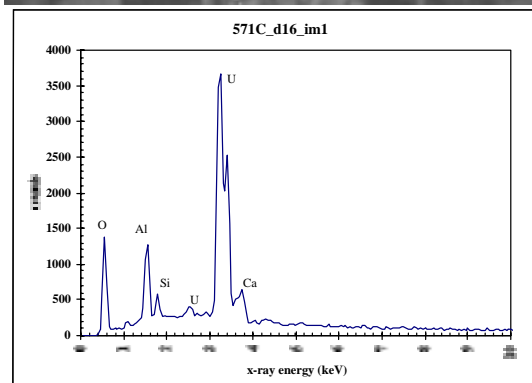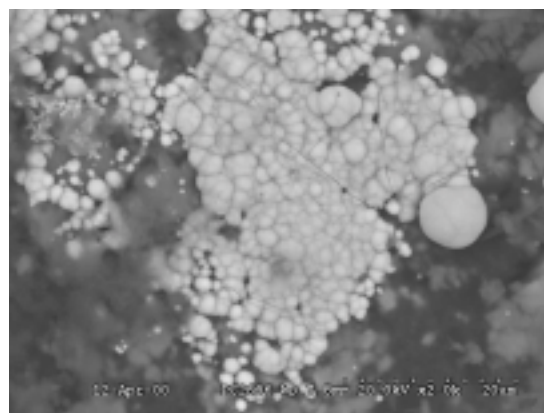
Fig. C105.   Closeup of uranium oxide similar to that observed in Fig. C104. EDS indicates strong uranium peaks along with aluminum, oxygen, calcium, and silicon.
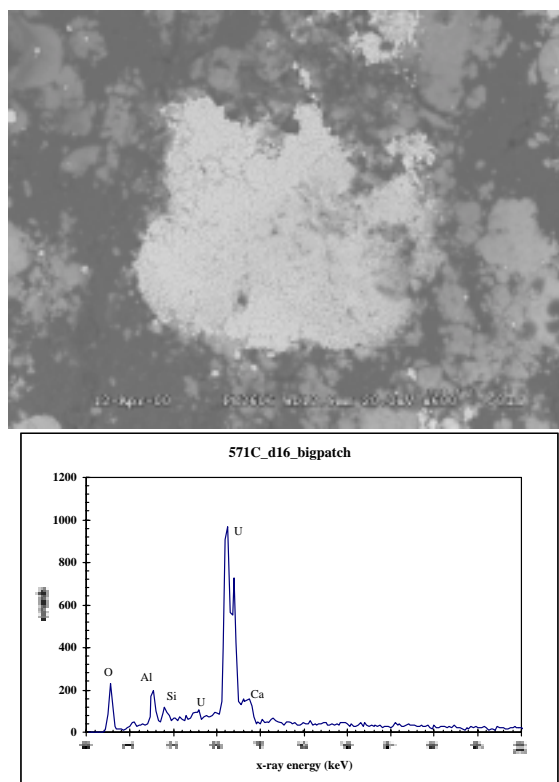
Fig. C106.   Large patch of uranium oxide
              EDS is shown.
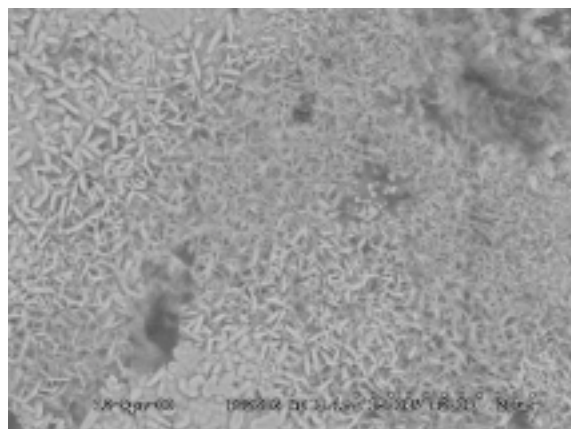
Fig. C107.   Closeup of the previous scan. A
              similar worm-like texture was
              described by Taylor (see text) as
              dehydrated schoepite.
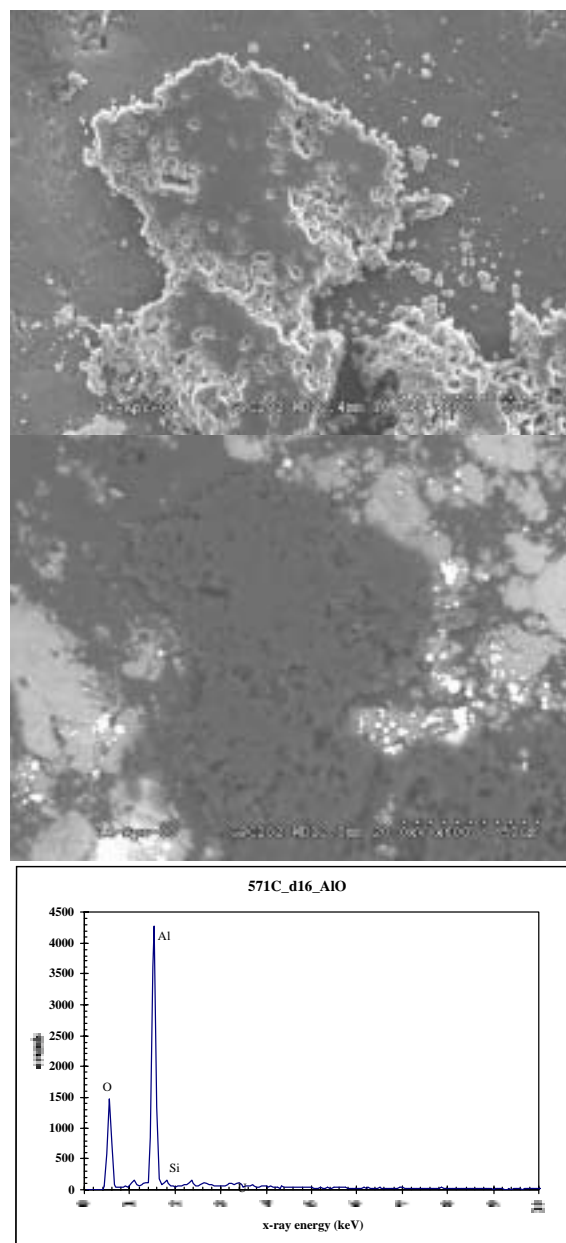
Fig. C108.   Secondary   and   backscatter
              images of patch of Al oxide.
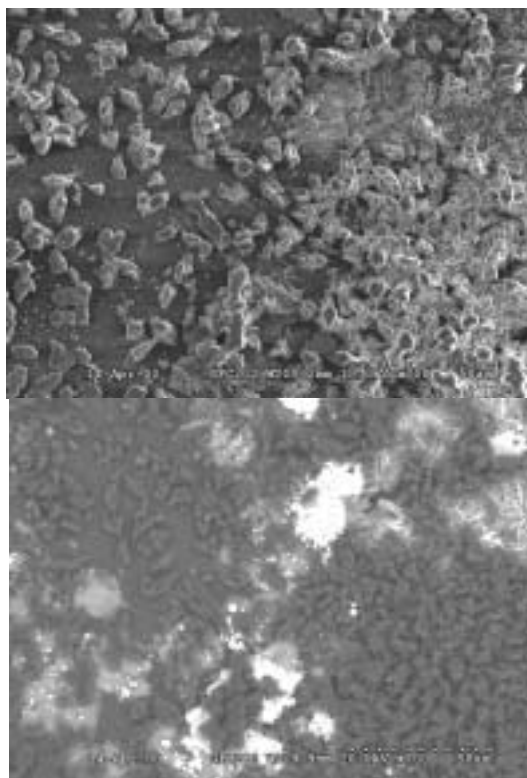
Fig. C109. Secondary and backscatter image of aluminum oxide grains (likely boehmite crystals). Some uranium-rich material can be seen in the backscatter electron images (white areas in lower photo).
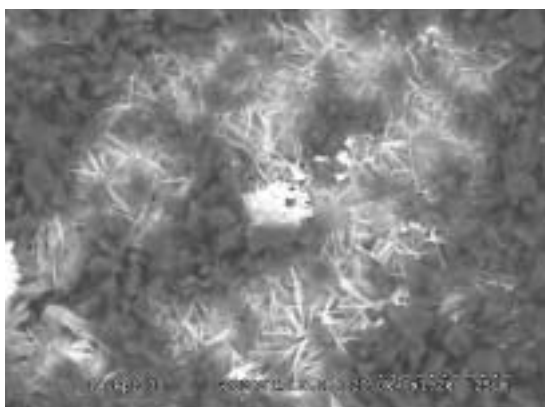
Fig. C110. Image of dendritic-appearing structures enriched in uranium and aluminum oxide crystals. When examined more closely, the uranium-enriched structures appear to be the familiar platelets. An agglomerated mass similar to that shown in Fig. C104 is in the center of the photo.
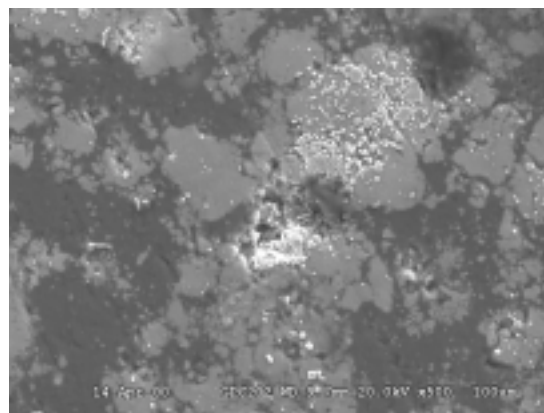
Fig. C111. In the center of this picture, a large crater hosts the growth of more pure uranium phases. Just below and above right is a patch of circular masses of uranium.
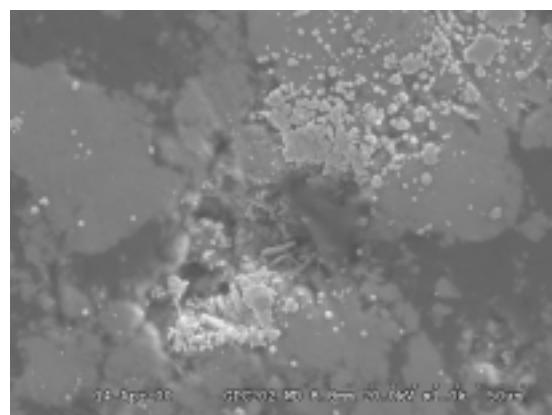
Fig. C112. Closer view of this hole from previous scan.

571C_d16_Uoxide3
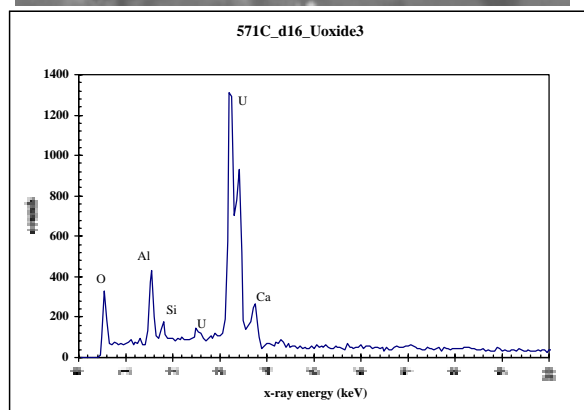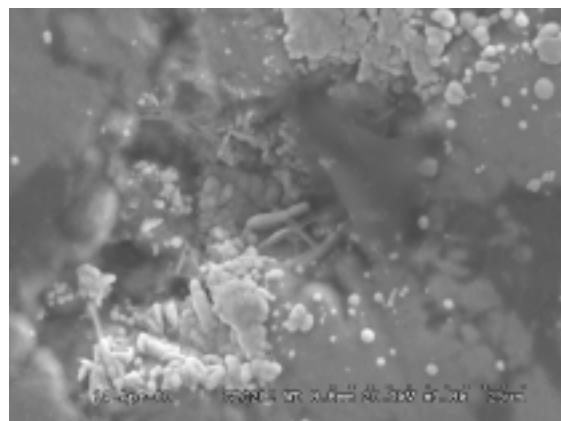
Fig. C113. Even closer image of the previous photos (EDS of white area of photo is shown).

571C_d16_AlO
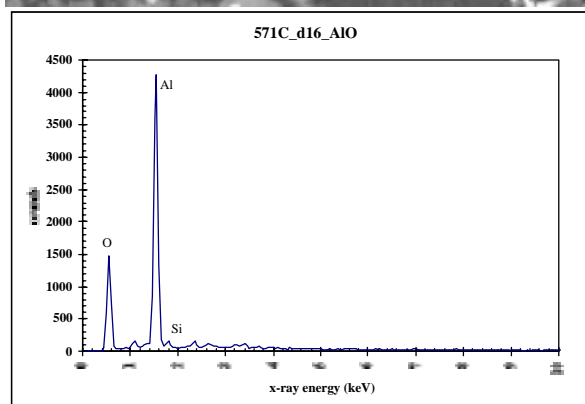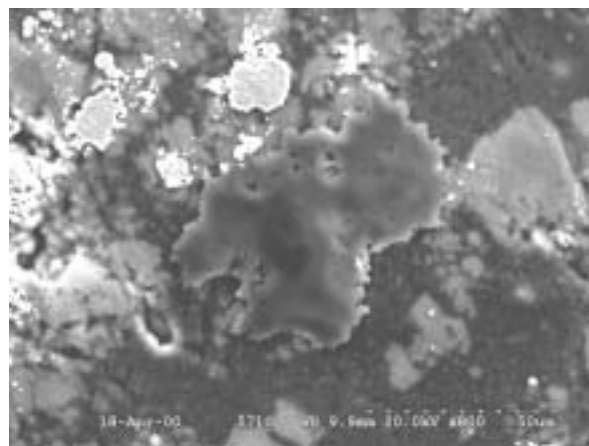
Fig. C115. An aluminum oxide patch. EDS spectrum of the oxide patch is shown.
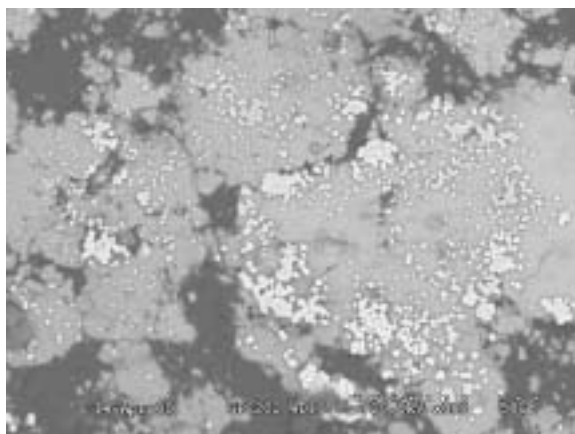
Fig. C114. The wide area view shows the speckles of uranium-rich deposits. Note that these deposits are found only atop a UAl_x grain (white background) and not found inside the Al oxide regions (black regions).

571C_d16_closer
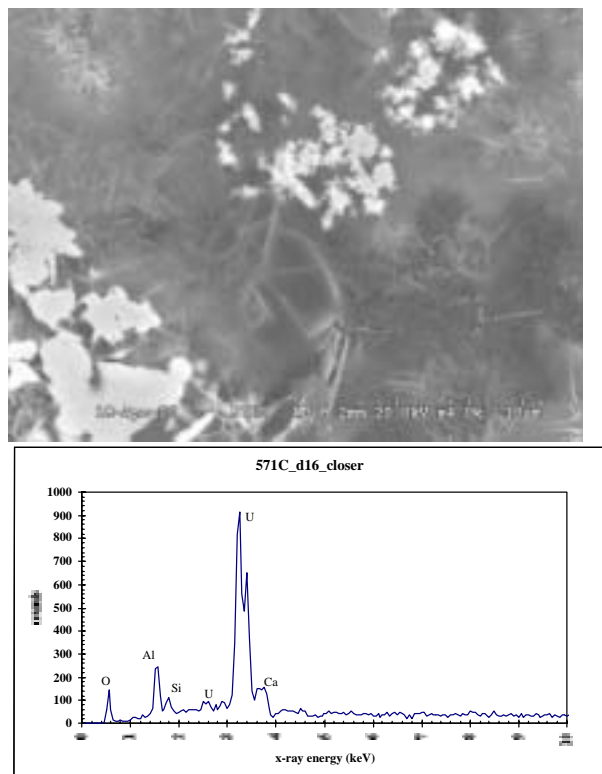
Fig. C116. Besides the small patches of hydrated uranium oxides, platelets can be seen embedded in the aluminosilicate hydrogel.
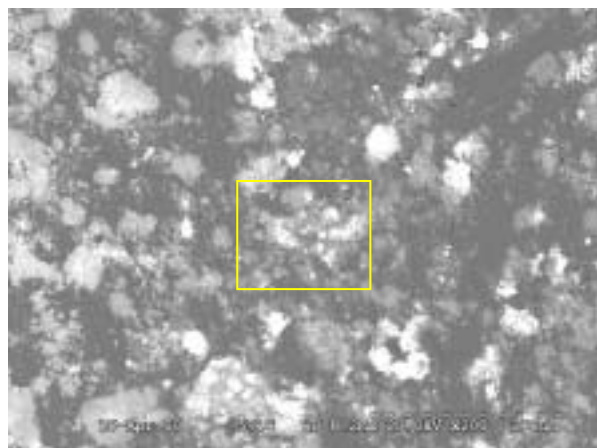
Fig. C117. This wide view shows the uranium-rich deposits residing atop UAl$_x$ grains.
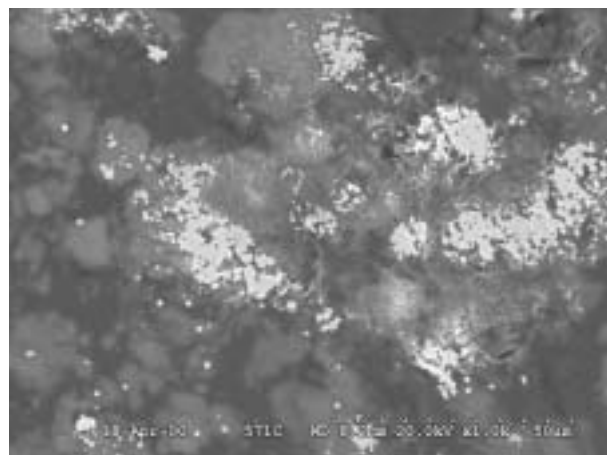
Fig. C118. Closer scan of Fig. C117 showing the region marked.
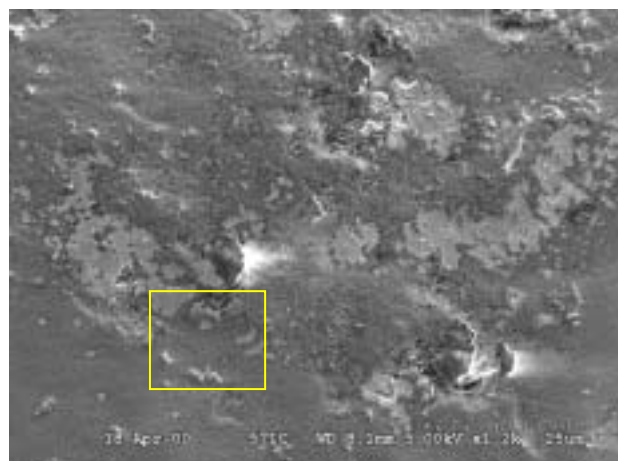
Fig. C119. This is a secondary electron reproduction of previous image but at 5 kV to show what the surface looks like. One can see that the uranium-rich deposits show up as smoothed, flat regions along the fuel surface. There is no evidence of UAl$_x$ patches here, i.e., no difference in the appearance of the surface.
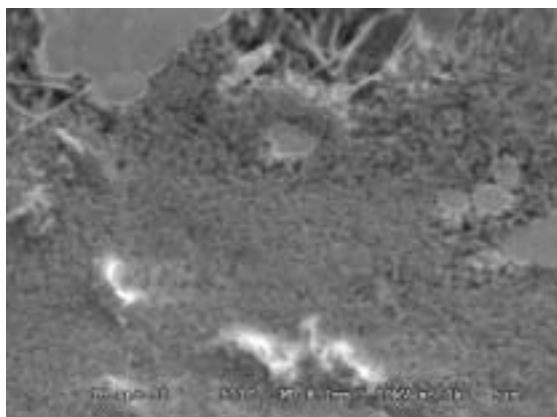
Fig. C120.   This close scan of the previous scan shows the refined grain structure on the hydrogel surface, a typical gel morphology.   Again, this is a secondary electron image at 5 kV.
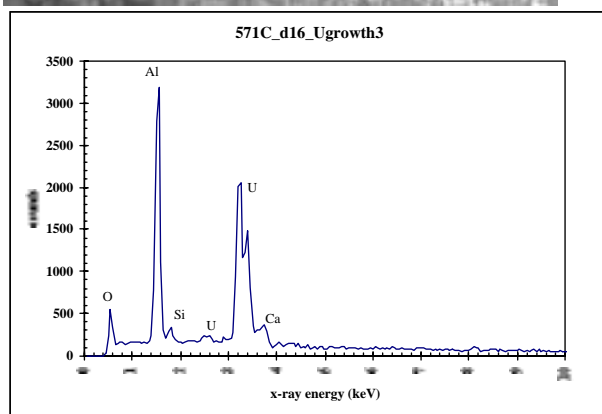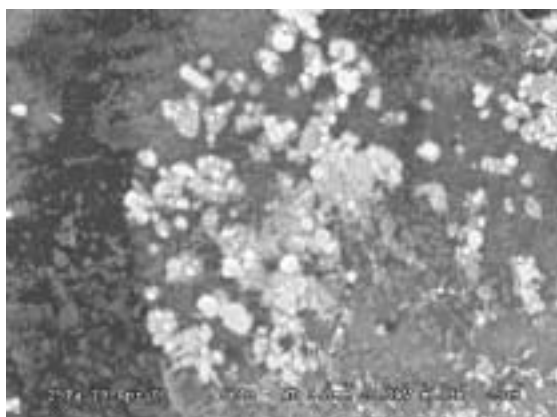
Fig. C121.   The growth of circular hydrated uranium oxides originates at the UAl$_x$-hydrogel interface.   The brightest areas are nearest to or exposed through the gel surface. These grow from larger masses (gray-white) still within and obscured by the hydrogel.
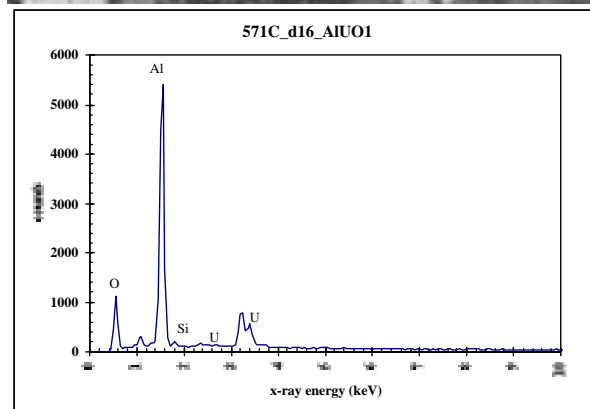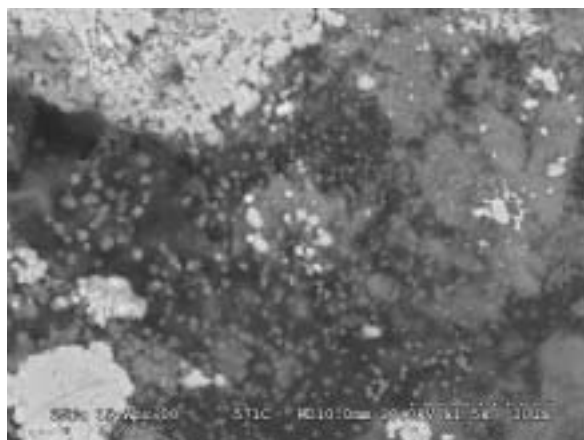
Fig. C122.   In this area of the fuel, the hydrogel was littered with inclusions rich in uranium (the gray-white circles).
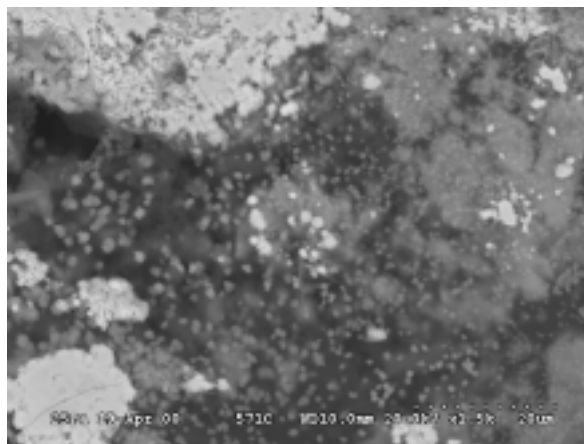
Fig. C123.   Same image as before with a different photo capture scheme.

571C_d16_Caparts
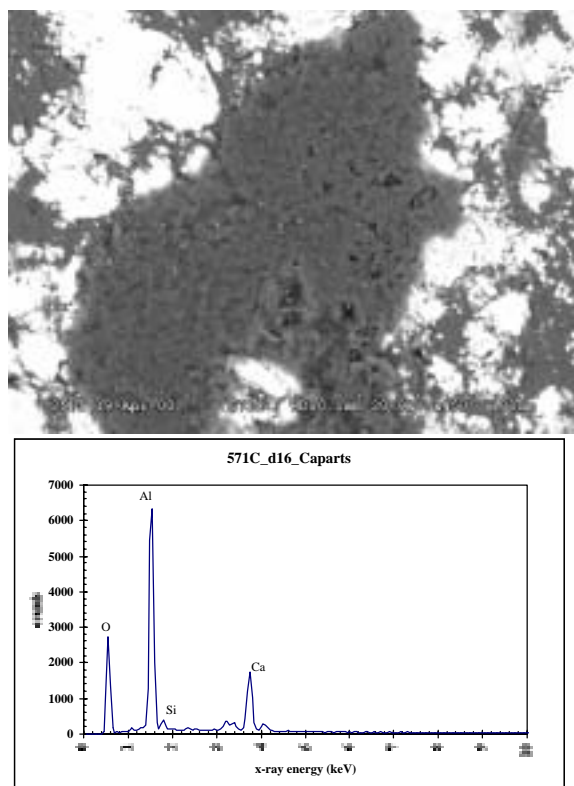
Fig. C124. Aluminum oxide bed surrounded by uranium oxide patches. The patch is speckled with light colored spheres that contain Ca.

571C_d16_UAlO2
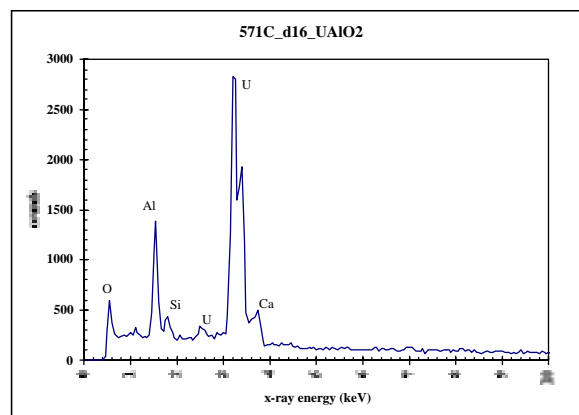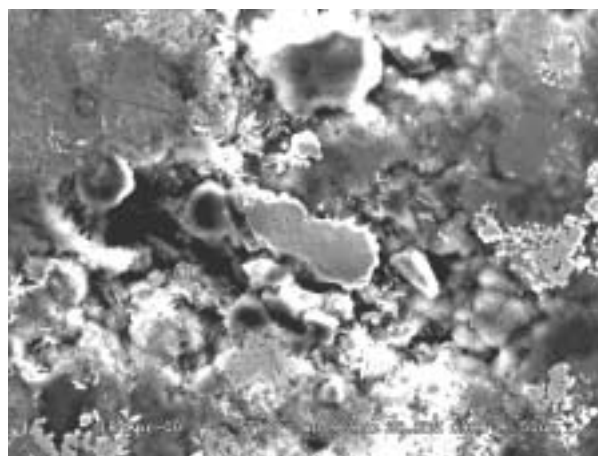
Fig. C125. This complicated mosaic of structures shows a large patch of uranium oxide in the center. EDS is of the central oxide.
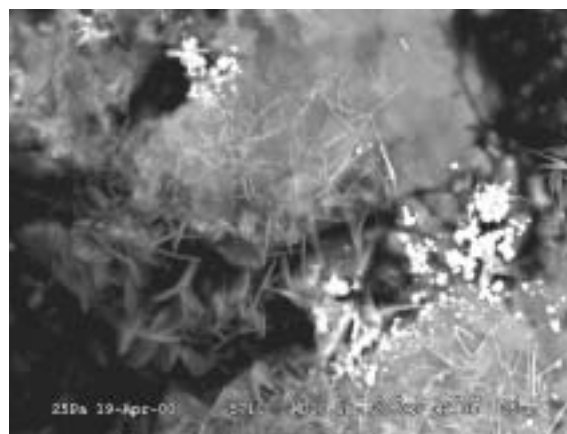
Fig. C126. Filaments appear to be growing in this region although they may, in fact, be the exposed edge of a thin platelet.
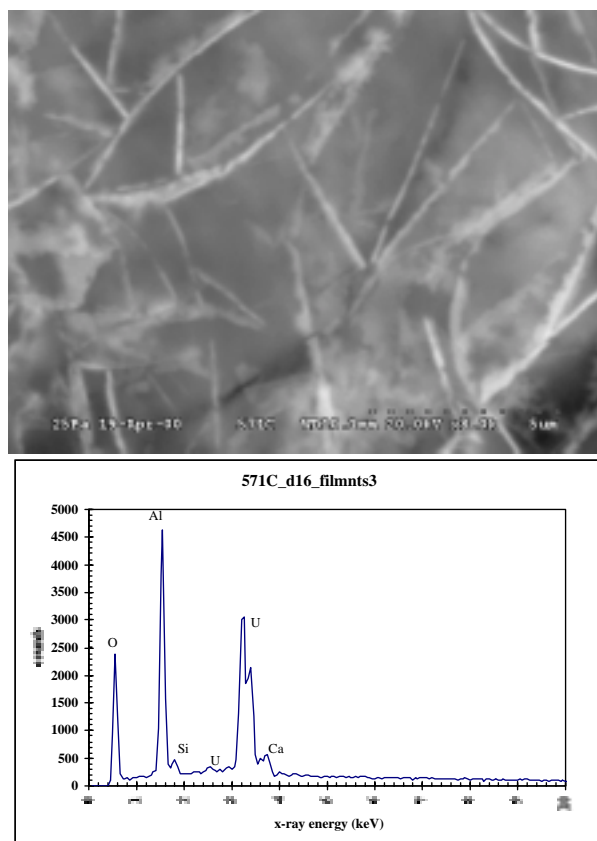
Fig. C127. Closer look at the filaments in Fig. C126.

The images shown in Figs. C128-C143 were taken by turning the fuel onto its side to reveal the profile of the meat and cladding, and polishing to 4000 grit paper. In most cases, the contrast was maximized to distinguish the small differences in density among UAl$_x$ phases and the hydrogel boundary.   Semi-quantitative analysis was performed with the PROZA technique installed with the EDS.   The pure UAl$_x$ phases served as a check to the accuracy of this semi-quantitative technique.
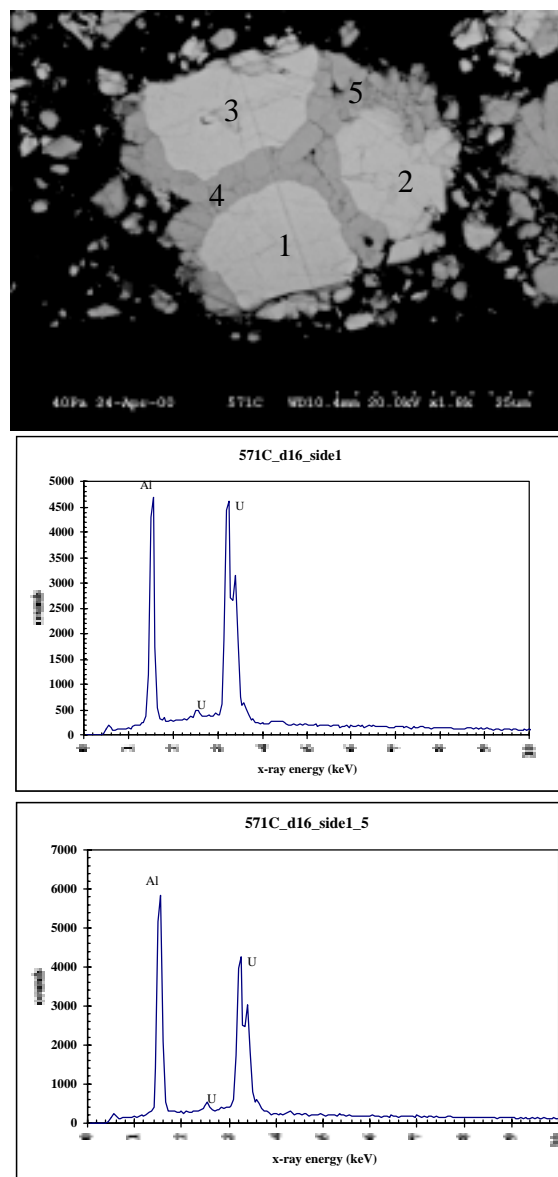
Fig. C128. EDS indicates a composition of 72% at % Al/28% U (regions 1, 2, 3), 5.6% Al/24.4% U (region 4), and 77% Al/23% U (region 5).
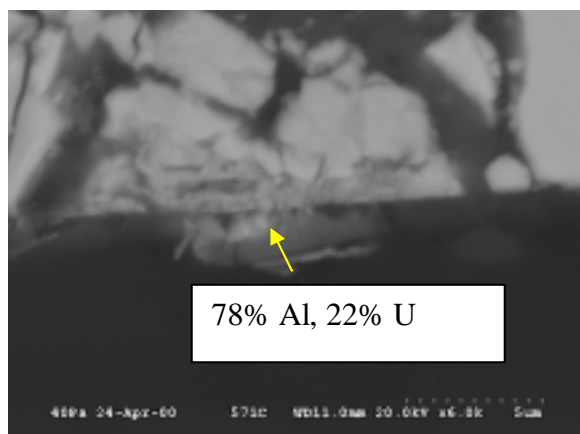
Fig. C129a. These U-rich structures have grown into the hydrogel and probably were exposed to the surface of the gel.

78% Al, 22% U

73.19% Al, 26.81% U with oxygen.

Fig. C129b.

Al with strong oxygen signal - hydrated Al_2O_3.

99.85% Al, 0.15% Si, no oxygen.
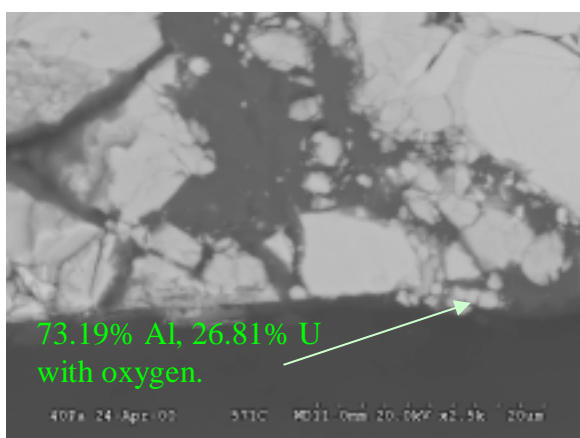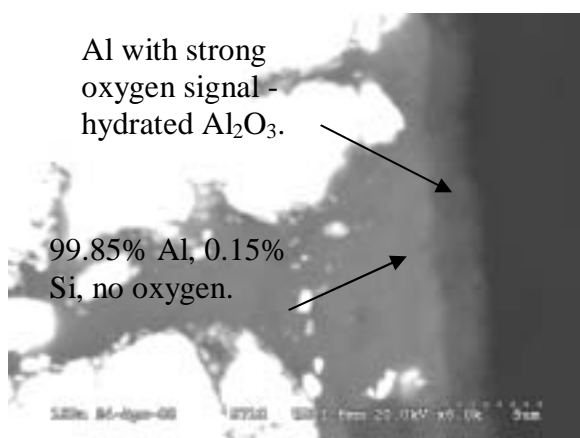
Fig. C130. Picture showing thickness of oxide layer on sample. According to the scale bar the oxide thickness is about 3 m after 16 days of testing.

76.6% Al, 7.2% Si, 16.2% U, with oxygen.
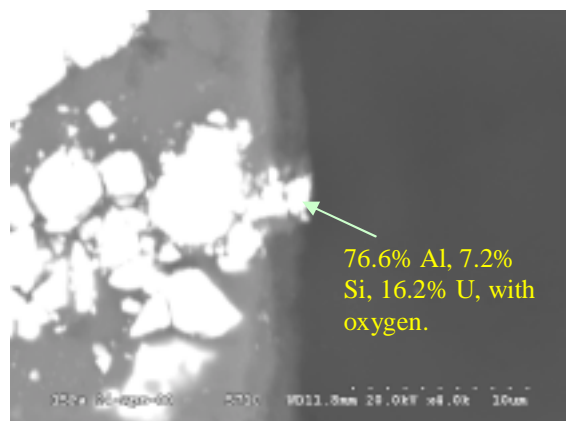
Fig. C131. Picture showing fuel meat protruding through the oxide layer.
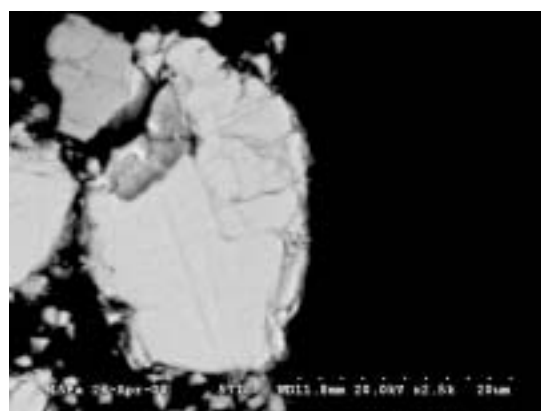
Fig. C132. Fuel showing an altered layer at surface interface.
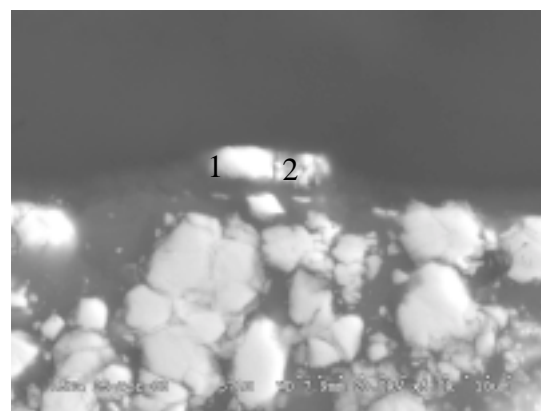
Fig. C133. EDS indicates a composition of 47% Al, 44% U, and 8% Si for left side of particle (bright side 1), and 58% Al, 34% U, and 8% Si for the right side (2). Both regions show oxygen presence.
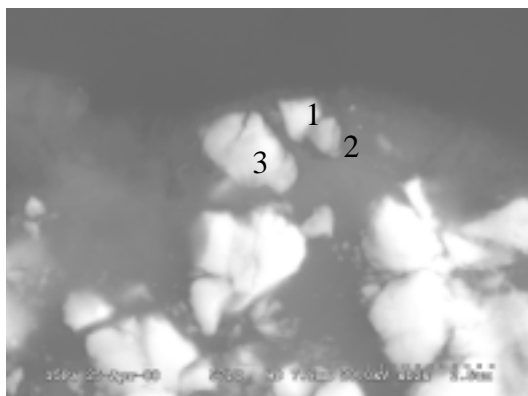
Fig. C134. According to EDS, the small shard closest to the top of the photo (1) is 90% Al, 8% U, and 2.5% Si (atom %) with oxygen. The smaller shard below that (2) is 90% Al, 5% U, with Si and oxygen. The big particle (3) is 90% Al, 10% U, plus oxygen.

These next pictures (Figs. C135-143) show aluminum-uranium phases at the boundary or protruding into the aluminum oxide layer. The important point here is that in all cases the uranium-aluminide is not pure UAl_x. The transformation seems to occur before the UAl_x reaches the oxide-metal interface and certainly before it breaks the surface to make direct contact with the air and dripped EJ-13. At least with this type of fuel composition and test conditions, galvanic coupling does not appear to protect the UAl_x from corrosion.
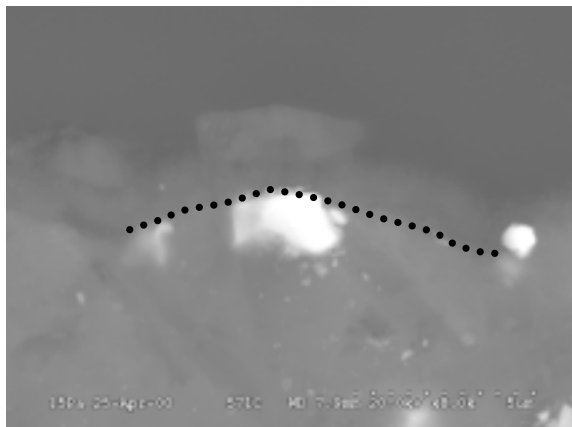
Fig. C135. Particle at the interface between the oxide and metal aluminum. The dotted line indicates this interface. EDS indicates a particle composition of 80% Al and 20% U with oxygen present.
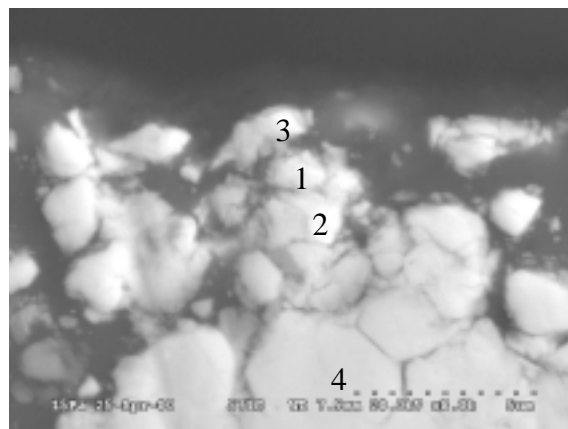
Fig. C136. The photo contains a variety of U-Al compositions. (1) 83% Al, 17% U with very little oxygen, (2) 80% Al and 20% U with very little oxygen, (3) 87% Al and 13% U and oxygen, (4) 74% Al and 26% U, no oxygen.
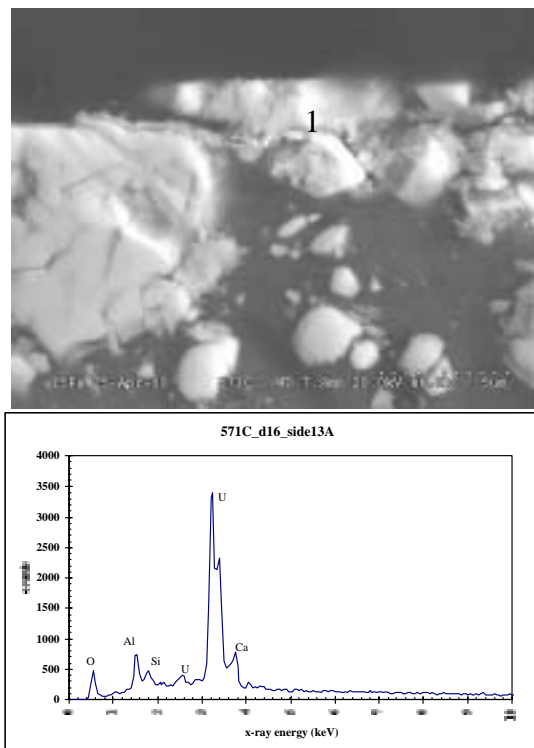
Fig. C137. This picture shows a highly transformed region of fuel with the top face exposed to the air and drips (1). EDS indicates about 50% U, 30% Al, and 10% Si. Ca is present but was not computed by EDS.
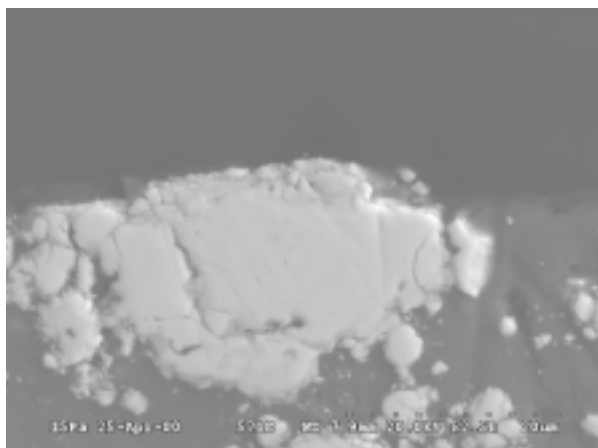
Fig. C138. Here is a full UAl_x grain with exposed top surface. The EDS of the grain body suggests that it is UAl_2, 66.2% Al and 33.8% U, with very little oxygen present (probably due to vacuum gas in instrument).
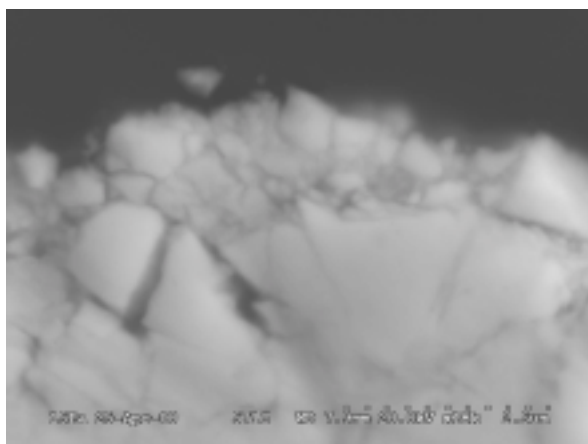
Fig. C139. This is a zoomed image of photo Fig. C138. The refined structure at the top suggests extensive transformation of the original UAl_x. EDS of this refined region suggests a composition of 46.8% U, 14.4% Si, 38.75% Al with oxygen and possibly Ca (?).
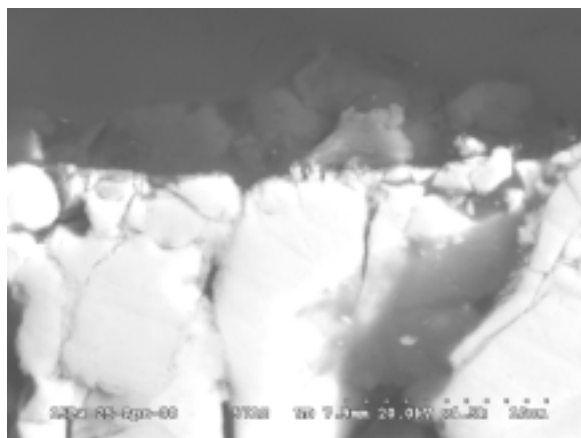
Fig. C140. This picture shows a chunk of Fe/Cr on fuel surface. This may have come from the vessel.
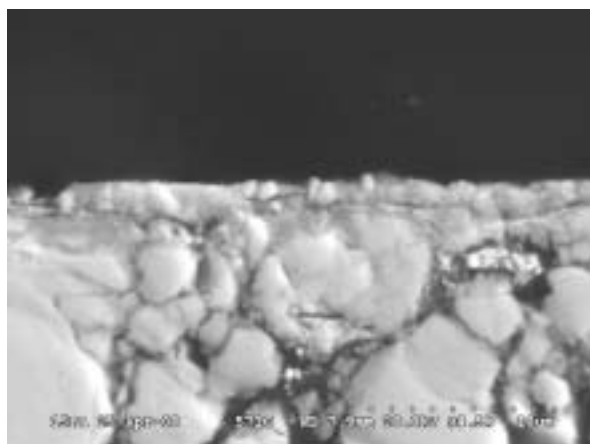
Fig. C141. An altered layer thickness of 1.5 m of similar composition as shown in Fig. C139.
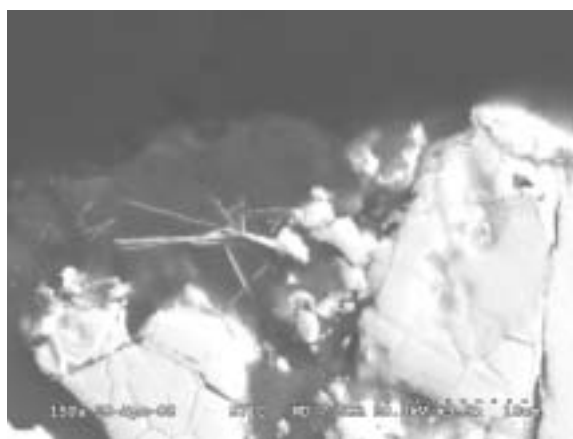
Fig. C142. Image shows what is probably the edge of a platelet growing inside the fuel as opposed to the fuel surface.
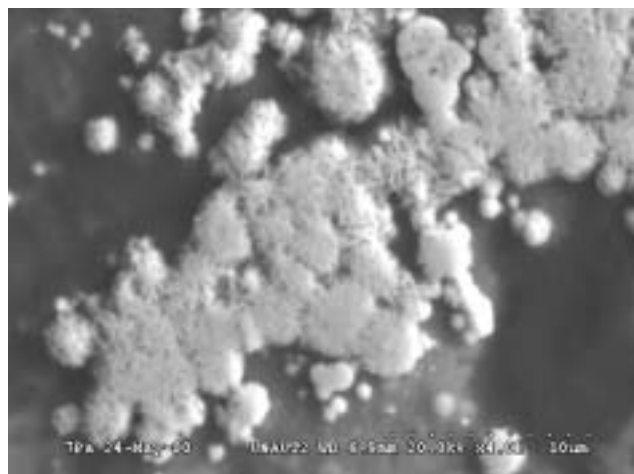
Fig. C143. After removing the sample from the epoxy, the surface was examined. The circular growths on the surface had dried and crystallized platelets.

The next set of images (Figs. C144 to C152) was taken of material scraped from the UNAUT2 fuel after initial examination, mounting for hydrogel examination (the previous set of photos), and removing from the mount. A razor blade was used to scrape the surface lightly. The scrapings were collected in ethanol and wicked through a holey carbon grid. No other explanation complements these photos. They are included for the sake of completeness.
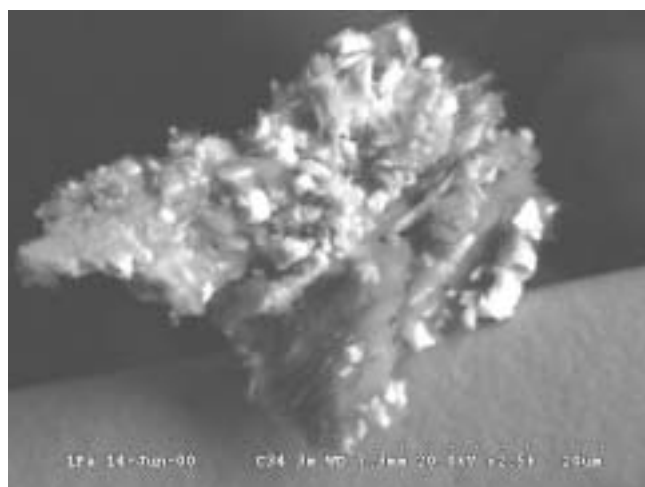
Fig. C144.
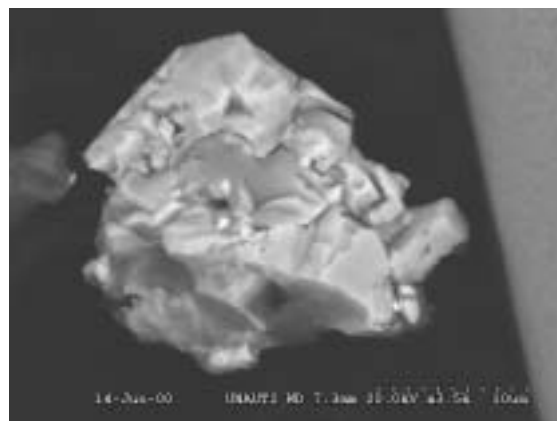
Fig. C145.
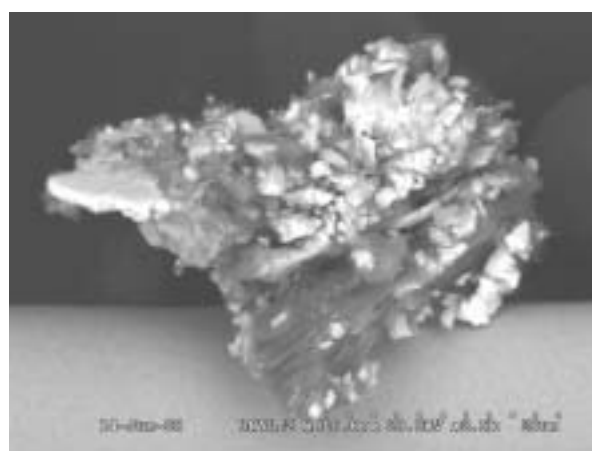
Fig. C146.
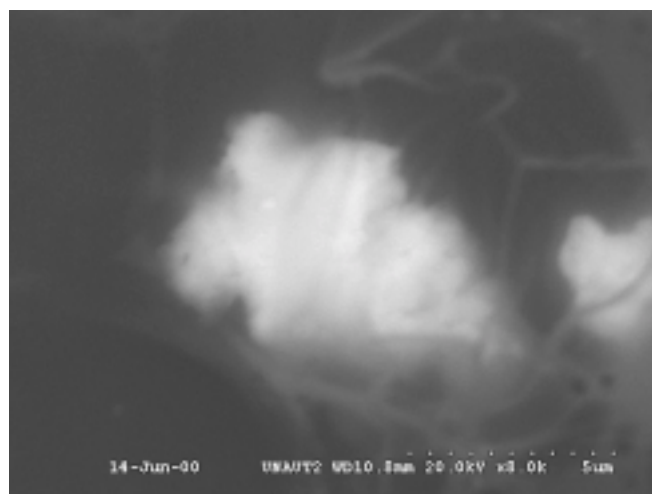
Fig. C147.
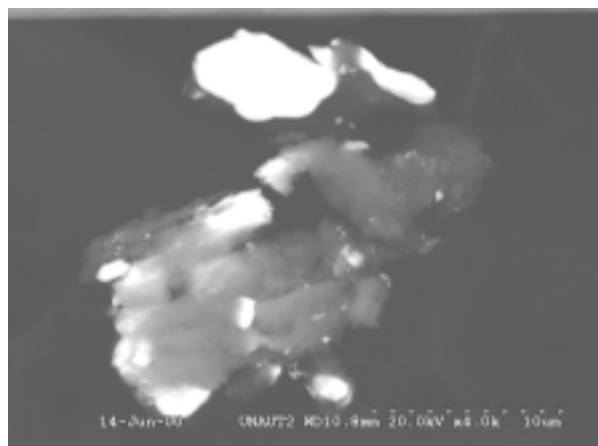
Fig. C148.
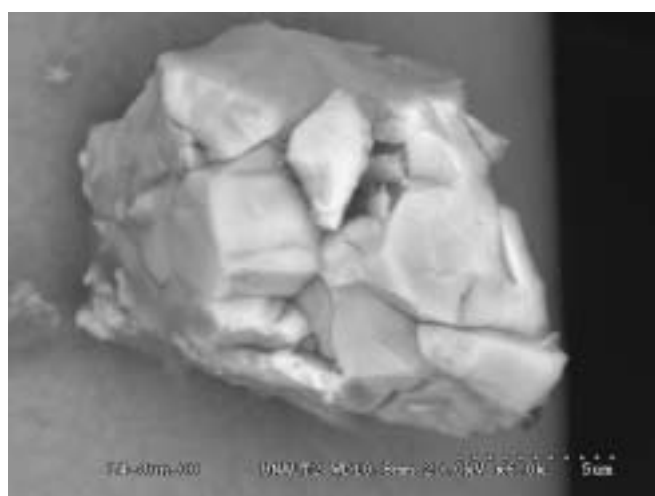
Fig. C149.
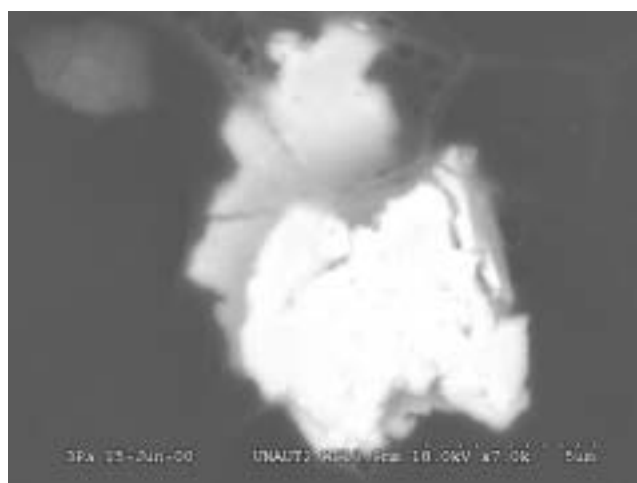
Fig. C150.
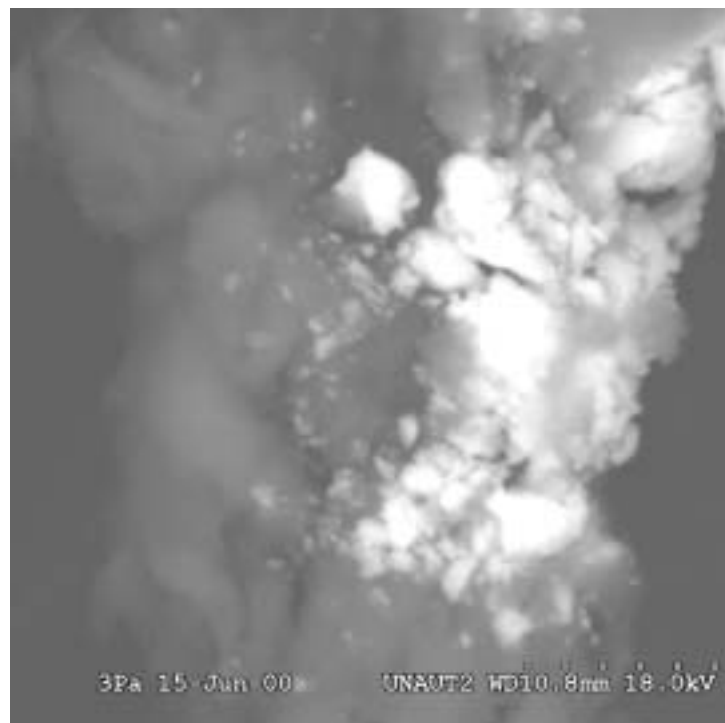
Fig. C151.
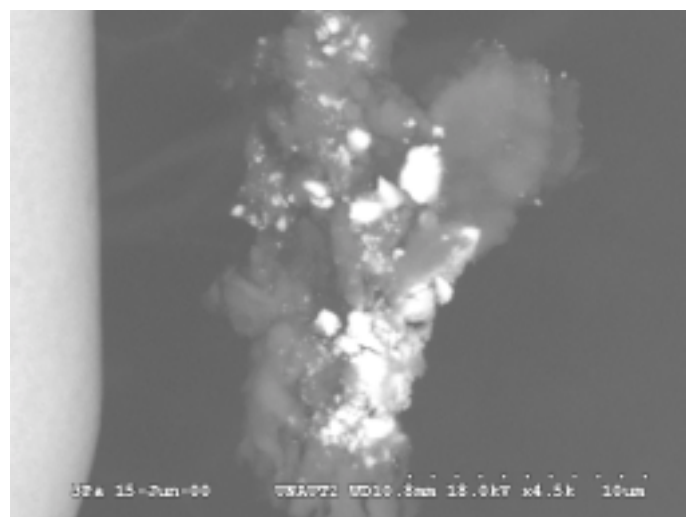
Fig. C152.

UNAUT3 FUEL PIECE (571C)

UNAUT3 after 55 Days of Testting

This set of images was taken after polishing the 571C coupon from test UNAUT2, restarting test numbered UNAUT3, and sampling after 55 days.
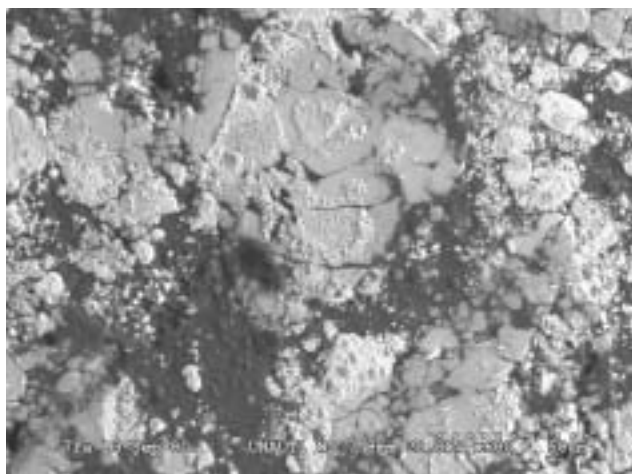

Fig. C153. The hydrogel that formed during this test was not as thick as in previous tests. Some areas appear very white in contrast, while others appear to be shadowed. This shadowing is due to the presence of the hydrogel. The hydrogel is not thick enough to completely obscure the underlying UAl_x phases. In some areas it appears to be absent (bright white areas).
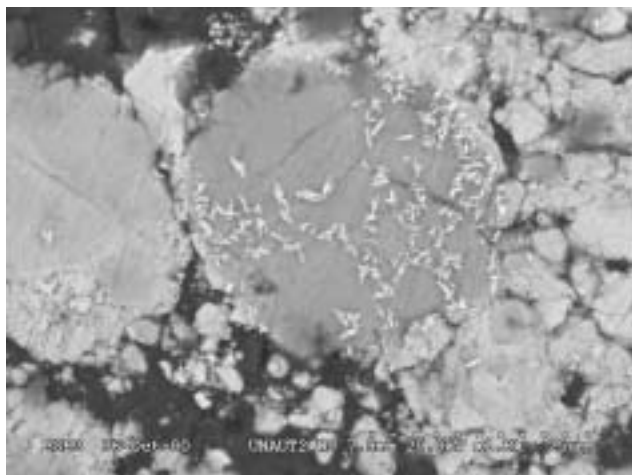
Fig. C154. Platelets have crystallized in a region where the hydrogel can be distinguished (the large, gray circular patch in center).
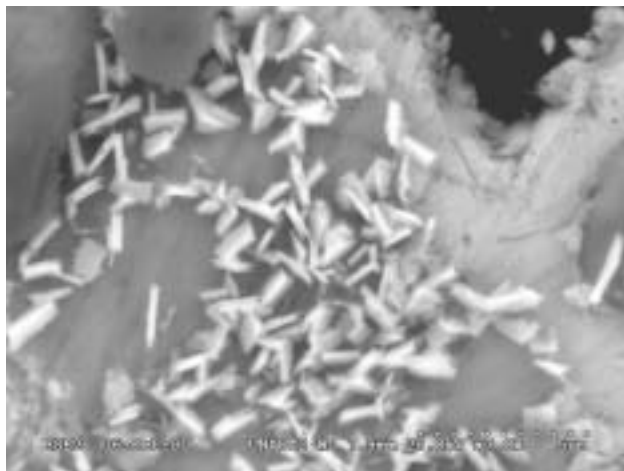

Fig. C155. A closer look at some of these platelets formed on the fuel surface.
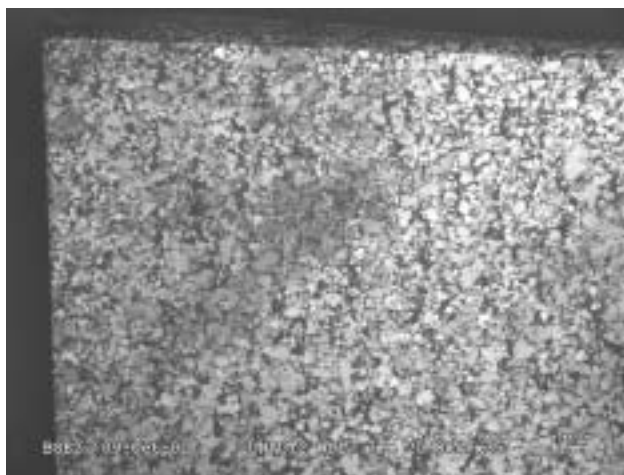

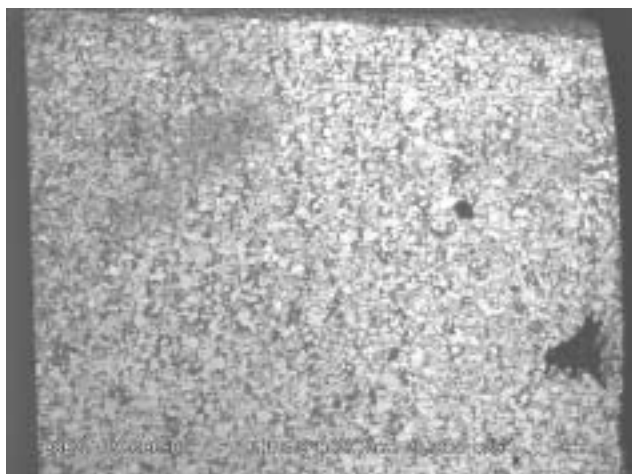Fig. C156. This image and Fig. C157 are wide views of the fuel surface.

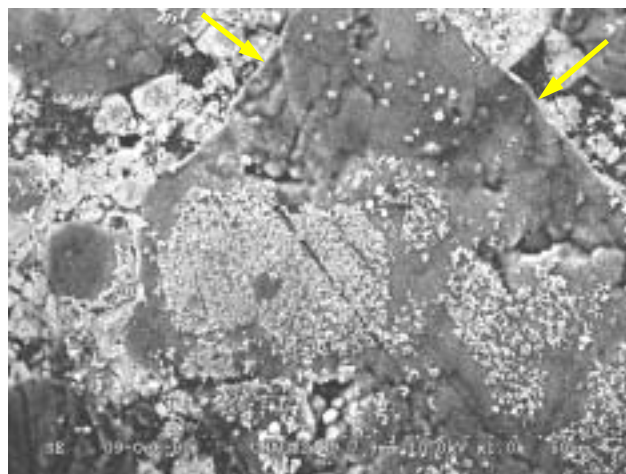Fig. C157. Almost the entire fuel face can be seen.

Fig. C159. Secondary electron image of Fig. C158. In this imaging mode, one can discern the hydrogel (see arrow at edge of hydrogel).
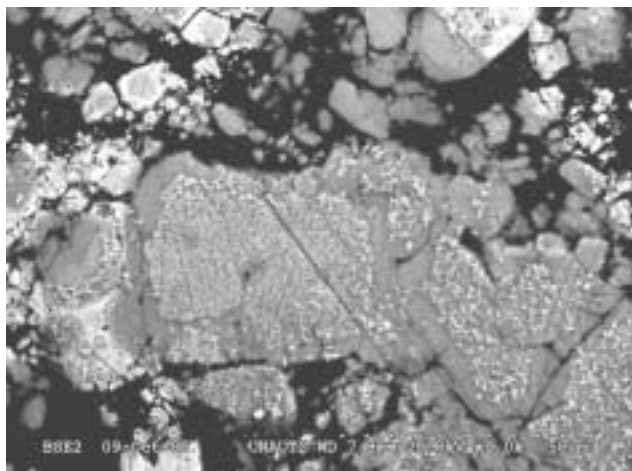

Fig. C158. Image of UAl_x grains and alteration products formed on its surface. Note how the platelets form near the center of the UAl_x grains, while the edges tend to be free of platelets. This may be evidence of the varied stoichiometry within a single UAl_x grain. The edges tend to be closer to UAl_4, which is thermodynamically more stable and less susceptible to corrosive attack, while the center of the grains is UAl_2.
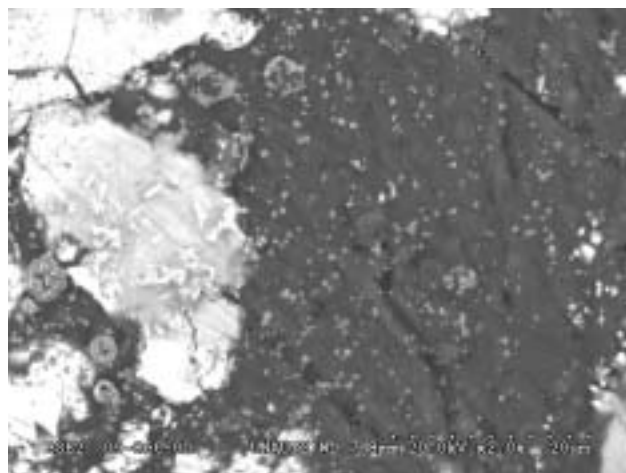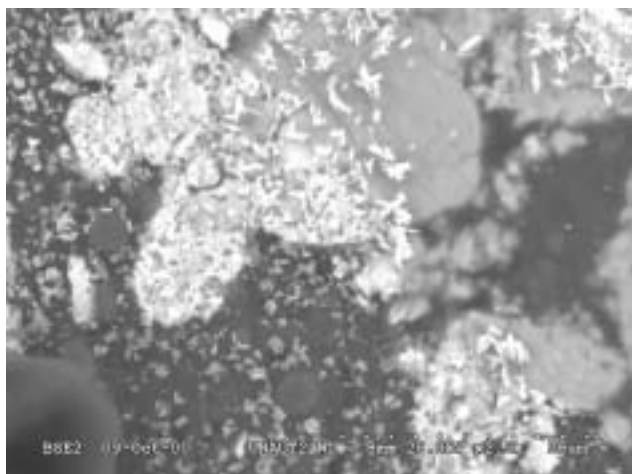

Fig. C160. Tiny platelets were formed in the hydrogel.

Fig. C161. The hydrogel is visible in the right-hand side of this image, while the left-hand side appears to be gel-free.
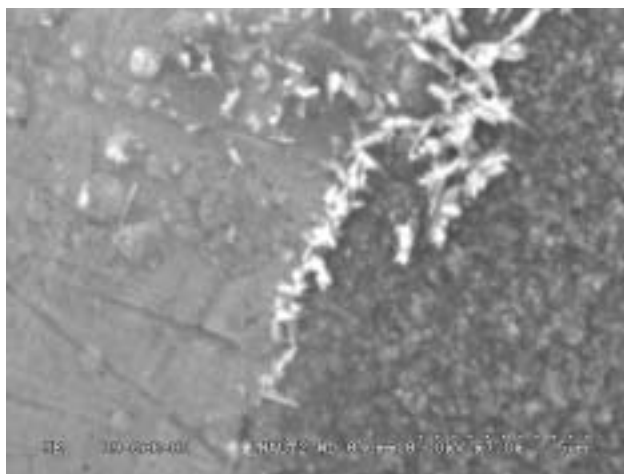

Fig. C162. Secondary-electron image of some platelets.

Fig. C163. Same as Fig. C162 except at a lower accelerating voltage (V=10 kV).

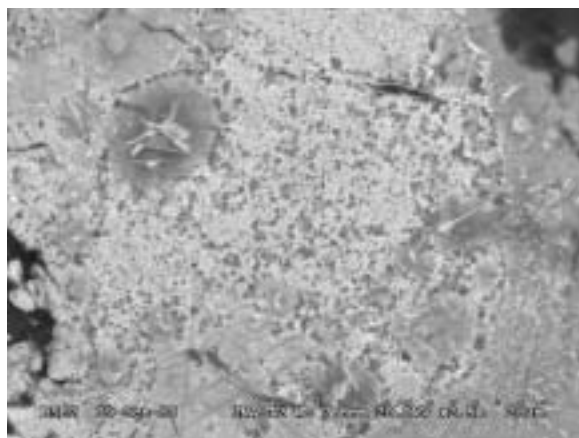Fig. C164. Platelets crystallize at the gel-front. The hydrogel is drying from left to right.

Fig. C165. This UAl_x grain has increased porosity due to the oxidation and dissolution of the Al.

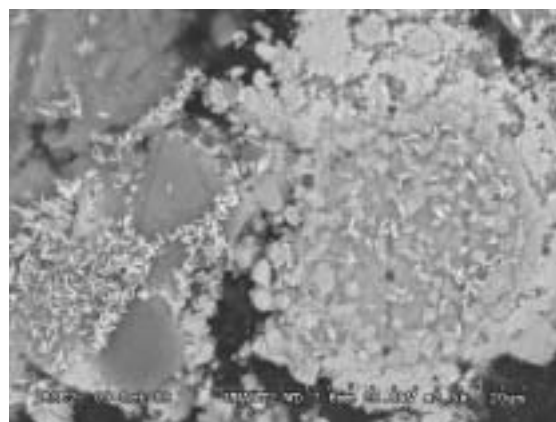Fig. C166. The UAl_x grain at right appears to be corroded in a similar manner as those appearing in Fig. C165. Platelets have crystallized at left.
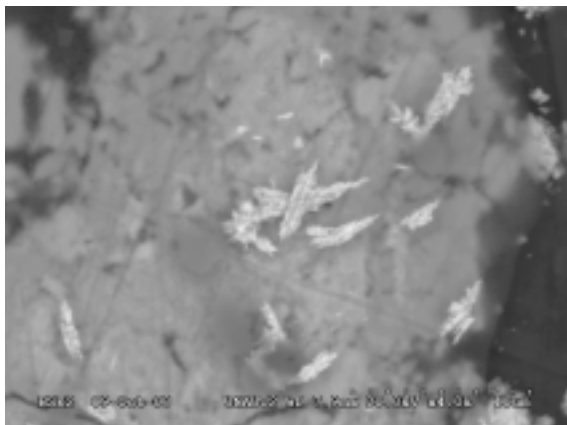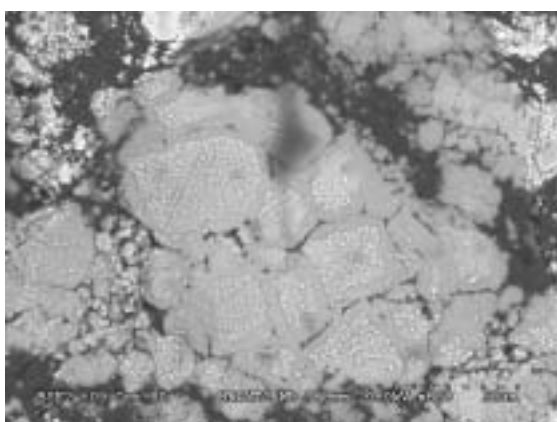
Fig. C167. U-rich participates.

Fig. C168. As in Fig. C158, the platelets form in the center of UAl$_x$ grains. If the corrosion process is characterized by oxidation, dissolution, and precipitation as an aqueous-based mechanism, one would expect the platelets to form without preference to location. Images like this lend support to the idea that a solid-state corrosion mechanism is responsible for the initial oxidation mechanism.
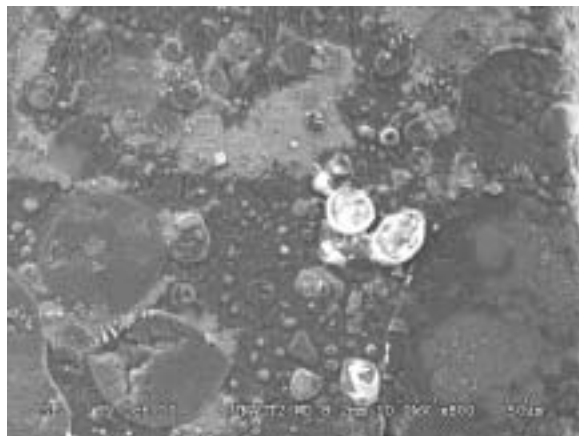
Fig. C169. This is a secondary image of an area of the fuel surface.

Sample 571C from UNAUT3, day 55 was embedded in epoxy and polished to a very fine grit, the same as for 571A after day 183. The alteration layer is not as ubiquitous as seen in the other sample (571A after day 183) but was seen in places. SEM of the surface confirmed the patchy nature of the gel layer film. EDS revealed Si in these layers with variable intensity. The hydrogel is shown as the light gray layer below the white of the UAl$_x$ in Figs. C170-C172.

Fig. C170.

Fig. C171.
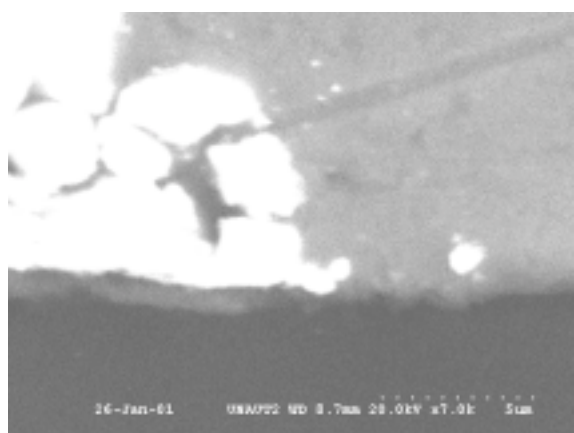
Fig. C172.

APPENDIX D

Transmission Electron Microscopy Reports for Analysis of Aluminum Fuel Mock Test Samples

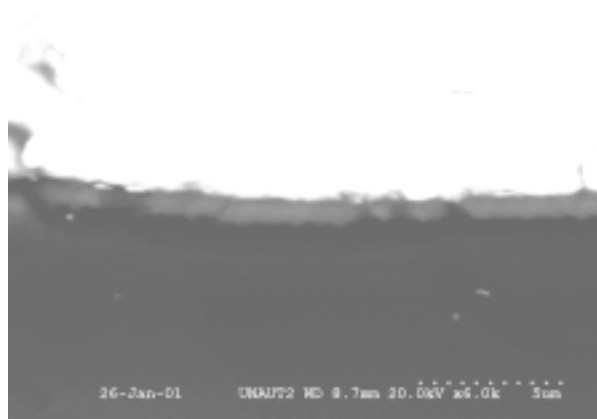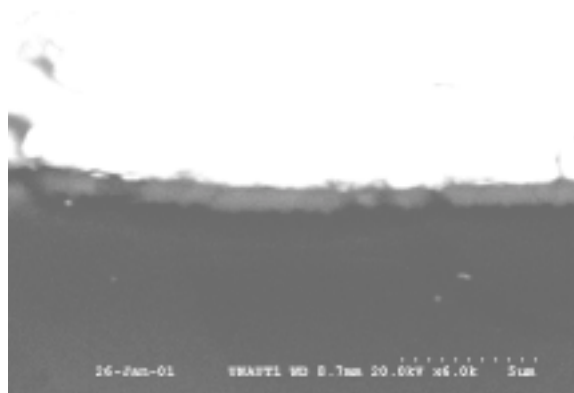Analytical reports from the TEM laboratory follow. The reports appear as they were when submitted to the author from the TEM laboratory. The reports have undergone only minor formatting changes.

AEM Survey Report on DOE-SNF Corrosion Tests
Analyzer: Edgar Buck
Date: May 2000

This sample is from a long-term drip test. Colloidal particles collected from the leachate were analyzed along with the corroded surface. Particles were scraped off the metal surface and deposited directly onto a holey carbon grid.

Table.1 Sample UNAUT2-D16

Grid No.	NoteBook Ref.	Block No.	Comments
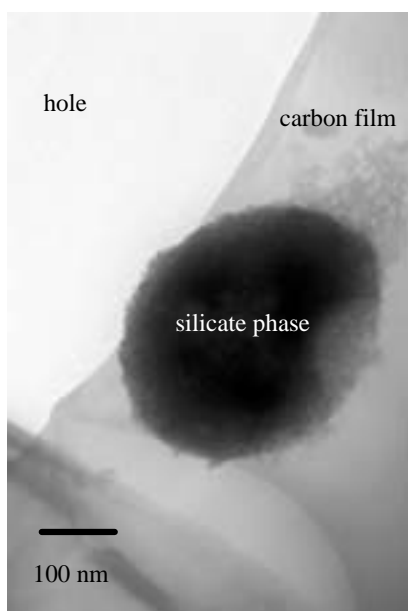
Fig. 1. Apparent colloids from U-Al metal drip test. Some were found as isolated particles, most were large agglomerates.
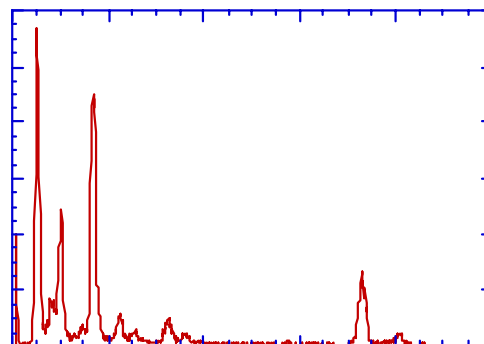
Fig. 2. EDS analysis of particle. No uranium or aluminum was observed in the particles.
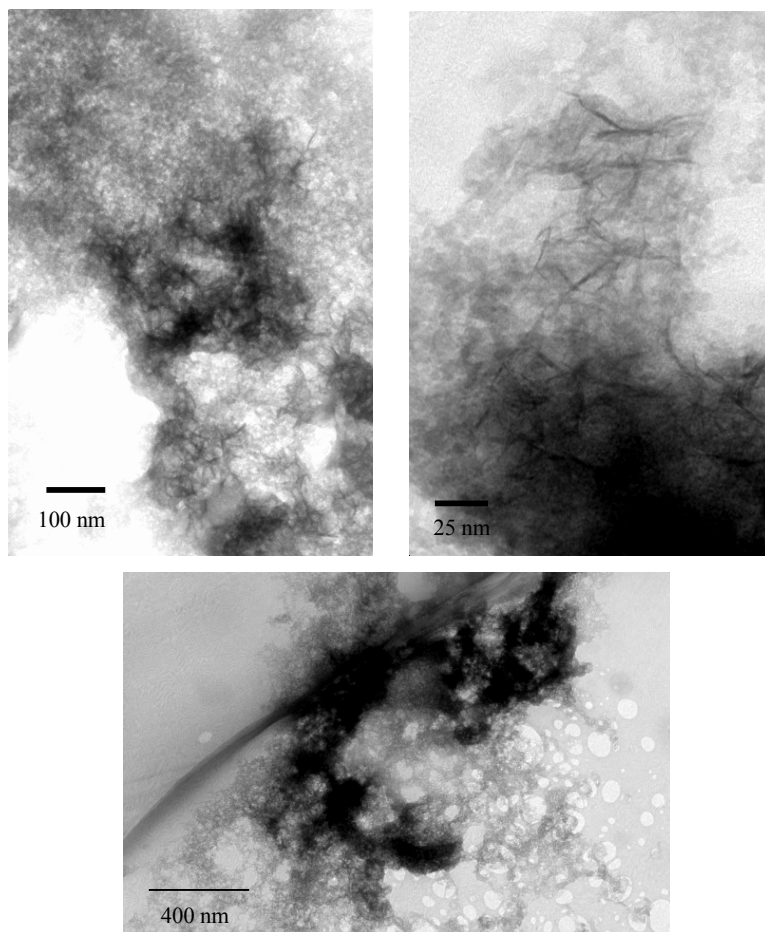
Fig. 3. TEM images of silicate agglomerates from the U-Al drip test.
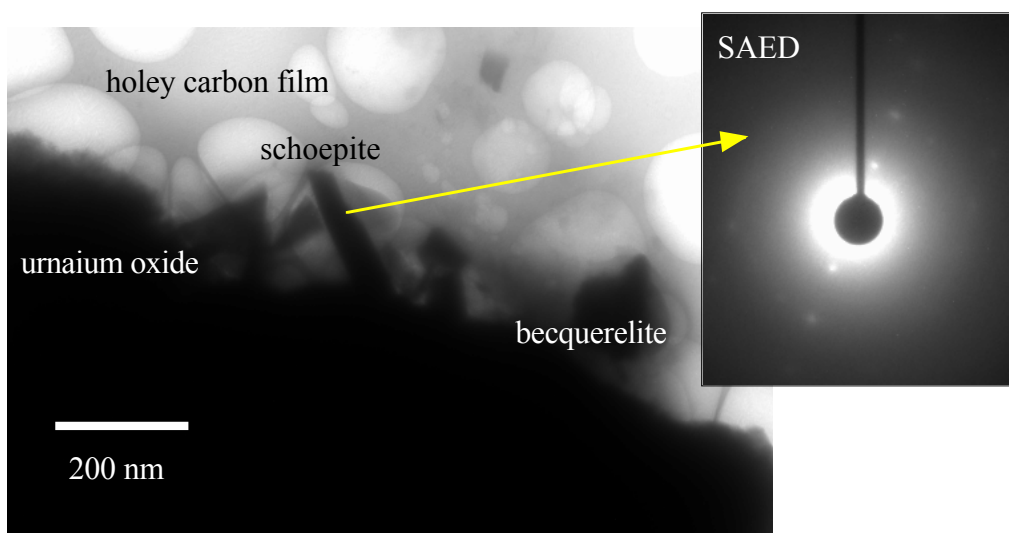
Fig. 4. mage showing alteration phases on the surface of uranium oxide.

Particles from the corroded surface were removed and transferred directly onto a holey carbon film. The surface of the material was black and silvery. By use of a razor

blade, particles were extracted from the surface under a stereomicroscope. According to SEM analyses, the black regions may be covered in a uranyl alteration phases. Some of the particles were thin enough for imaging.

A mass of uranium bearing phases was found. Based on electron diffraction and EDS analysis, the phases were identified as dehydrated schoepite and becquerelite.

Samples have been isolated for microtoming. These will reported on when the samples are prepared.

Microscopy Analyst: Jennifer Holly
 April 10, 2001
Sample ID: UNAUT 2 D71
Colloid sample # C421

This sample was analyzed during the first and second week of April. There are 8 images and 8 EDS spectra in the pages that follow. All the nickel peaks are artifacts due to the nickel grid. Sample prepared by passing unfiltered leachate from test UNAUT3 after 55 days (UNAUT2d71) through a holey carbon grid.

The table below summarizes the data and images.

Table 2.   Sample ID: TEM colloids grids C421 from sample UNAUT 2 D71 for Mike Kaminski

	Grid #	Notebook	Digital Image Nos.	Comments
NA	none	SN1718:77	1824	Fe rich particle
NA	none	SN1718:77	1825	Si rich particle
NA	none	SN1718:77	1826	3 Ti-rich particles. I found 4 more of these Ti-rich clusters on the grid.
NA	none	SN1718:77	1827	Fe-rich particle with some Al, Si, Ca, S, and Ca.
NA	none	SN1718:77	1828	Al, Si with small amounts of Fe and K.
NA	none	SN1718:77	1829	A cluster of Al-rich particles with small amounts of Cl, S, and Si.
NA	none	SN1718:77	1830	Al, Si, Fe and Mg
NA	none	SN1718:77	1831	Similar in composition as the particle in 1830.
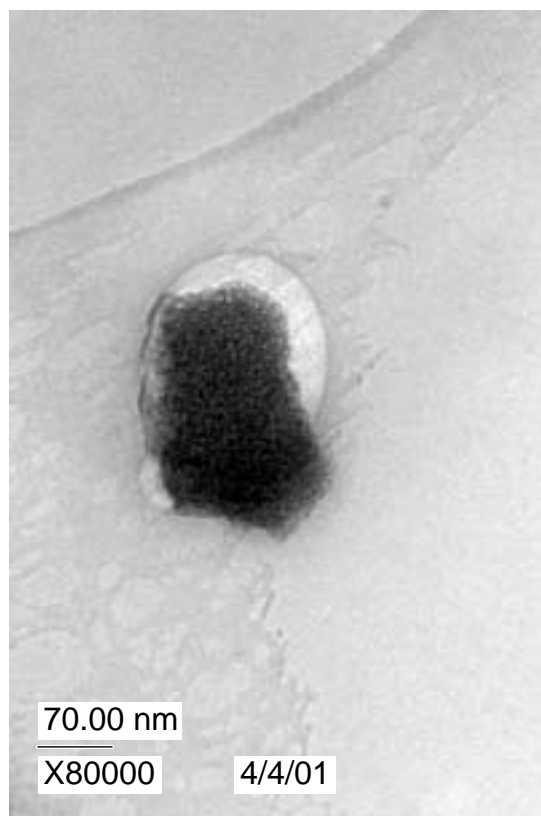
CCD 1824
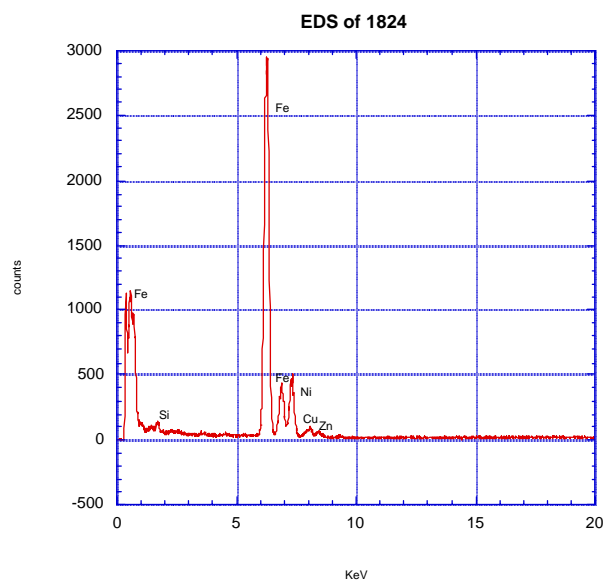
EDS of the Particle in CCD 1824
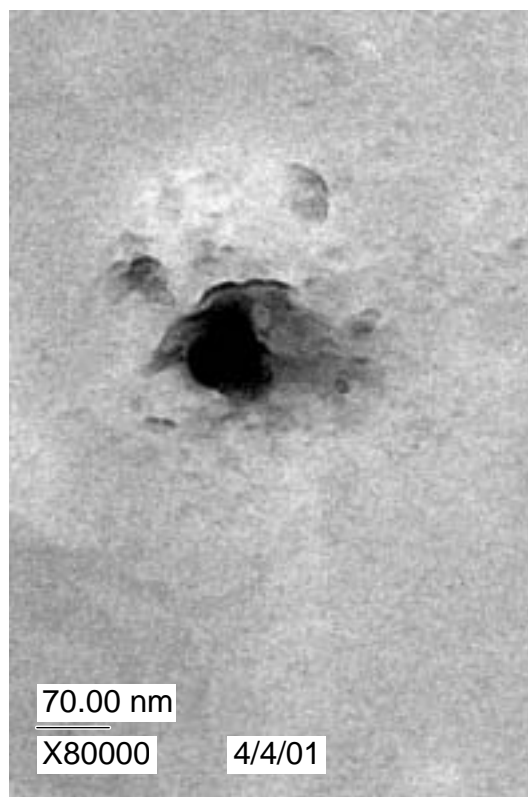
CCD 1825
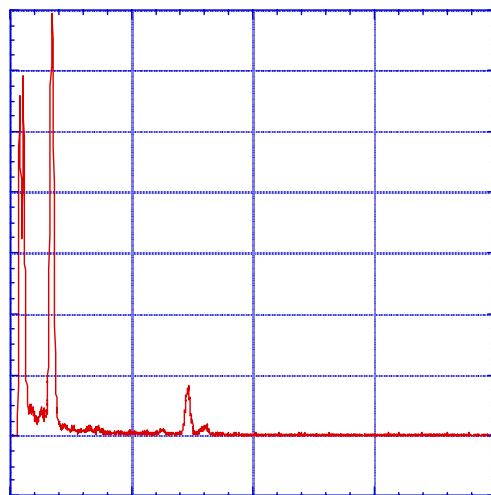
EDS of the Dark Particle in the Center of CCD 1825
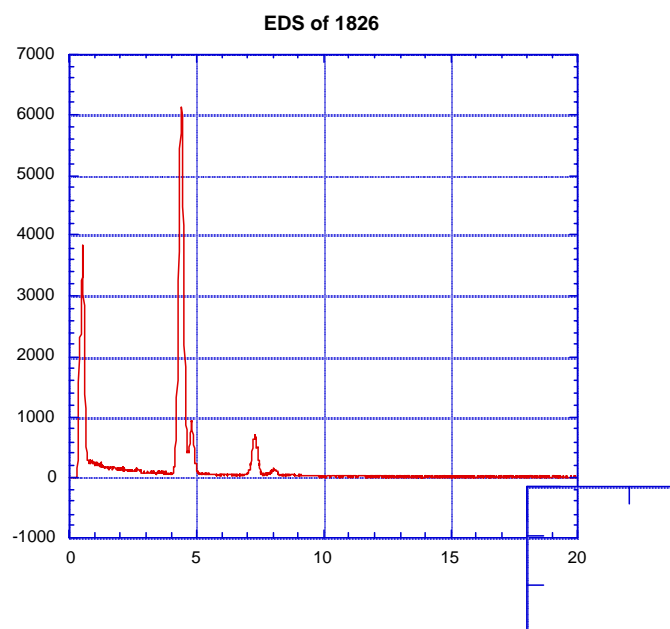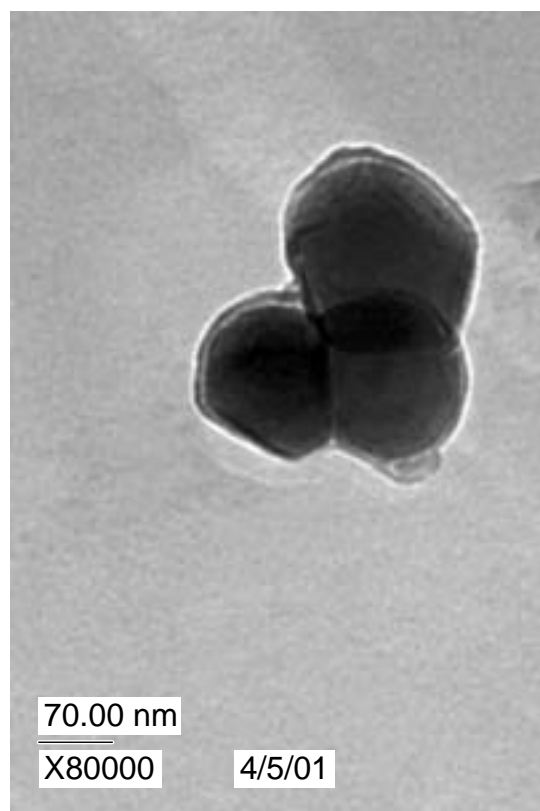
CCD 1826

EDS of the Cluster of Three Particles Imaged in CCD 1826
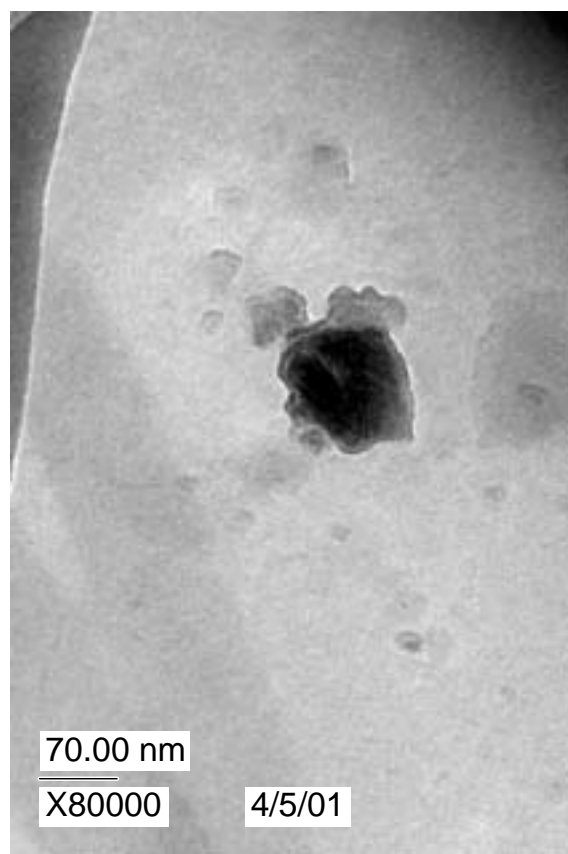
CCD 1827
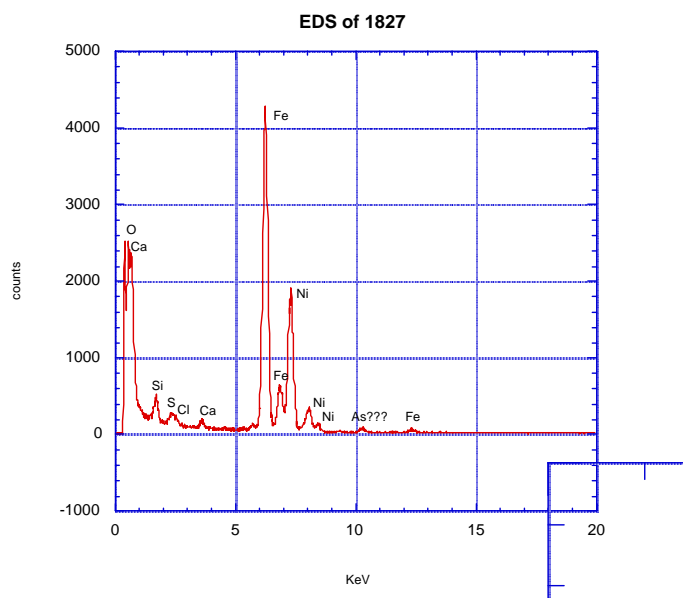
EDS of the Dark Area in CCD 1827
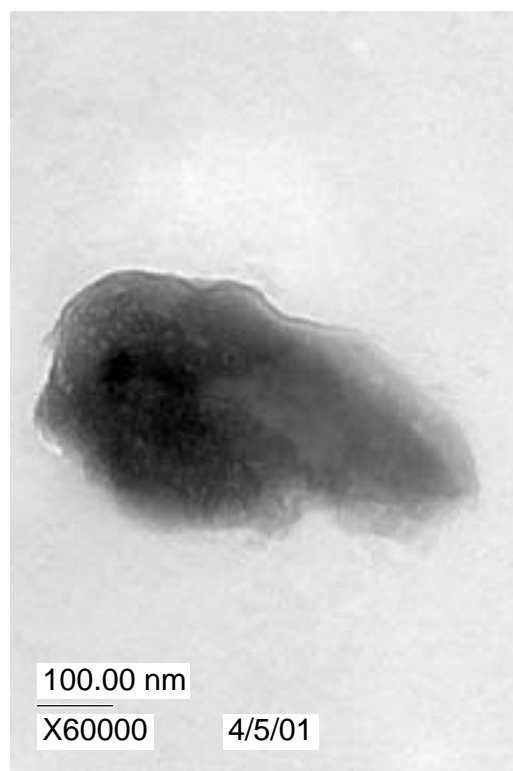
CCD 1828
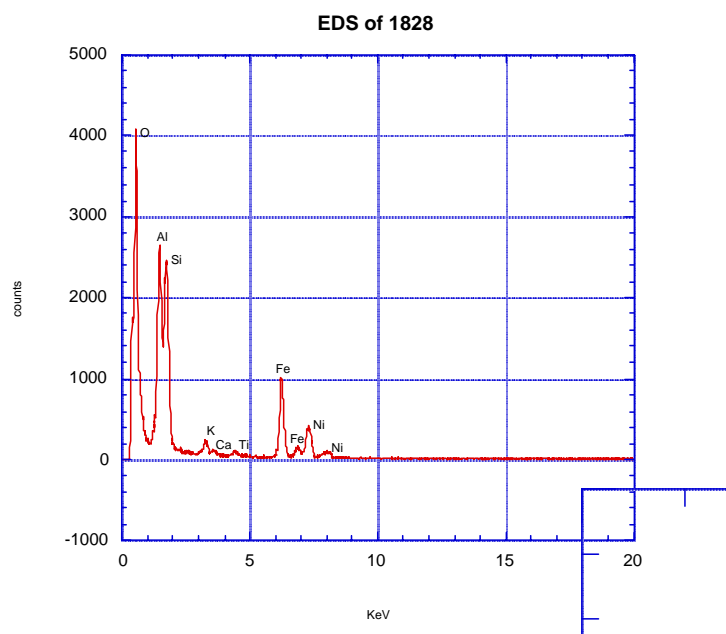
EDS of the Dark Material in CCD 1828
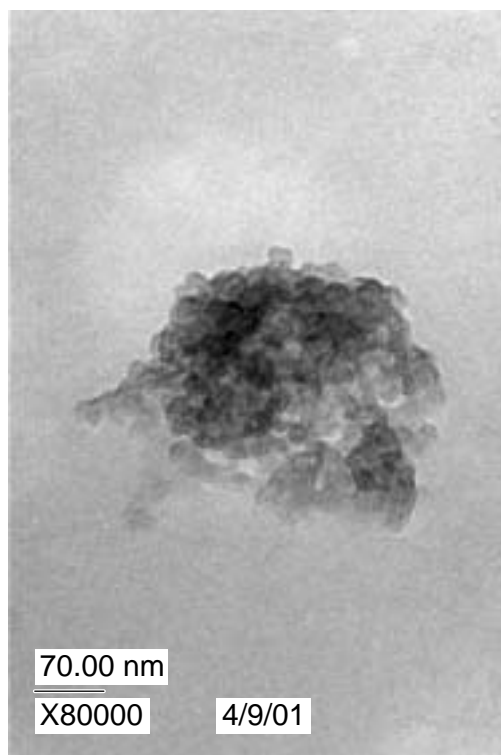
CCD 1829
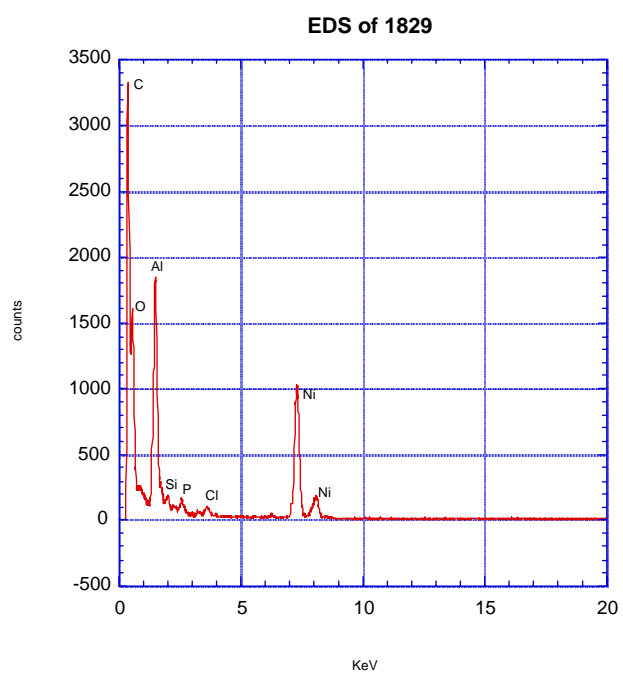
EDS of the Cluster of Particles in CCD 1829

CCD 1830. The halo is due to the intense convergent beam spot during EDS acquisition.

70.00 nm

X80000   4/9/01

EDS of 1830
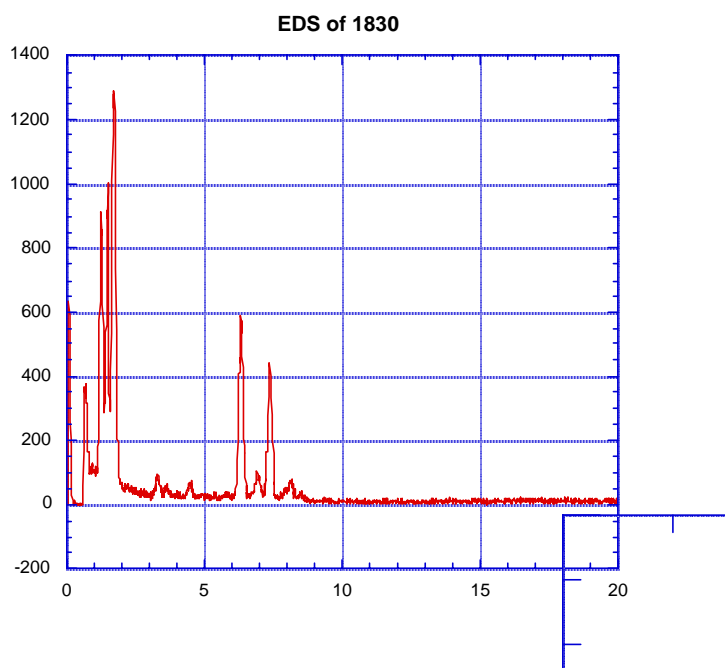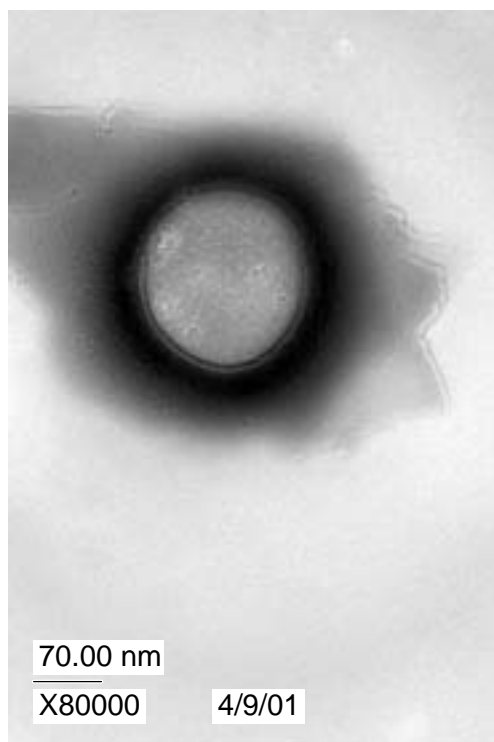
EDS of the Center Area of the Particle in CCD 1830

100.00 nm

X40000   4/9/01
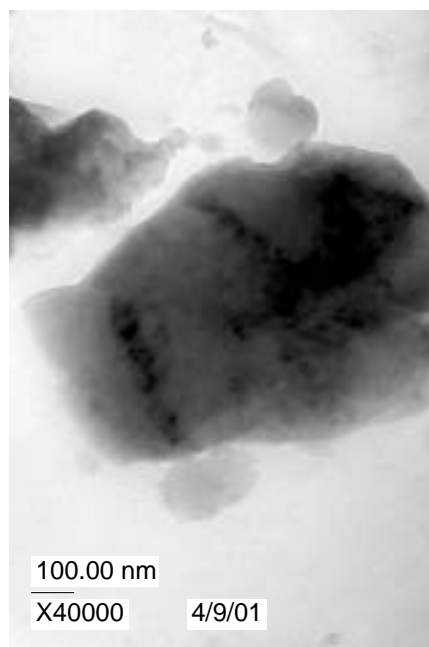
CCD 1831

EDS of 1831
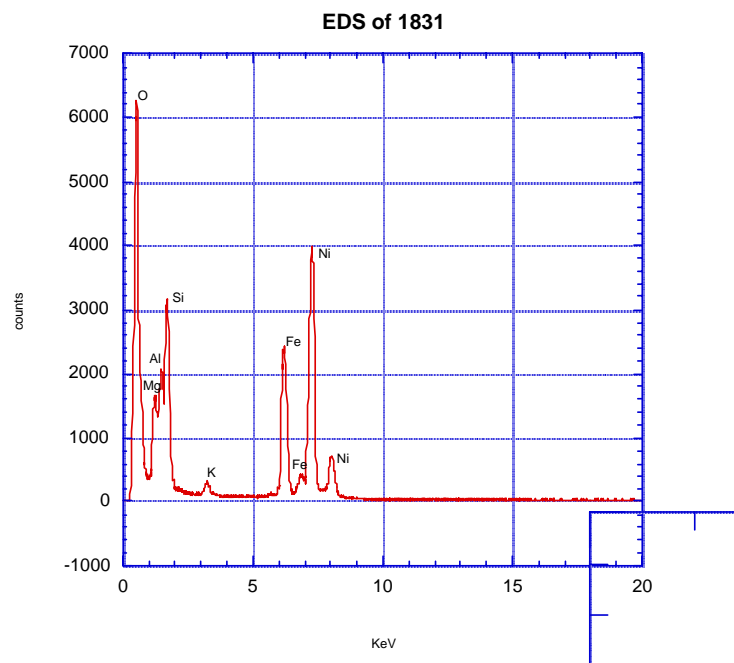
EDS of all the Dark Particle in CCD 1831

Microscopy Analyst: Jennifer Holly
April 4, 2001
Sample ID: UNAUT 1 D183
Colloid sample # C420

This sample was analyzed during the first week of April. There are 9 images and 8 EDS spectra in the pages that follow. All the copper peaks are artifacts due to the copper grid. Sample prepared by passing unfiltered leachate from test UNAUT1 after 183 days through a holey carbon grid.

The table below summarizes the data and images.

Block #	Grid #	Notebook Ref.	Digital Image Nos.	Comments and Elements identified by EDS
NA	none	SN1718:76	1815	Large Si rich particle
NA	none	SN1718:76	1816	Large area of Si rich material with some Na.
NA	none	SN1718:76	1817	Large Ti-rich particle.
NA	none	SN1718:76	1818	Elongated structure with "fuzzy" appearance. EDS identified Si, K, P, and Al.
NA	none	SN1718:76	1819	More "fuzzy" material of similar composition to material in 1818.
NA	none	SN1718:76	1820	Ti-rich cluster of particles. No EDS spectra data saved.
NA	none	SN1718:76	1821	Si, Al, K,S, and Cl.
NA	none	SN1718:76	1822	Si and Al
NA	none	SN1718:76	1823	Si and Al

100.00 nm

X40000   4/2/01
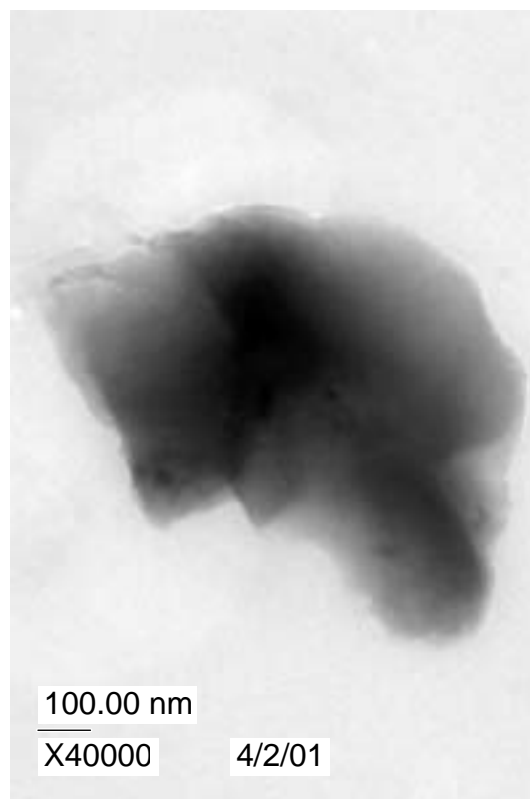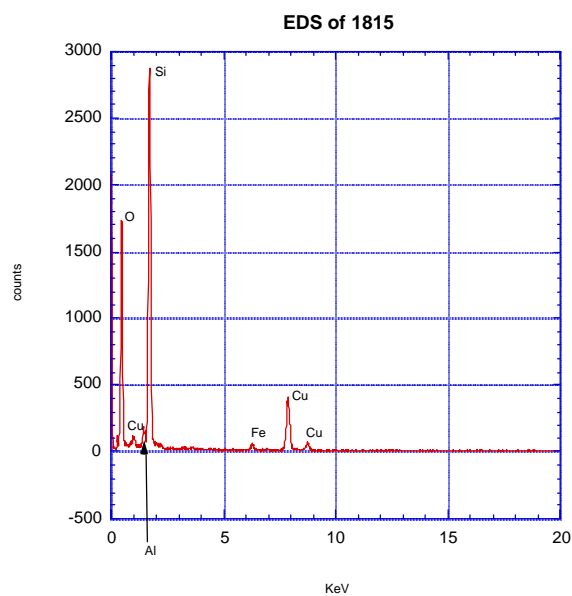
CCD 1815

EDS of Particle in CCD1815
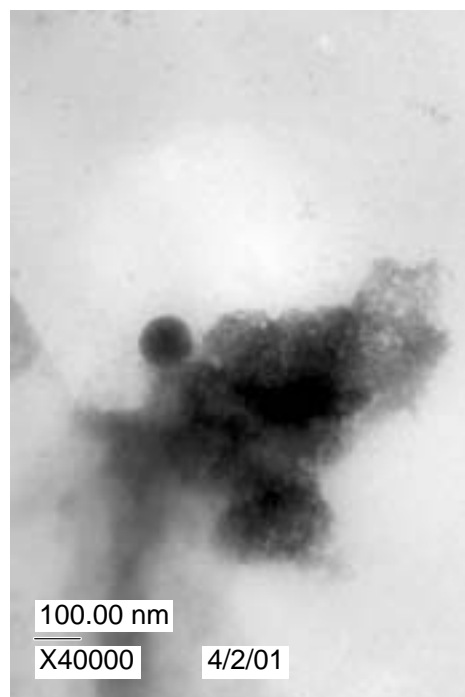
CCD 1816
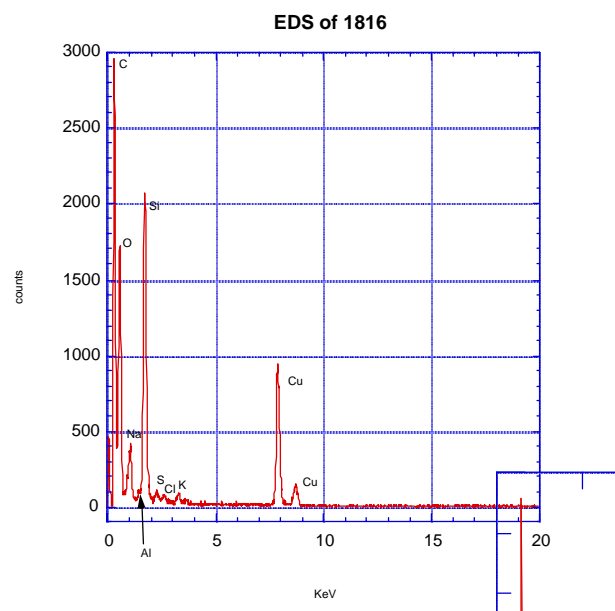
EDS of the Material in CCD 1816.
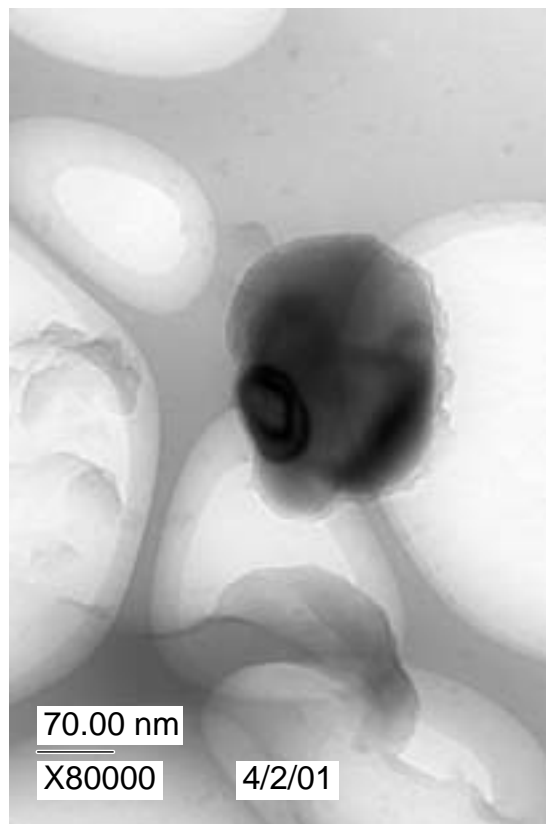
CCD 1817

EDS of 1817
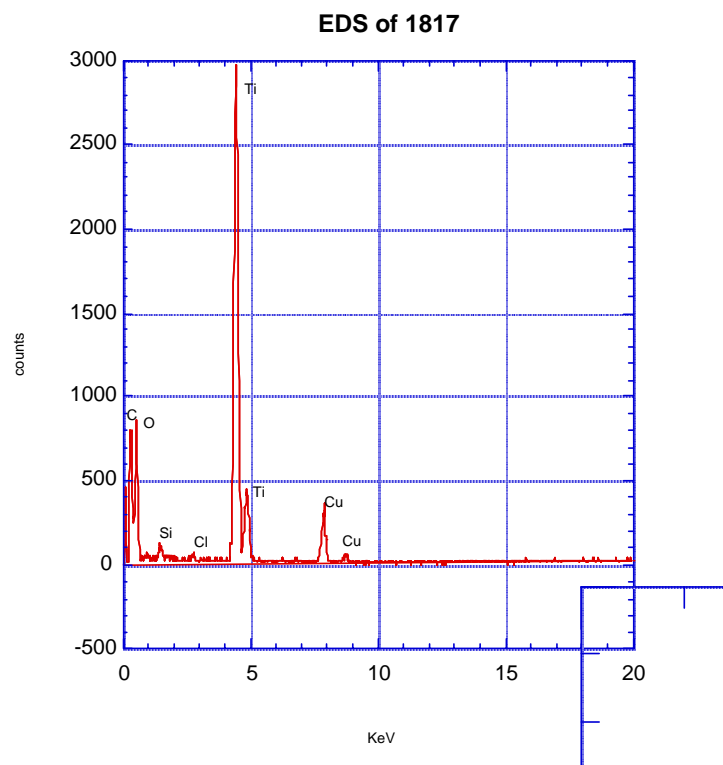
EDS of Central Particle in CCD 1817

CCD 1818. Notice the large elongated structure containing fuzzy material in this image. This particular area of the grid contained three large structures appearing to be similar to this one. Several smaller round particles of approximately 60 to 110 nm in diameter were found near these elongated "fuzzy" structures, which are found in images 1821-1823.
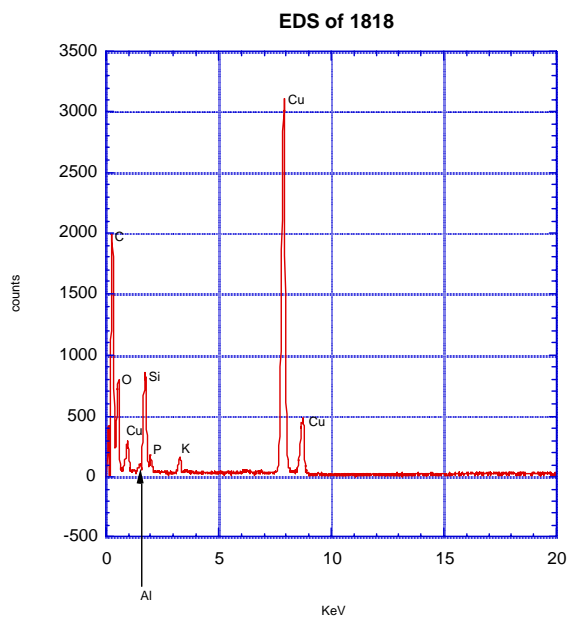
EDS of "Fuzzy Material" in CCD 1818
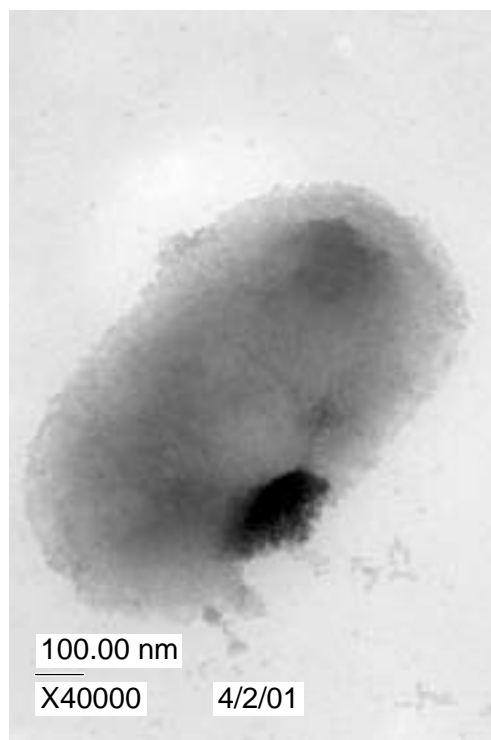
CCD 1819
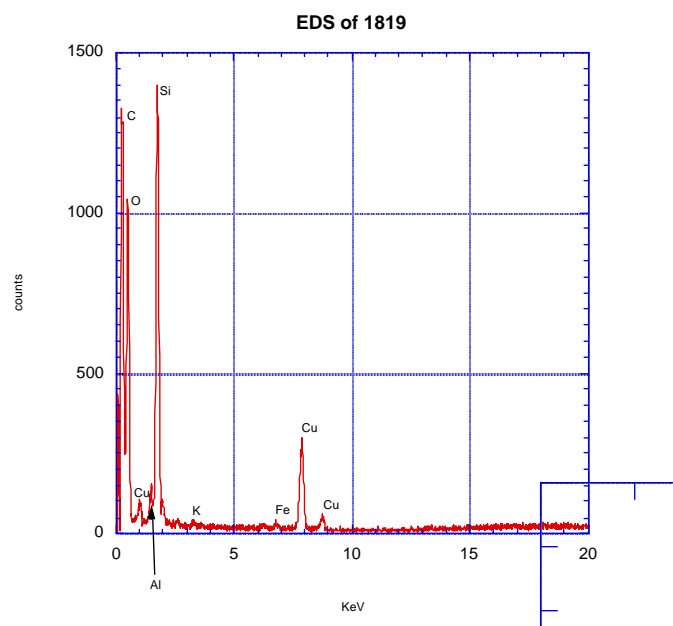
EDS of the Large Particle in CCD 1819
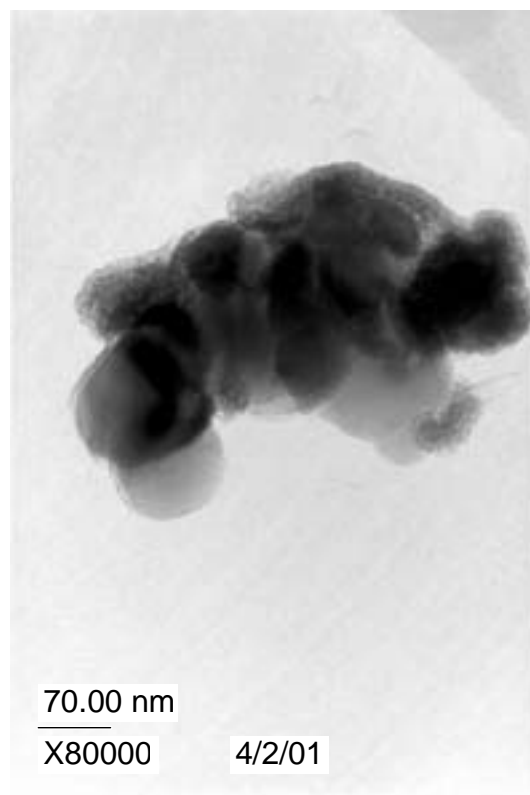
CCD 1820

There wasn't an EDS spectrum recorded for these particles because the EDS was very similar to the EDS recorded for the particle in CCD 1817.

100.00 nm

X40000   4/2/01
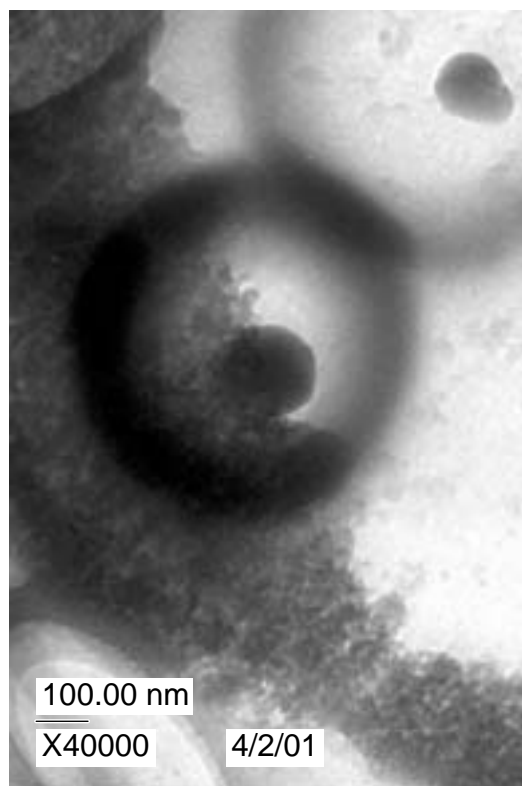
CCD 1821 of the area containing both the round particle analyzed by the EDS spectra 1821 and the fuzzy elongated material similar to that found in CCD 1818. The halos around the particles are from beam damage during the EDS analysis.
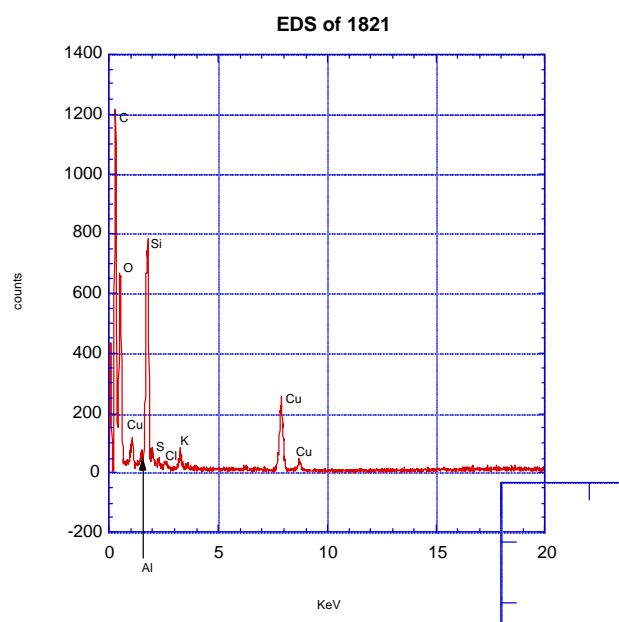
EDS of the central particle with the darkest halo surrounding it in CCD 1821.
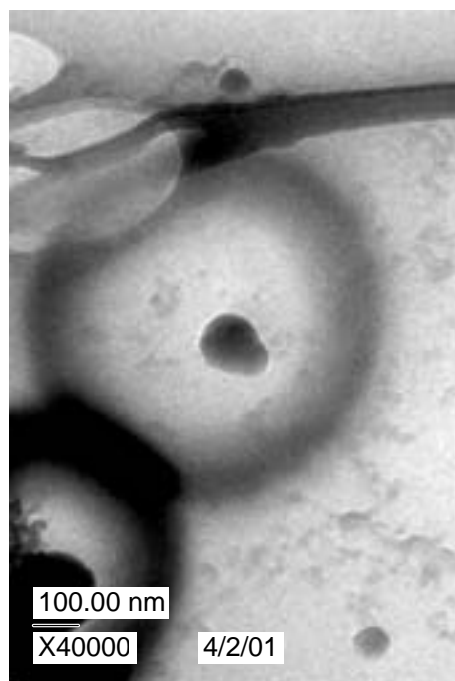
CCD 1822 The particle of interest in this picture is the one in the very center of this image and off to the upper right in CCD 1821.
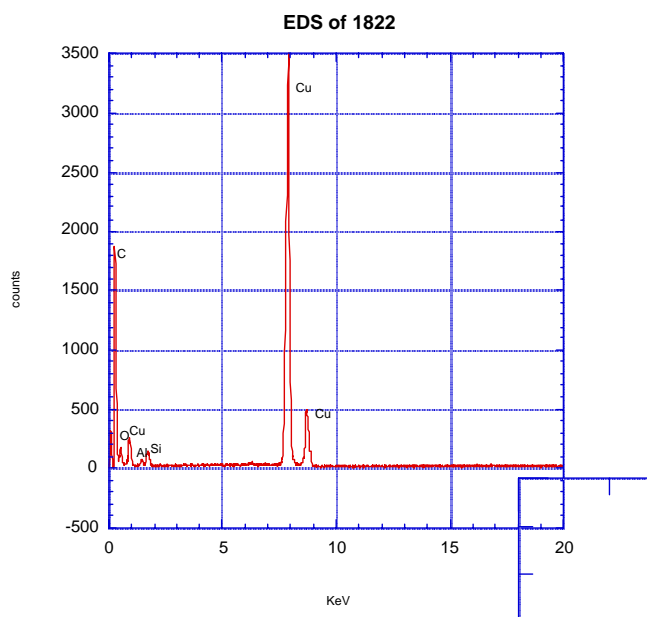
EDS of the central particle in CCD 1822 with the light halo surrounding it.
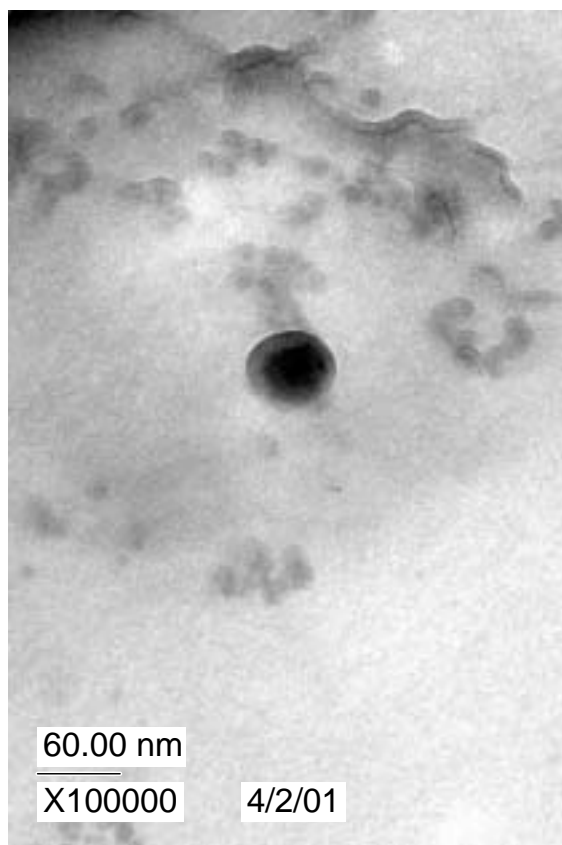
CCD 1823
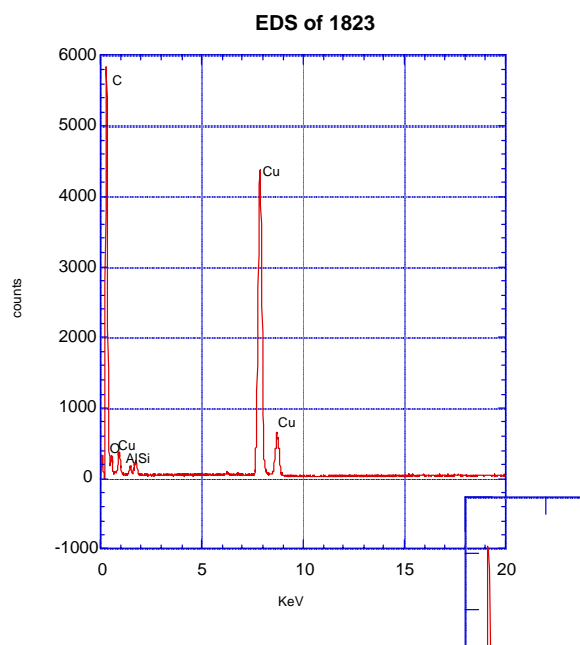
EDS of Spherical Particle in CCD 1823

**Raw Data from ICP-MS of Aqueous Solutions Generated under
Unirradiated UAl$_x$ Tests and Subsequent Release Rate Calculations**

Table E1. ICP-MS Analysis Report (RFA#: I-000303-2)

ICP-MS Analysis Report **(RFA#: I-000303-2)**							
Submitted by:	M. Kaminski	Date of analysis:	3/28/00		Analyst:	Y. Tsai /	
						S. F. Wolf	
Sample Name		UNAUT1/1-21strip	UNAUT1D67 SFHstrip	UNAUT1D67 Bstrip	UNAUT1SFH1 -21	UNAUT1EJB	UNAUT1D67-V	Estimated
								Accuracy
Element		Concentration (PPB)	Concentration (PPB)	Concentration (PPB)	Concentration (PPB)	Concentration (PPB)	Concentration (PPB)	
Sodium	Na	273	810	791	4.66E+04	7.03E+04	6.30E+04	±10%
Magnesium	Mg	32.9	169	153	174	28.7	214	±10%
Aluminium	Al	99.7	614	576	993	259	771	±10%
Silicon	Si	246	2.28E+03	2.35E+03	3.41E+04	4.26E+04	3.88E+04	±10%
Iron	Fe	891	2.24E+03	2.67E+03	98.4	166	135	±10%
Zirconium	Zr	7.66	60.2	26.1	<0.12	31.7	4.17	±10%
Gold	Au	<0.02	<0.02	<0.02	1.57	0.071	0.421	±10%
Uranium	U	<2.67	23.7	5.44	64.3	14.3	71.2	±10%
*Uranium	*U235	<0.61	4.99	<0.61	10.6	2.22	10	±10%
* = Semi-Quantitation								

Table E2. ICP-MS Analysis Report (RFA#: I-000411-1)

ICP-MS Analysis Report (RFA#: I-000411-1)						
Submitted by:	M. Kaminski		Date of analysis:	4/13/00	Analyst:	Y. Tsai / S. F. Wolf
Sample Name		EJ13 MG3	UNAUT2-D16-VC	UNAUT2-D16-AS V	UNAUT2-D16-AS SFH	Estimated Accuracy
Element		Concentration (PPB)	Concentration (PPB)	Concentration (PPB)	Concentration (PPB)	
Sodium	Na	5.85E+04	6.42E+04	286	360	±10%
Magnesium	Mg	288	127	35.6	74.6	±10%
Aluminium	Al	628	1.36E+03	209	416	±10%
Silicon	Si	4.54E+04	4.31E+04	600	242	±10%
Calcium	Ca	8.41E+03	6.14E+03	284	265	±10%
Iron	Fe	498	215	3.01E+03	51.5	±10%
Zirconium	Zr	2.45	1.82	1.5	8.58	±10%
Gold	Au	<0.2	0.128	<0.02	0.022	±10%
Uranium	U	1.37	80.3	6.58	12.3	±10%
*Uranium 235	*U235	<0.2	24.1	1.97	3.71	±27%
* = Semi-Quantitative						

Table E3. ICP-MS Analysis Report (RFA#: I-000522-1)

ICP-MS Analysis Report   **(RFA#: I-000522-1)**

Submitted by:	M. Kaminski	Date of analysis:	6/6/00		Analyst:	Y. Tsai / S. F. Wolf		

Sample Name		UNAUB1 5-10 AS-SFH	UNAUB1 5-10 ASV	UNAUT1-d115-AS-SFH	UNAUT1-d115-AS-V	Mertz-EJ13-762	UNAUB1-V 5-12	UNAUT1-d115-VC	Estimated Accuracy
Element		Concentration (PPB)	Concentration (PPB)	Concentration (PPB)	Concentration (PPB)	Concentration (PPB)	Concentration (PPB)	Concentration (PPB)	
Sodium	Na	9.67E+03	192	9.72E+03	889	4.69E+04	5.82E+04	1.47E+05	±10%
Magnesium	Mg	74.8	33.2	57.3	52.8	192	68.3	16.1	±10%
Aluminium	Al	114	108	203	255	447	217	108	±10%
Silicon	Si	789	897	1.19E+03	4.04E+03	3.87E+04	4.25E+04	2.65E+04	±10%
Calcium	Ca	2.02E+03	211	1.62E+03	1.74E+03	9.79E+03	7.80E+03	2.44E+03	±10%
Chromium	Cr	15.6	1.23E+03	6.78	276	<2.8	68.2	54.5	±10%
Iron	Fe	158	3.07E+03	72.9	1.33E+03	<28.2	113	<14.1	±10%
Zirconium	Zr	21.1	4.09	3.41	0.877	<0.22	0.482	1.87	±10%
Gold	Au	21.2	0.022	14.9	0.048	<0.04	0.072	0.161	±10%
Uranium	U	0.339	0.216	21.3	24.6	0.488	0.384	50.7	±10%
*Uranium	*U238	<0.01	<0.01	5.18	5.82	<0.1	<0.01	12.6	±11%

* = Semi-Quantitative

Table E4. ICP-MS Analysis Report (RFA#: I-000918-1)

ICP-MS Analysis Report (RFA#: I-000918-1)

Submitted by:	M. Kaminski		Date of analysis:	11/7/00		Analyst:	Y. Tsai				

Sample Name		UNAUB1-D151-ASV	UNAUB1-D151-SFH-AS	SNF UNAUB1-D151-V	UNAUT1-D183-ASV	UNAUT1-D183-SFH-AS	UNAUT1-D183-V	UNAUT2-D71-ASV	UNAUT2-D71-SFH-AS	SNF UNAUT2-D71-V	SNF TSR762-EJ13	Estimated Accuracy
Dilution Factor		1	1	1	1	1	10	1	1	1	1	
Element		ppb	ppb	ppb	ppb	ppb	ppb	ppb	ppb	ppb	ppb	
Sodium	Na	186	3.26E+03	5.56E+04	1.70E+03	2.07E+03	7.07E+05	246	1.62E+03	5.73E+04	5.23E+04	±10%
Magnesium	Mg	77	32.3	24.8	74.2	52.5	<8.4	82.8	64.9	42	293	±10%
Aluminium	Al	88.9	<50.8	272	252	440	<508	89.7	156	410	496	±10%
Silicon	Si	508	204	3.47E+04	1.87E+03	804	1.44E+05	495	624	3.52E+04	3.57E+04	±10%
Potassium	K	<57.5	<57.5	1.11E+04	413	<57.5	9.35E+04	<57.5	<57.5	1.14E+04	1.08E+04	±10%
Calcium	Ca	391	162	8.57E+03	2.30E+03	450	9.90E+03	205	177	1.01E+04	1.36E+04	±10%
Iron	Fe	827	<61.6	<61.6	764	<61.6	1.82E+03	929	<61.6	<61.6	<61.6	±10%
Zirconium	Zr	0.544	20.4	0.063	1.18	27.1	1.9	2.88	34.1	0.225	<0.03	±10%
Gold	Au	0.082	31.3	0.068	0.082	47.2	3.1	0.076	10.5	0.052	<0.04	±10%
Uranium	U	<0.19	<0.19	0.382	13.2	17	33	4.25	12.9	61.5	0.219	±10%
Uranium	U235	<0.01	<0.01	0.015	3.27	4.23	8.26	1.11	3.3	16	0.011	±16%

* = Semi-Quantitative

Table E5. Raw Data for Analysis of the EJ-13 Water

Z	EJ-13 MG#3	TSR762
Na	5.85E+4	5.23E+4
Mg	288	293
Al	6.28E+2	4.96E+2
Si	4.54E+4	3.57E+4
K	DNA	1.08E+4
Ca	8.41E+3	1.36E+4
Fe	4.98E+2	<61.6
Zr	2.45	0.03
Au	0.20	0.04
U	1.37	0.22
*U235	0.3425	0.05475

Table E6. Mass (g) of Supernate and Acid Strip Solutions Recovered from Test Samplings

Test #	Sampling day	Reference Notebook	Total solution in base	Total solution in SFH	Total strip solution used base	Total strip solution used SFH	Injected solution	Starting solution
UNAUT1	Day 30	1682-27-29,35,36	4.99	1.63	44.97	none	6.0	5.04
	Day 67	1682-36,53,54	7.23	1.7504	48.33	53.06	6.0	5.11
	Day 115	1682-54,74,75	4.27	0	43.44	50.75	9.75	5.03
	Day 183	1682-75,105,106,109-110	1.6442	0	45.13	52.61	12.75	9.96
UNAUT2	Day 16	1682-64,65,76,77	7.53	0	44.11	64.18	3.75	5.03
	Day 55	1682-77, 112,113	15.0387	0	47.54	68.25	11.25	5.03
UNAUB1	Day 83	1682-44,45,72,73	14.6	0	43.44	48.85	17.25	5.01
	Day 151	1682-73,115,116	17.4382	0	42.01	98.1	13.25	5.01

Table D7. Elemental Percentages Recovered from Disposition from Test Samplings. Totals from base, base strip, and spent fuel holder (SFH) strip solutions are 100%.

	UNAUT1			UNAUT2			UNAUB1		
Z	base	base strip	SFH strip	base	base strip	SFH strip	base	base strip	SFH strip
Na	74	6.7	19	89	1.6	9	69	0.6	30
Mg	5.5	43	52	10	34	57	11	36	53
Al	6.1	40	54	24	20	56	29	31	39
Si	55	29	16	89	5.2	6.0	91	4.5	4.4
K	88	11	1.7	96	1.5	2.2	96	1.2	2.8
Ca	11	74	15	79	9	12	65	6.3	28
Fe	1.2	56	43	1.4	95	4.0	1.5	91	7.5
Zr	2.9	21	77	0.6	6.6	93	0.3	6.2	94
Au	0.3	0.3	99	0.2	0.6	99	0.1	0.1	100
U-238	14	32	54	41	13	45	32	25	43
U-235	14	32	54	41	13	45	32	25	43

Distribution for ANL/CMT-03/01

Internal (Printed Copies):

M. M. Goldberg	L. Nuñez	G. F. Vandegrift
M. D. Kaminski (5)	M. J. Steindler	S. K. Zussman

Internal (Electronic Copies):

M. R. Hale, TIS	J. C. Cunnane	J. A. Fortner
T. S. Bray	W. L. Ebert	D. Lewis
Y. I. Chang	R. J. Finch	C. J. Mertz

External (Printed Copies):

T. Adams, SRS
W. Hurt, INEEL
N. Iyer, SRS
C. Shelton-Davis, INEEL
R. Sindelar, SRS
P. Wheatley, INEEL

External (Electronic Copies):
M. A. Buckley, Library-E
E. Sackett, Library-W
Chemical Technology Division Review Committee Members:
   H. U. Anderson, University of Missouri-Rolla, Rolla, MO
   R. A. Greenkorn, Purdue University, West Lafayette, IN
   C. L. Hussey, University of Mississippi, University, MS
   M. V. Koch, University of Washington, Seattle, WA
   V. P. Roan, Jr., University of Florida, Gainesville, FL
   J. R. Selman, Illinois Institute of Technology, Chicago, IL
   J. S. Tulenko, University of Florida, Gainesville, FL
M. Ebner, INEEL
H. Loo, INEEL
T. Thornton, Framatome, Las Vegas, NV